Max-Planck-Institut
für Meteorologie

MAX-PLANCK-GESELLSCHAFT

International Max Planck Research School
on Earth System Modelling

Effects of coupling frequency on climate simulated by a coupled AO-GCM

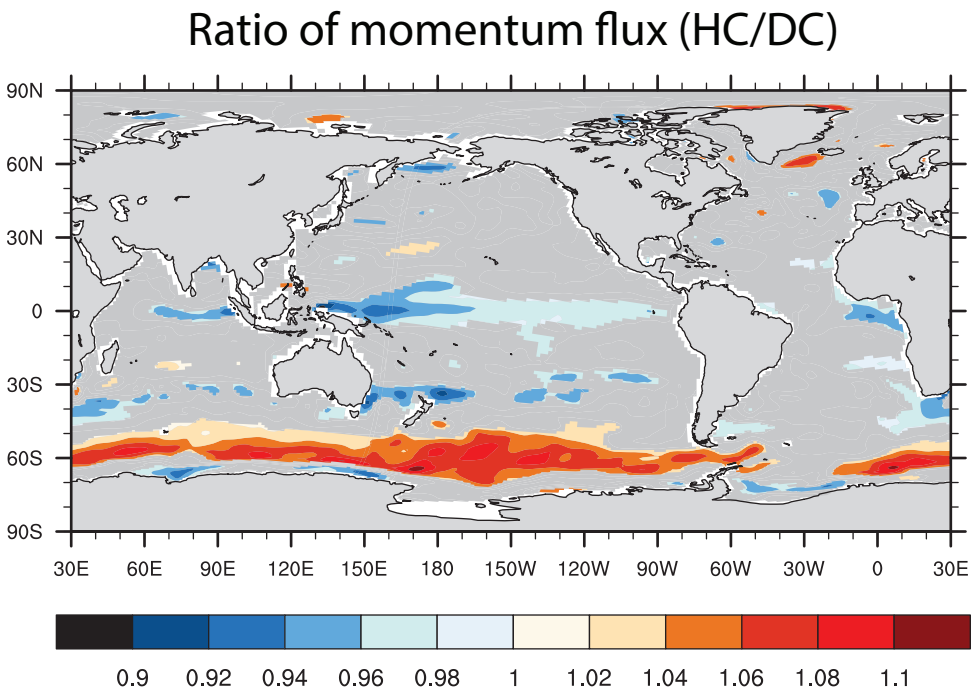

Fangxing Tian

Hamburg 2016

Berichte zur Erdsystemforschung
Reports on Earth System Science

182
2016

Hinweis

Die Berichte zur Erdsystemforschung werden vom Max-Planck-Institut für Meteorologie in Hamburg in unregelmäßiger Abfolge herausgegeben.

Sie enthalten wissenschaftliche und technische Beiträge, inklusive Dissertationen.

Die Beiträge geben nicht notwendigerweise die Auffassung des Instituts wieder.

Die "Berichte zur Erdsystemforschung" führen die vorherigen Reihen "Reports" und "Examensarbeiten" weiter.

Notice

The Reports on Earth System Science are published by the Max Planck Institute for Meteorology in Hamburg. They appear in irregular intervals.

They contain scientific and technical contributions, including Ph. D. theses.

The Reports do not necessarily reflect the opinion of the Institute.

The "Reports on Earth System Science" continue the former "Reports" and "Examensarbeiten" of the Max Planck Institute.

Anschrift / Address

Max-Planck-Institut für Meteorologie
Bundesstrasse 53
20146 Hamburg
Deutschland

Tel./Phone: +49 (0)40 4 11 73 - 0
Fax: +49 (0)40 4 11 73 - 298

name.surname@mpimet.mpg.de
www.mpimet.mpg.de

Layout

Bettina Diallo and Norbert P. Noreiks
Communication

Copyright

Effects of coupling frequency on climate simulated by a coupled AO-GCM

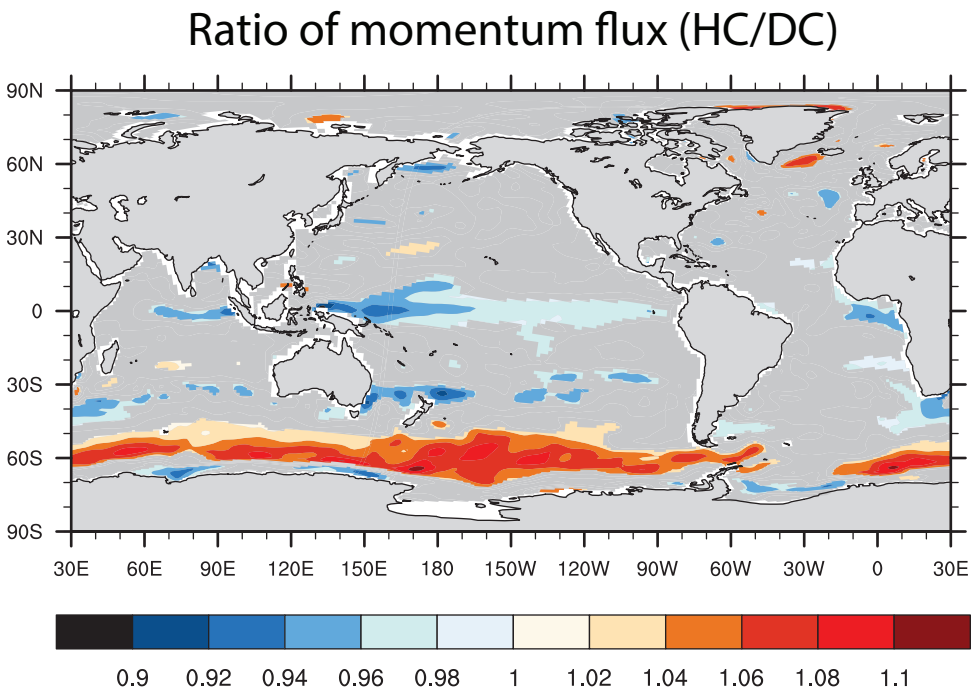

Fangxing Tian

Hamburg 2016

Fangxing Tian

Max-Planck-Institut für Meteorologie
Bundesstrasse 53
20146 Hamburg

Tag der Disputation: 1.7.2016

Folgende Gutachter empfehlen die Annahme der Dissertation:

Prof. Dr. Martin Claussen
Dr. (habil) Jin-Song von Storch

Berichte zur Erdsystemforschung / Max-Planck-Institut für Meteorologie 182
Reports on Earth System Science / Max Planck Institute for Meteorology 2016

ISSN 1614-1199

Abstract

In the climate system, processes on intra-daily time scales can influence processes on longer and larger scales. The temporal resolution of most global observations is not high enough to properly describe intra-daily processes; and the air-sea coupling frequency in more than half of the Coupled Model Intercomparison Project Phase 5 (CMIP5) models is not high enough to resolve intra-daily processes and the air-sea feedbacks induced by these processes. Thus, our understanding of the interactions of intra-daily variations with processes on time scales longer than one day is limited. In this thesis, the effects of intra-daily processes on the climate state and on inter-annual variability is investigated using the CMIP5-version of the Max Planck Institute-Earth System Model (MPI-ESM) with a coupling frequency between the atmospheric and oceanic components being once per day and once per hour.

It is found that increasing the coupling frequency to include intra-daily air-sea interactions reduces some of the known biases of the model, in particular, the biases of SST, oceanic potential temperature, and zonal winds in the atmosphere.

The parametrizations of air-sea fluxes of momentum, heat and fresh water are directly related to the coupling frequency. In order to describe the spatial distribution and the temporal evolution of the intra-daily variability of the air-sea fluxes, the effects of an increased coupling frequency on the basic statistics of the air-sea fluxes at grid point level are investigated. Increasing the coupling frequency reduces the mean of the momentum-flux magnitude by up to 7% in the tropics and increases it by up to 10% in the Southern Ocean. The variance and extremes of all the fluxes are increased in most parts of the oceans. Exceptions are found for the momentum and fresh water fluxes in the tropics. The increases of the variance are substantial, reaching up to 50% for the momentum flux, 100% for the fresh water flux, and a factor of 15 for the net heat flux. These diurnal and intra-diurnal variations account for up to 50% to 90% of the total variances and exhibit distinct seasonality. An analysis that differentiates the effect of daily averaging from that of air-sea feedbacks occurring within a day is performed, and it is found that using hourly coupling without daily averaging leads to increases in variances and extremes, whereas changes in the mean wind stress in the tropical and Southern Ocean and the decreases of variance and extremes over the tropical oceans are due to intra-diurnal air-sea feedbacks.

Besides grid-point changes, increasing the coupling frequency also leads to changes in terms of large-scale modes. In the Southern Ocean, the dependence of the SST-wind-stress feedback on the mean state of SST, which is colder in the hourly coupled experiment, leads to an increase of westerlies. In the Equatorial Pacific, in the hourly coupled experiment, the Bjerknes feedback reveals a diurnal cycle during El Niño events, with the feedback being stronger in the nighttime than in the daytime, but no clear diurnal cycle during La Niña events. This leads to a decrease of wind stress in the Equatorial Pacific in the hourly coupled experiment.

Increasing the coupling frequency also affects El Niño-Southern Oscillation (ENSO). ENSO is not symmetric: El Niño is stronger than La Niña. However, CMIP5 models that use daily ocean-atmosphere coupling simulate almost symmetric ENSO. Increasing the coupling frequency from daily to hourly, the ENSO asymmetry can be simulated by MPI-ESM. This can be explained by the ability of the hourly coupled model to resolve intra-daily air-sea feedbacks which affect the pattern and strength of the convection over the tropical Pacific, and consequently, the asymmetry of El Niño and La Niña. This result is further confirmed by MPI-ESM with different spatial resolutions.

Zusammenfassung

Im Klimasystem können Prozesse mit intra-täglichen Zeitskalen länger-dauernde und großskalige Prozesse beeinflussen. Die zeitliche Auflösung von den meisten globalen Beobachtungen ist nicht hoch genug, um intra-tägliche Prozesse genau genug zu beschreiben; und die Kopplungsfrequenz zwischen Atmosphäre und Ozean in mehr als der Hälfte der Modelle der *Coupled Model Intercomparison Project Phase 5* (CMIP5) ist nicht hoch genug, um intra-tägliche Prozesse und die durch diese Prozesse erzeugte Atmosphäre-Ozean-Rückkopplungen aufzulösen. Deswegen ist unser Verständnis von Interaktionen zwischen intra-täglichen Variationen und Prozessen mit Zeitskalen von mehr als einem Tag eingeschränkt. In dieser Doktorarbeit werden die Auswirkungen von intra-täglichen Prozessen auf den Klimazustand und auf zwischenjährliche Veränderungen untersucht unter Benutzung der CMIP5-Version des Max-Planck-Institut Erdsystemsmodels (MPI-ESM) mit einer Kopplungsfrequenz zwischen atmosphärischen und ozeanischen Komponenten von einmal pro Tag sowie einmal pro Stunde.

Es stellt sich heraus, dass eine Erhöhung der Kopplungsfrequenz, die intra-tägliche Atmosphäre-Ozean-Schwankungen berücksichtigt, einige der bekannten Fehler des Models reduziert, insbesondere die Fehler von SST, potentieller Temperatur des Ozeans sowie des zonalen Windes der Atmosphäre.

Die Parametrisierung der Atmosphäre-Ozean-Flüsse von Impuls, Wärme und Süßwasser sind direkt abhängig von der Kopplungsfrequenz. Um die räumliche Auflösung und die zeitliche Entwicklung der intra-täglichen Variabilität der Atmosphäre-Ozean-Flüsse zu beschreiben, werden die Auswirkungen einer Erhöhung der Kopplungsfrequenz auf die grundsätzlichen Statistiken der Atmosphäre-Ozean-Flüsse an Gitterpunkten untersucht. Eine Erhöhung der Kopplungsfrequenz reduziert den Mittelwert des Impulsflusses um bis zu 7% in den Tropen und erhöht ihn um bis zu 10% im Südlichen Ozean. Die Varianz und die Extremwerte von allen Flüssen sind in den meisten Teilen der Ozeane erhöht. Ausnahmen werden für den Impuls- und Süßwasserfluss in den Tropen gefunden. Die Erhöhung der Varianz ist substanziell und erreicht bis zu 50% für den Impulsfluss, 100% für den Süßwasserfluss und einen Faktor von 15 für den totalen Wärmefluss. Diese täglichen und intra-täglichen Variationen machen zwischen 50 und 90% der totalen Varianz aus und sind saisonal unterschiedlich ausgeprägt. Eine Analyse, die zwischen den Auswirkungen des täglichen Mittels und denen der intra-täglichen

Atmosphäre-Ozean-Rückkopplungen unterscheidet, wird durchgeführt. Es stellt sich heraus, dass die Nutzung einer stündlichen Kopplung ohne tägliches Mittel eine Erhöhung der Varianz und der Extremwerte zur Folge hat, wohingegen Veränderungen des mittleren Windstresses in den Tropen und im Südlichen Ozean sowie die Abnahme der Varianz und der Extremwerte über den tropischen Ozeanen auf intra-tägliche Atmosphäre-Ozean-Rückkopplung zurückzuführen ist.

Neben der Änderung an Gitterpunkten führt eine Erhöhung der Kopplungsfrequenz auch zu Veränderungen von großskaligen Phänomenen. Im Südlichen Ozean führt die Abhängigkeit der SST-Windstress-Rückkopplung von der mittleren SST, welche kälter im stündlich gekoppelten Experiment ist, zu einer Zunahme der Westwinde. Im äquatorialen Pazifik zeigt die Bjerknes-Rückkopplung im stündlich gekoppelten Experiment einen Tagesgang bei El Niño-Ereignissen, wobei die Rückkopplung in der Nacht stärker ist als am Tag. Es gibt aber keinen klaren Tagesgang bei La Niña-Ereignissen. Dies führt zu einer Abnahme des Windstresses im äquatorialen Pazifik im stündlich gekoppelten Experiment.

Eine Erhöhung der Kopplungsfrequenz wirkt sich auch auf El Niño-Southern Oscillation (ENSO) aus. ENSO ist nicht symmetrisch: El Niño ist stärker als La Niña. Trotzdem simulieren CMIP5-Modelle, die tägliche Atmosphäre-Ozean-Kopplungen nutzen, eine fast symmetrische ENSO. Durch eine Erhöhung der Kopplungsfrequenz von täglich zu stündlich kann die ENSO-Asymmetrie mit MPI-ESM simuliert werden. Dies kann damit erklärt werden, dass das stündlich gekoppelte Modell die Fähigkeit hat, intra-tägliche Atmosphäre-Ozean-Rückkopplungen aufzulösen, die sich auf die Struktur und die Stärke der Konvektion über dem tropischen Pazifik auswirken und sich daher auch auf die Asymmetrie von El Niño und La Niña. Dieses Ergebnis wird zusätzlich von MPI-ESM mit unterschiedlichen räumlichen Auflösungen bestätigt.

Contents

Chapter 1

Introduction

1.1 Motivation

The atmosphere and the ocean are coupled by air-sea fluxes of momentum, heat and water across the air-sea interface. Such a coupling process can influence the oceanic variability, and in turn influence the atmospheric variability. This air-sea interactions occur over a wide range of spatial and temporal scales. Processes with short temporal and small spatial scales can influence processes with longer temporal and larger spatial scales (Meehl et al. 2001). However, the temporal resolution of most of global observations is not high enough to properly describe intra-daily processes; and the air-sea coupling frequency in more than half of the CMIP5 models are not high enough to resolve the intra-daily air-sea interactions. Thus, our understanding of the interactions between the intra-daily and the longer temporal scale systems is limited (Danabasoglu et al. 2006; Bernie et al. 2008; Klingaman et al. 2011; Terray et al. 2012; Guemas et al. 2013; Ham et al. 2010).

The Max Planck Institute-Earth System Models (MPI-ESM) with a coupling frequency of once per hour enables this work to investigate the influences of intra-daily processes, such as diurnal cycle and random intra-daily fluctuations, on the climate state and inter-annual variability of climate system.

1.2 State of research on high-frequency variations and air-sea coupling

There are many gaps in the knowledge of the effect of intra-daily air-sea interactions on the climate system, even though some previous studies exist on two important components of the intra-daily air-sea interactions: the diurnal cycle

(Bernie et al. 2005; Kawai and Wada 2007; Gentemann et al. 2008; Gille 2012; Guemas et al. 2013) and the random intra-daily fluctuations (Palmer 2001; Beena and von Storch 2009; Williams 2012). The diurnal cycle of the air-sea interactions are related to the earth rotation and solar zenith angle. Intra-daily fluctuations are caused, for example, by convective events, turbulence and instabilities within the planetary boundary layers. The current state of researches of the effect of intra-daily air-sea feedback on the climate system is addressed below, divided into studies dealing with the diurnal cycle and the studies dealing with the fluctuations.

1.2.1 Diurnal cycle

Previous studies show that observed magnitude of the SST diurnal cycle varies with the latitude. The diurnal range of SST is typically $2°C - 7°C$ (Kawai and Wada 2007; Gentemann et al. 2008; Gille 2012). Since the net heat flux and fresh water flux are sensitive to the surface temperature, the diurnal cycle of SST may strongly influence the diurnal variation of the atmosphere and the associated air-sea interaction, and thus affect the mean climate state.

The diurnal cycle of air-sea feedback modifies the mean climate state through the following mechanism (Fig.1.1): The dominating solar heating during daytime stabilizes the ocean by warming the upper ocean. The vertical mixing is reduced and the mixed-layer depth becomes shallower. The shoaled mixed-layer amplifies the increase of SST during daytime. In the nighttime, the upward heat flux leads to a cooling of the SST, the upper ocean is destabilized. The enhanced turbulence deepens the mixed-layer depth and then releases the surface cooling to a deeper mixed-layer. Hence, the SST cooling in the nighttime is weakened in a deeper mixed-layer. Since the daytime warming is amplified and the night cooling is weakened, the daily-mean SST is increased. This implies that including the diurnal cycle of air-sea feedback into a coupled climate model, the simulated daily-mean SST is increased.

This mechanism has been systematically studied by Bernie et al. (2005, 2007, 2008). Based on a Coupled General Circulation Model (CGCM) which can reproduce the diurnal cycle of SST and the mixed-layer depth, it is demonstrated that including the diurnal cycle into the coupled GCM leads to a tropical wide warming of SST. The strongest warming occurs in the equatorial Pacific. The warming has a maximum of up to $0.3°C$ in the eastern tropical Pacific and reaches $0.2°C$ in the central and western Pacific. Ham et al. (2010) suggested that the cold bias

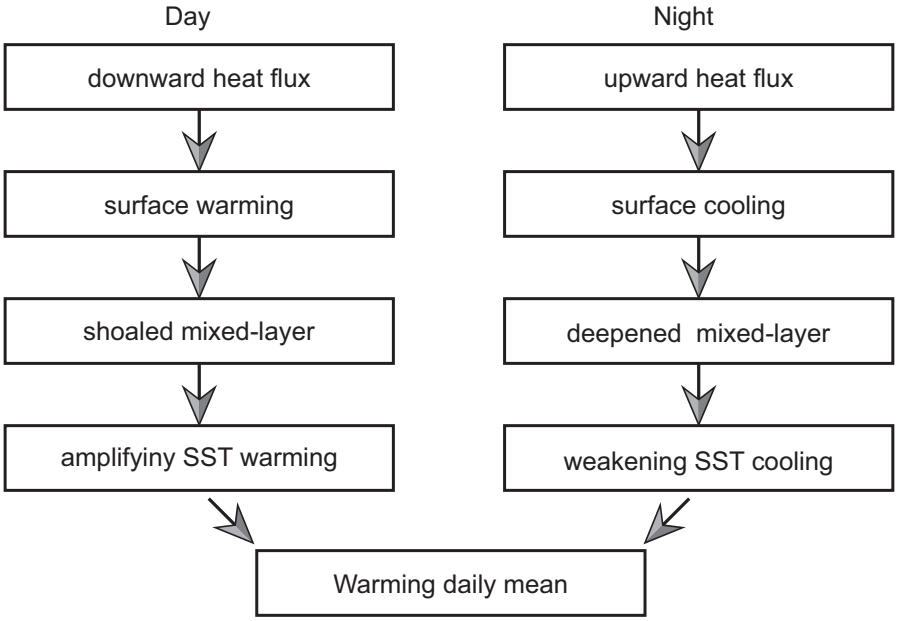

Fig. 1.1: Mechanism of the effects of diurnal cycle on mean SST as suggested by Bernie et al. (2005).

of the model over the equatorial western Pacific is reduced when increasing the coupling frequency. Ham et al. (2010) further show that the tropical warming initiated by the diurnal cycle can be amplified by the following air-sea feedback: The SST warming initiated by the diurnal cycle enhances the local atmospheric convection in the tropical Pacific, and consequently generates low-level westerlies in the western tropical Pacific and easterlies in the eastern tropical Pacific. The westerlies amplify the SST warming by enhancing the Ekman down welling, whereas the easterlies decrease the SST warming by enhancing the Ekman up welling.

Most of the studies about the diurnal cycle focus on the tropical and subtropical regions, because at low-latitudes, the diurnal range of SST is large and the static stability of the ocean is stable, thus the local effect is strong. However, the effects of diurnal cycle at the mid- and high-latitudes are not clear. Besides the local effect, the diurnal cycle in the tropics might be connected with the climate variability at higher latitudes. These global effects of the diurnal cycle need to be addressed.

1.2.2 Intra-daily fluctuations

In addition to the diurnal cycle, random intra-daily fluctuations are also one important component of intra-daily air-sea interactions. For example, Stochastic fluctuations in precipitation and solar radiation can be caused by the generation and development of convective clouds. Fluctuations in evaporation, latent heat flux and momentum flux can be caused by small-scale turbulence. These fluctuations generally have high frequency and small spatial scales. The importance of fluctuations for the climate system has been supported by many previous studies (Palmer 2001; Kuhlbrodt and Monahan 2003; Williams 2012). For example, by implementing a stochastic physics parametrization to atmospheric part of the coupled model of the European Centre for Medium-Range Weather Forecasts (ECMWF), Palmer (2001) has found that the cold tropical sea-surface temperature bias is reduced by around $0.2°C$.

As shown in Fig.1.2, the effects of fluctuations in buoyancy fluxes on oceanic state depend on the oceanic static stability. In regions where stratification is mostly stable, such as in the tropical and subtropical ocean, fluctuations in buoyancy fluxes tend to increase the mixed-layer depth. This can be explained through the following mechanism: In a statically stable water column, the buoyant anomalies, caused by the precipitation and surface heat, cannot significantly shoal the mixed layer. In contrast, the dense anomaly caused by evaporation and surface cooling destabilizes the water column. The destabilization initiates convection and vertical mixing, and thus deepens the mixed-layer. Therefore, in mostly stable ocean, the mixed-layer depth tends to be increased by normally distributed fluctuations. However, in mostly unstable regions, the convective mixing is strong, the dense anomaly cannot further enhance the mixing, the fresh anomaly, however, increases the static stability and thus decrease the mixing. Therefore, the mixing tends to be weakened by fluctuations in the unstable ocean.

This mechanism of the stochastic fluctuations has been verified by Beena and von Storch (2009). By coupling the ocean general circulation model MPIOM to an empirical model of atmospheric dynamics, they found that the fluctuating buoyancy anomalies tend to increase convective mixing in mostly stable regions, such as in the subtropical ocean in the Southern Hemisphere and tend to reduce the mixing in the Southern Ocean. To capture the air-sea feedbacks in the coupled system, the climate impact of the stochastic fluctuations in air-sea fluxes has been further studied by Williams (2012). They apply the stochastic fluctuations to the air-sea buoyancy fluxes in a 3-hourly coupled climate model (ECHAM4.6-OPA).

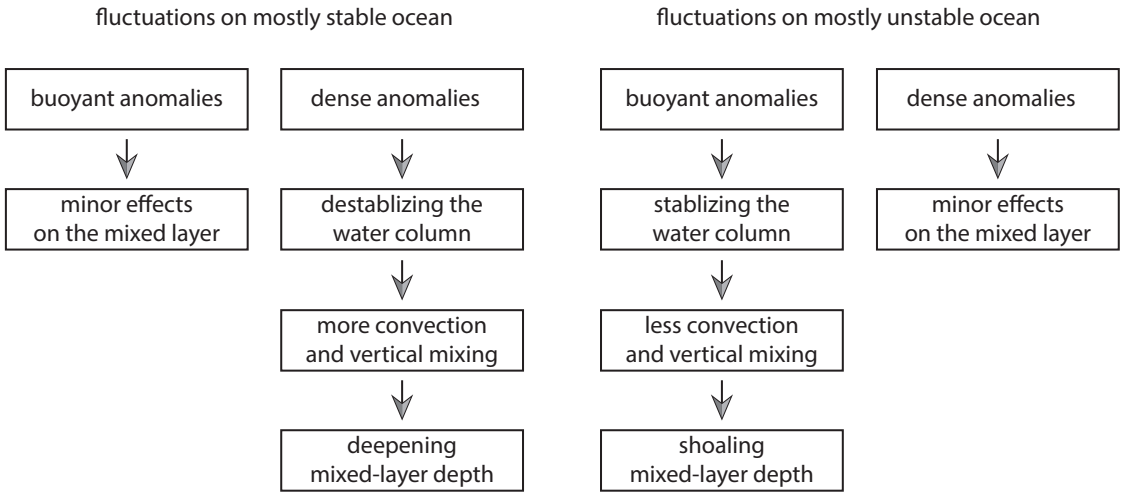

Fig. 1.2: Mechanism of the effects of fluctuation on mean SST as suggested by Beena and von Storch (2009).

By perturbing the net fresh water flux and net heat flux separately, they found that the oceanic mixed-layer is deepened systematically, the surface ocean is cooled, the precipitation is decreased in ITCZ and is increased in the subtropics, and the Hadley cell is weakened.

In the experiments of those works, fluctuations are studied by including white noise into the climate system. For example, Williams (2012) represented fluctuations using white noise drawn from a uniform distribution between 0.5 and 1.5. Beena and von Storch (2009) also used white noises. The spatial distribution of the statistics of the fluctuations, such as those of variance and extremes, are not considered. The temporal evolutions, such as seasonal variations, have not been studied. Additionally, fluctuations depend on the character of the related surface flux. For example, the fluctuations of precipitation are different from that of the wind stress, the fluctuations of the zonal wind stress are different with that of the meridional wind stress. However, these differences are normally ignored in the previous works. To reasonably consider the spatial distribution of temporal evolution of the statistics characters of the air-sea fluxes, it is better to involve the intra-daily fluctuations in the coupling system by increasing the air-sea coupling frequency.

The diurnal cycle and the random intra-daily fluctuations affect the climate system simultaneously through different mechanisms (Fig.1.1and 3.3). For example, in the tropical and subtropical ocean, the diurnal cycle tends to shoal the mixed layer depth and warm the SST, whereas the random fluctuations tend to

deepen the mixed layer and cool the SST. However, in most of the previous works the effects of the diurnal cycle and the random fluctuations have been studied separately, their joint effects are not clear.

1.3 Aims of the thesis

In this thesis, the joint effects of diurnal cycle and intra-daily fluctuations are produced in MPI-ESM by increasing the air-sea coupling frequency from daily to hourly. This work aims to give the global distributions and the temporal evolutions of the basic statistics of intra-daily variabilities of the air-sea fluxes in the hourly coupled MPI-ESM.

In comparison with daily coupled MPI-ESM, the included intra-daily variabilities in hourly coupled MPI-ESM are partly caused by the different averaging interval during the coupling processes, and partly caused by the intra-daily air-sea feedbacks which can only be resolved by hourly coupled MPI-ESM. This work aims to differentiate the effects of intra-daily air-sea feedbacks from that of the different averaging interval.

The included intra-daily air-sea interactions can affect the climate state and the variability of the coupled system. This work aims to study the effects on the climate states of the air-sea fluxes, including in the Southern ocean, which has not been mentioned in previous works, and in the tropical Pacific. This work also aims to address the effects of the intra-daily air-sea interactions on the inter-annual variability – ENSO and to explain how the intra-daily air-sea interactions improve the simulation of ENSO asymmetry.

1.4 Outline of the thesis

This thesis contains three major chapters. Each chapter has its own abstract, introduction and conclusion, and hence can be read independently. Chapter 2 evaluates the performance of MPI-ESM with the standard daily coupling in comparison to observations, and analyses the changes to the hourly coupled MPI-ESM. Chapter 3 quantifies the statistics of the diurnal cycle and random intra-daily fluctuations of the air-sea fluxes at each grid point and studies the modes of the air-sea fluxes that lead to large-scale changes. Chapter 4 studies the interactions between the intra-daily air-sea feedback and the inter-annual variability of ENSO. A detailed outline of each chapter is given below.

Chapter 2:

To study the effects of intra-daily air-sea interactions, a coupled GCM which can simulate the diurnal cycle and random intra-daily fluctuations is an indispensable tool. Though MPI-ESM can be coupled once per hour, some studies are still needed to understand how the coupling frequency affects the model parametrizations. Whether the overall performance of the MPI-ESM is improved by increasing the coupling frequency also needs to be addressed. Besides a general overview of the model used in this study, the following questions are also addressed in this chapter:

- Can parametrizations directly respond to changes in coupling frequency?
- What are the biases in standard daily coupled MPI-ESM? Are they improved in the hourly coupled model?

Chapter 3:

The effect of the intra-daily air-sea feedback is discussed by comparing the simulated data of an hourly coupled MPI-ESM with those obtained from a daily coupled MPI-ESM. Since the diurnal cycle and random intra-daily fluctuations are the most important aspects of the intra-daily air-sea feedback, quantifying their strength at each grid point is essential to study their joint effect on the climate state. Further, the diurnal cycle and random fluctuations on each grid point lead to changes in the large-scale patterns of air-sea fluxes, understanding these large-scale modes of the air-sea fluxes is another purpose of this chapter. Hence, the following questions will be addressed in this chapter:

- What are the effects of increasing coupling frequency on the basic statistics of air-sea surface fluxes at grid point level?
- Which processes are responsible for the changes in basic statistics of air-sea fluxes?
- How does the intra-daily air-sea feedback affect large-scale patterns of air-sea fluxes?

Chapter 4: As Chapter 3 demonstrates that the intra-daily air-sea feedback at grid-point level is related to the large scale mode of the air-sea fluxes, it is worthwhile to investigate whether the air-sea feedback on intra-daily time scales can influence phenomena on longer time scales, such as ENSO. In the observation,

El Niño is stronger than La Niña. However, the simulated ENSO in many CMIP5 models, including the MPI-ESM, is almost symmetric. This chapter aims to address the following question:

- Can hourly coupling improve the model's ability in simulating the ENSO asymmetry, and if yes, why?

This thesis is closed with a discussion of results in Chapter 5.

Chapter 2

Model and model performance

To simulate intra-daily air-sea feedback, the coupling frequency between atmosphere and ocean in MPI-ESM is increased from daily to hourly. To confirm that the hourly coupling frequency of MPI-ESM leads to more realistic simulation of the general circulation, this chapter introduces the model parametrizations which are directly related to the coupling frequency, i.e. the parametrizations of air-sea fluxes and convection, and evaluates the biases of the simulated general circulation in the hourly and daily coupled experiments.

Increasing the air-sea coupling frequency from daily to hourly changes the Probability Density Functions (PDFs) of the momentum, heat and fresh water fluxes. The diurnal cycle of the net heat flux can be well simulated. The increased convective precipitation in most part of the equatorial oceans indicates that the convection scheme in MPI-ESM also responds to the intra-daily air-sea feedback.

Increasing the air-sea coupling frequency improves many aspects of the simulation. For example, the cold biases in the western equatorial Pacific and subtropical Southern Ocean and the warm biases in the high-latitude Southern Ocean are all decreased by up to 10%. The biases of the tropospheric westerlies around $60°S$ decrease by up to 10%. The warm biases of oceanic potential temperature decrease in most parts of the ocean by up to 20%. Hence, increasing the coupling frequency from daily to hourly improves the performance of MPI-ESM.

2.1 Introduction

Coupled General Circulation Models (CGCMs) are important tools to study atmospheric and oceanic phenomena. To study the effects of the intra-daily air-sea interactions on the climate system, it is curial to assess the ability of CGCMs in realistically simulating the intra-daily air-sea feedback, such as the diurnal cycle of SST and the random intra-daily fluctuations.

In the atmosphere, fluctuations originate to a considerable extent from the convection and the related processes. It is difficult to properly parametrize these fluctuations. In the ocean, modelling sub-grid scale turbulence and mixing via eddy parametrizations is also one primary error source. In addition, in most CGCMs, the exchange frequency of the atmospheric and oceanic information is restricted by the coupling frequency. The air-sea exchanges with frequency higher than the coupling frequency cannot be resolved by numerical models. As shown in Table 2.1, the coupling frequency in more than half of the fifth phase of the coupled model intercomparison project (CMIP5) models is once per day, including the Max Planck Institute for Meteorology Earth System Model (MPI-ESM). In these daily coupled models, diurnal cycles and random intra-daily fluctuations are not resolved.

A high air-sea coupling frequency is not used in most of the CGCMs is probably because that the coefficients used in calculating the turbulent air-sea fluxes are determined from measurements averaged over about one hour (Bradley 1968). The empirical coefficients used in the daily coupled CGCMs may not be appropriate for hourly coupled CGCMs. Despite this problem, hourly coupling can be realized with MPI-ESM. Using the low resolution version (MPI-ESM-LR), integrating for one year takes 8000s for daily coupling and 27000s for hourly coupling. When using an hourly coupling frequency in MPI-ESM, the applicability of the empirical coefficients and related parametrizations need to be confirmed. Additionally, the changes and improvements of the general circulation caused by increasing coupling frequency from once per day to once per hour need to be investigated.

The structure of this chapter is as follows: Section 2.2 describes the model and experiments used in this work. Section 2.3 describes the parametrizations related to the coupling frequency. Section 2.4 investigates the changes of the biases of MPI-ESM caused by including intra-daily air-sea feedback. Conclusions are drawn in Section 2.5.

Table 2.1: The coupling frequency of CMIP5 models

Interval	Model names		
24 h	BCC-CSM1.1	BCC-CSM1.1(m)	BNU-ESM
	CanESM2	CanCM4	CESM1(BGC)
	CESM1(CAM5)	CESM1(CAM5.1.FV2)	CESM1(FASTCHEM)
	CESM1(WACCM)	CMCC-CESM	CMCC-CMS
	CNRM-CM5	FGOALS-g2	FGOALS-s2
	FIO-ESM v1.0	HadCM3	HadGEM2-AO
	HadGEM2-CC	HadGEM2-ES	IPSL-CM5A-LR
	IPSL-CM5B-LR	IPSL-CM5A-MR	**MPI-ESM-LR**
	MPI-ESM-MR	**MPI-ESM-P**	NorESM1-M
	NorESM1-ME		
3 h	ACCESS1.0	ACCESS1.3	EC-Earth
	MIROC4h	MIROC-ESM	MIROC-ESM-CHEM
2 h	GFDL-CM2.1	GFDL-CM3	GFDL-ESM2G
	GFDL-ESM2M	INM-CM4	NCEP-CFSv2
1.5 h	CMCC-CM	GISS-E2-H	
1 h	MIROC5	MRI-CGCM3	MRI-ESM1
0.5 h	GISS-E2-H-CC	GISS-E2-R	GISS-E2-R-CC

2.2 Model and experiments

2.2.1 The coupled model: ECHAM6/MPIOM

Max Planck Institute for Meteorology Earth System Model (MPI-ESM) is used in this work. The MPI-ESM consists of ECHAM6 for the atmosphere (Stevens et al. 2013) and MPIOM for the ocean (Jungclaus et al. 2006, 2010).

ECHAM6 is an atmospheric general circulation model used for the CMIP5. In comparison with ECHAM5, the most important changes concern the short wave radiative transfer. Changes in the short wave physics have been combined with a revised surface albedo scheme and new representation of cloud optics. Over the ocean, ECHAM5 treated the surface albedo as constant, whereas ECHAM6 accounts for zenith angle (Stevens et al. 2013). Here we use the model MPI-ESM with the low resolution configuration. i.e. MPI-ESM-LR, meaning that ECHAM6 is run at T63 horizontal resolution (approximately 1.875° on a Gaussian grid) with 47 vertical levels. The atmospheric model time step is 600s.

The oceanic component, MPIOM, is a free-surface ocean general circulation model including a sea-ice model (Jungclaus et al. 2006). MPIOM is based on primitive equations for a Boussinesq fluid on a rotating sphere using a z-coordinate system. The version used in this thesis is formulated on a horizontal GR15 grid, which has two grid poles, one over Antarctic and one over southern Greenland. The horizontal resolution is about 1.5°. The model applies 40 vertical levels with a 12m surface layer and the first 20 layers are distributed over the upper 700m. The ocean model time step is 3600s.

ECHAM6 and MPIOM are coupled without flux adjustments using the Ocean-Atmosphere-Sea-Ice-Soil (OASIS3) coupler (Valcke et al. 2003), in which the air-sea fluxes of momentum, heat and fresh water are averaged over each coupling interval. After averaging, the fluxes are exchanged between the atmospheric and oceanic components. Thus, interactions between the atmosphere and the ocean can occur only on time scales longer than the coupling interval.

2.2.2 The experiments

Two experiments are performed with MPI-ESM-LR that are identical except for the coupling frequency. The first one has a coupling frequency of once per day and is called *Daily Coupling* (*DC*) experiment. The other experiment has a coupling frequency of once per hour and is called *Hourly Coupling* (*HC*) experiment.

Both of the experiments are pre-industrial control simulation with constant external forcing conditions corresponding to the year 1850, e.g. no anthropogenic land use, no aerosol climatology, constant pre-industrial ozone climatology, constant pre-industrial solar radiation and constant orbital parameters. Greenhouse gas concentrations are also constant, e.g. $CO_2 = 284.725$ ppm, $CH_4 = 0.79097924$ ppm and $N_2O = 0.2754250$ ppm. Dynamic vegetation is activated. Each experiment is run for multi centuries so that the atmosphere and the upper ocean have reached a quasi-equilibrium. We use daily mean data of the last 100 years of the two experiments and 50 years of hourly mean data of experiment HC to study the changes induced by different coupling frequencies.

2.3 Parametrizations affected by coupling frequency

The parametrizations in MPI-ESM, that are important for this work, are introduced as follows.

2.3.1 The air-sea fluxes

If the coupling frequency is once per day, the air-sea fluxes are computed in the atmosphere model component using SST and ocean surface currents which are averaged over one day. The computed air-sea fluxes are also averaged over one day in the coupler OASIS3 and then passed to the ocean component. Using a coupling frequency of once per hour, the hourly mean SST and ocean surface currents are used to compute air-sea fluxes, which are also averaged every hour. Therefore, the air-sea fluxes are directly influenced by the coupling frequency. Here, the parametrizations of the considered air-sea fluxes and these relations with coupling interval are addressed.

Wind stress

The wind stress $\boldsymbol{\tau}$ is calculated from the velocity difference between the near surface wind speed and the ocean surface currents (Pacanowski 1987):

$$\boldsymbol{\tau} = \rho\, C_D |\mathbf{W} - \mathbf{V}|(\mathbf{W} - \mathbf{V}) \tag{2.1}$$

where ρ is the density of air and C_D is the drag coefficient. $\mathbf{W}$ is the wind vector at the lowest atmosphere level and $\mathbf{V}$ is the ocean velocity vector of the surface level.

In the model coupling process, **V**, generated in MPIOM, is averaged over the coupling interval, i.e. one day in experiment DC and one hour in experiment HC. In the atmospheric component, the calculated momentum flux is also averaged over a coupling interval. Because of the difference of **V** and the coupling interval, the statistics of the momentum flux are different in experiment HC and DC. As an example, Fig.2.1 compares the probability density function (PDF) of momentum flux in experiment HC and DC. The probability of the extreme wind stress, which is weaker than 0.15 $N\,m^{-2}$ or stronger than 0.6 $N\,m^{-2}$, is higher in experiment HC than in experiment DC. The increase of the probability of extremely weak and strong wind stress may originate from intra-daily fluctuations which can be captured by experiment HC. The details of the momentum flux will be discussed in more details in Chapter 3.

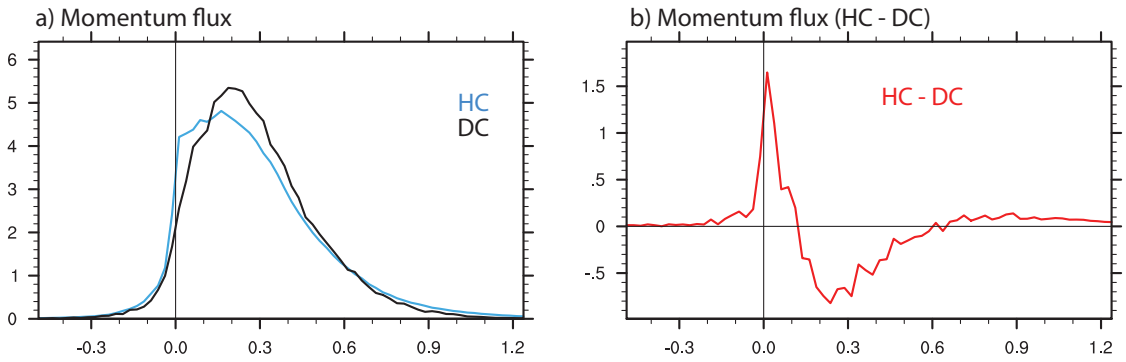

Fig. 2.1: (a) Probability density function (PDF, %) of the momentum flux ($N\,m^{-2}$) at a grid point near 60°S 180°E in experiment HC (black) and DC (blue). (b) Difference between the two PDFs (HC - DC).

Net heat flux

The net heat flux Q_{srf} is defined as the sum of sensible and latent heat flux and short wave and long wave radiation:

$$Q_{srf} = Q^{se}_{srf} + Q^{la}_{srf} + Q^{lw}_{srf} + Q^{sw}_{srf} \tag{2.2}$$

where Q^{se}_{srf}, Q^{la}_{srf}, Q^{lw}_{srf} and Q^{sw}_{srf} indicate the sensible, latent, long wave and short wave heat fluxes, respectively.

As suggested by Oberhuber (1993), the sensible and latent heat flux are parametr-

ized as:

$$Q^{se}_{srf} = \rho_a \, c_a \, C_H \, V_{10m} \, (T_a - T_{srf}) \tag{2.3}$$

$$Q^{la}_{srf} = \rho_a \, L_{srf} \, C_L \, V_{10m} \, (q_a - q_{srf}) \tag{2.4}$$

where ρ_a, c_a and L_{srf} are constants denoting the air density, the specific capacity for air and the latent heat of vaporization or sublimation. Variable coefficients of sensible heat flux C_H and latent heat flux C_L are formulated according to Large and Pond (1982). V_{10m} indicates the 10m wind speed. T_a and q_a are the air temperature and specific humidity at the 2m level. T_{srf} is the ocean model upper layer temperature or the ice/snow layer skin temperature. q_{srf} is specific humidity at the surface.

Long wave and short wave radiation are parametrized as:

$$Q^{lw}_{srf} = \epsilon\sigma T_a^4(0.39 - \, 0.05\sqrt{e/100}(1 - \chi n^2) + 4\epsilon\sigma T_a^3(T_{srf} - T_a) \tag{2.5}$$

$$Q^{sw}_{srf} = \, (1 - \alpha_{srf})Q^{incsw} \tag{2.6}$$

where n, ϵ and σ are fractional cloud cover, surface thermal emissivity and the Stephan-Boltzmann constant, respectively. e is the saturation vapour pressure calculated based on the formulae of Buck (1981). χ is the cloudiness factor. Q^{incsw} is the incident short wave radiation which is the function of the solar zenith angle and is provided as part of the forcing data. α_{srf} is the surface reflectivity.

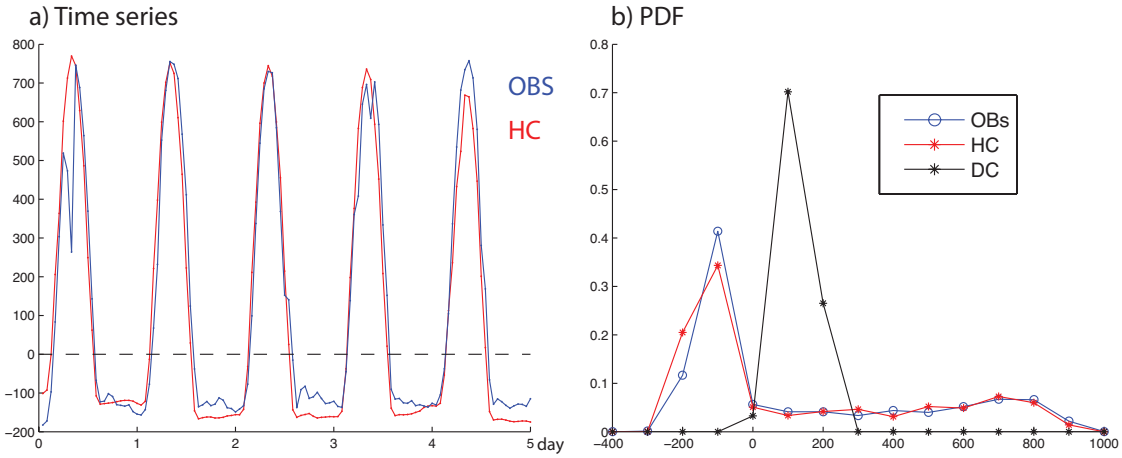

Fig. 2.2: (a) Time series of hourly net heat flux for observation (blue) and experiment HC (red), and (b) the respective probability density function (PDF %) ($W\,m^{-2}$) at a grid point near 0° 140°W for observation(blue), experiment HC (red) and experiment DC (black)The observation is obtained from the TOGAR COARE dataset.

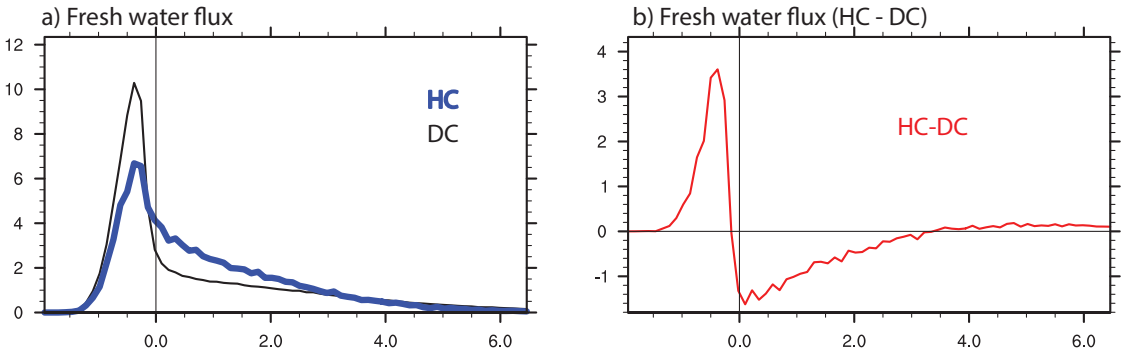

Fig. 2.3: (a) Probability density function (PDF %) of the fresh water flux ($mm\,day^{-1}$) at grid point $60°S$ $180°$ in experiment HC (black) and DC (blue), and (b) is the difference between the two PDFs (HC - DC).

In the daytime, the net heat flux is dominated by the short wave radiation which has a diurnal cycle. In the nighttime, it is dominated by the sum of the long wave radiation, sensible heat flux and latent heat flux. Fig.2.2a shows the dominant features of heat fluxes in terms of an example. If the coupling interval is one hour, the simulated diurnal cycle of the net heat flux (red) agrees well with observations (blue). However, if a coupling interval of one day is used, the information of the diurnal cycle is lost by the daily averaging. As shown in Fig.2.2b, the PDF of net heat flux with a diurnal cycle (red) is very close to observations (blue). Both have a high probability of negative values and extremely large positive values ($> 300W\,m^{-2}$). Most of the negative values and extreme positive values disappear if a coupling interval of one day is used (black).

Fresh water flux

The fresh water flux at the sea level Q_ζ is defined as:

$$Q_\zeta = P - E + R + G \tag{2.7}$$

where P, E, R and G are fluxes of fresh water in units of $mm\,day^{-1}$ due to precipitation, evaporation, river run off and glacial melt water, respectively. E is calculated from the latent heat flux as:

$$E = Q_{srf}^{la}/(L_{srf}\rho_w) \tag{2.8}$$

where ρ_w the density of sea water, L_{srf} is the latent heat of vaporization or sublimation as appropriate for water or ice/snow surface.

The negative fresh water flux is dominated by the evaporation and the positive flux is dominated by the precipitation. As an example, the PDFs of the simulated fresh water fluxes at one grid point are shown in Fig.2.3a. For the hourly coupled experiment, the maximum of the PDF is located at values around $-0.2\ mm\,day^{-1}$ and the PDF has a long positive tail. When using a coupling interval of one day, some of the large negative values ($< -0.02\ mm\,day^{-1}$) and large positive values ($> 3.5\ mm\,day^{-1}$) are filtered before being sent to the oceanic component (Fig.2.3b). This implies that, considering intra-daily fluctuations by increasing the coupling frequency, the extremely strong evaporation events ($< -0.02\ mm\,day^{-1}$), and extremely strong precipitation events ($> 3.5\ mm\,day^{-1}$) are captured.

2.3.2 The convection scheme

The temporal and spatial character of convection is affected by the diurnal cycle of SST. Meanwhile, the convection is able to affect the inter-annual variability of SST and particularly ENSO (Rädel et al. 2016). This interaction is further studied in Chapter 5. Here, the convection scheme in MPI-ESM and its relationship to the coupling interval is addressed.

In ECHAM6, the shallow and mid-level (elevated moist layer) convection scheme follows the Tiedtke formulation(Tiedtke 1989), whereas deep (including congestus) convection follows the Nordeng formulation (Nordeng 1994). The shallow convection is defined as cloud depths smaller than 200 hPa. For deep convection the mass-flux is determined by assuming that convection removes Convective Available Potential Energy (CAPE) over a given time scale. The intensity of shallow convection is based on the budget of the moist static energy, i.e. the convective flux at cloud base equals the contribution of all other physical processes when integrated over the subcloud layer. Finally, mid-level convection can occur for elevated moist layers, and its mass flux is set according to the large-scale vertical velocity.

The trigger condition of the convection depends on the difference of virtual temperature between the air parcel and the environment:

$$T_v^p + \Delta T > T_v^{env} \tag{2.9}$$

where T_v^p is the virtual temperature of the air parcel, T_v^{env} is the virtual temperature of the environment. ΔT is related to the temperature variance in the

planetary boundary layer. Thus, the trigger condition is determined by the properties of the air parcel at the lifting level and on the vertical profile of virtual temperature in the large-scale environment.

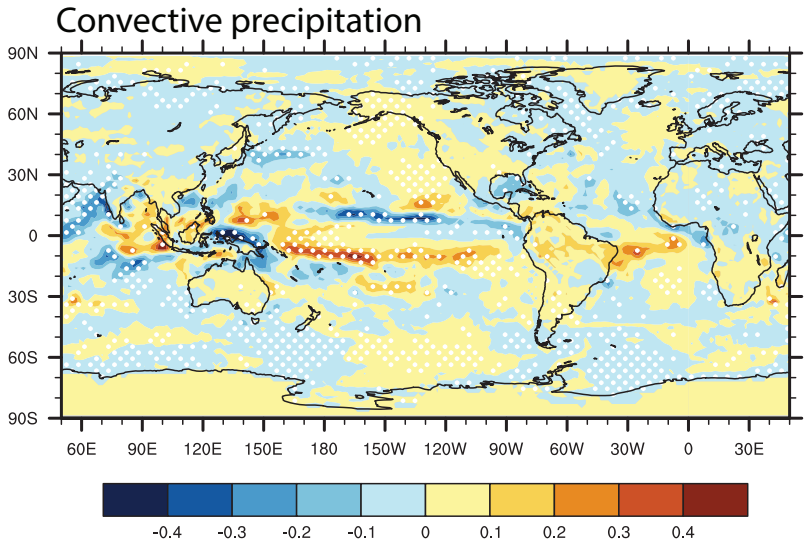

Fig. 2.4: Differences in the convective precipitation ($mm\,day^{-1}$) between the hourly coupled experiment and daily coupled experiment (HC - DC). The dots indicate no-zero differences at 5% significance level following a t-test.

The average of SST over one coupling interval is sent to the atmospheric component to calculate the heat flux, such as the latent and sensible heat flux. The heat fluxes influence the temperature of air, T_v^{env} and T_v^p, and then the convection. In the hourly coupled experiment, an hourly averaged SST is used to calculate the air temperature. In the daily coupled experiment, the air temperature is calculated from daily averaged SST. Since the intra-daily variability of SST is removed by the daily averaging, the convection cannot be influenced by the diurnal cycle of SST. Therefore, the different coupling interval can lead to significant difference in convection. As shown in Fig.2.4, the difference of the convective precipitation has the maximum in the tropical ocean. Including the diurnal cycle of SST leads to more precipitation in the eastern tropical Indian Ocean, the equatorial central Pacific, and tropical Atlantic, and less precipitations in the north western Indian Ocean, the western equatorial Pacific and the central tropical Pacific along $10°N$. This indicates that the convection is sensitive to the diurnal cycle of SST.

Increasing the coupling frequency from daily to hourly is important for surface fluxes and convections and therefore might influence the large-scale model biases.

2.4 Changes in model biases due to increasing coupling frequency

As the air-sea fluxes interact with the large-scale circulation of atmosphere and ocean, increasing coupling frequency leads to the change in the atmosphere and deeper ocean.

In comparison with the observations, the simulated SST in experiment DC is too warm in the Southern Ocean (south of $45°N$) and too cold in the Pacific and Indian Ocean (Fig.2.5a). Especially in the equatorial central Pacific the simulated equatorial cold tongue extends too far west and is too strong, which is a common bias in many CGCMs (Wittenberg et al. 2006). When increasing the coupling frequency from once per day to once per hour, the SST is generally increased in the tropical ocean (Fig.2.5b), with the maximum in the western Pacific warm pool by 0.1 $°C$. In the central and eastern equatorial Pacific the SST is decreased with a maximum of -0.1 $°C$. In the subtropical oceans of the northern Hemisphere, an increase of SST is found in the Bay of Bengal and the Atlantic, whereas a pronounced decrease is found along $20°N$ in the Pacific and the Arabian sea. In the southern Hemisphere, the SST is increased in latitudes ($20°S - 50°S$). In the high latitudes, south of $50°S$ and north of $45°N$, the SST is generally decreased with maximum values up to -0.5 $°C$. Hence, the warm biases in the Southern Ocean are decreased by up to 10%, whereas The cold biases in the western tropical Pacific, south Pacific and south Indian Ocean are decreased by around 10%.

The SST warming over the equatorial Pacific warm pool may be associated with the Madden-Julian Oscillation (MJO) and El Niño-Southern Oscillation (ENSO). The significant change of the magnitude and gradient of SST in the Bay of Bengal and Indian Ocean can affect the formation of the onset vortex of the Asian summer monsoon (Wu et al. 2012). Since the mean of SST is decreased in the Southern Ocean and increased in the subtropical ocean, the meridional SST gradient around $60°S$ is increased and may result in an increase of westerlies.

The potential temperature of the ocean is defined as the temperature that a parcel of water would have if it were moved adiabatically to a reference pressure of the ocean surface. The potential temperature in the ocean model is determined by the parametrizations of eddies, diapycnal mixing, and the simulated large scale circulation and inter basin exchanges. Changing the coupling frequency may influence the mixing and circulation and, thus, the potential temperature of the ocean.

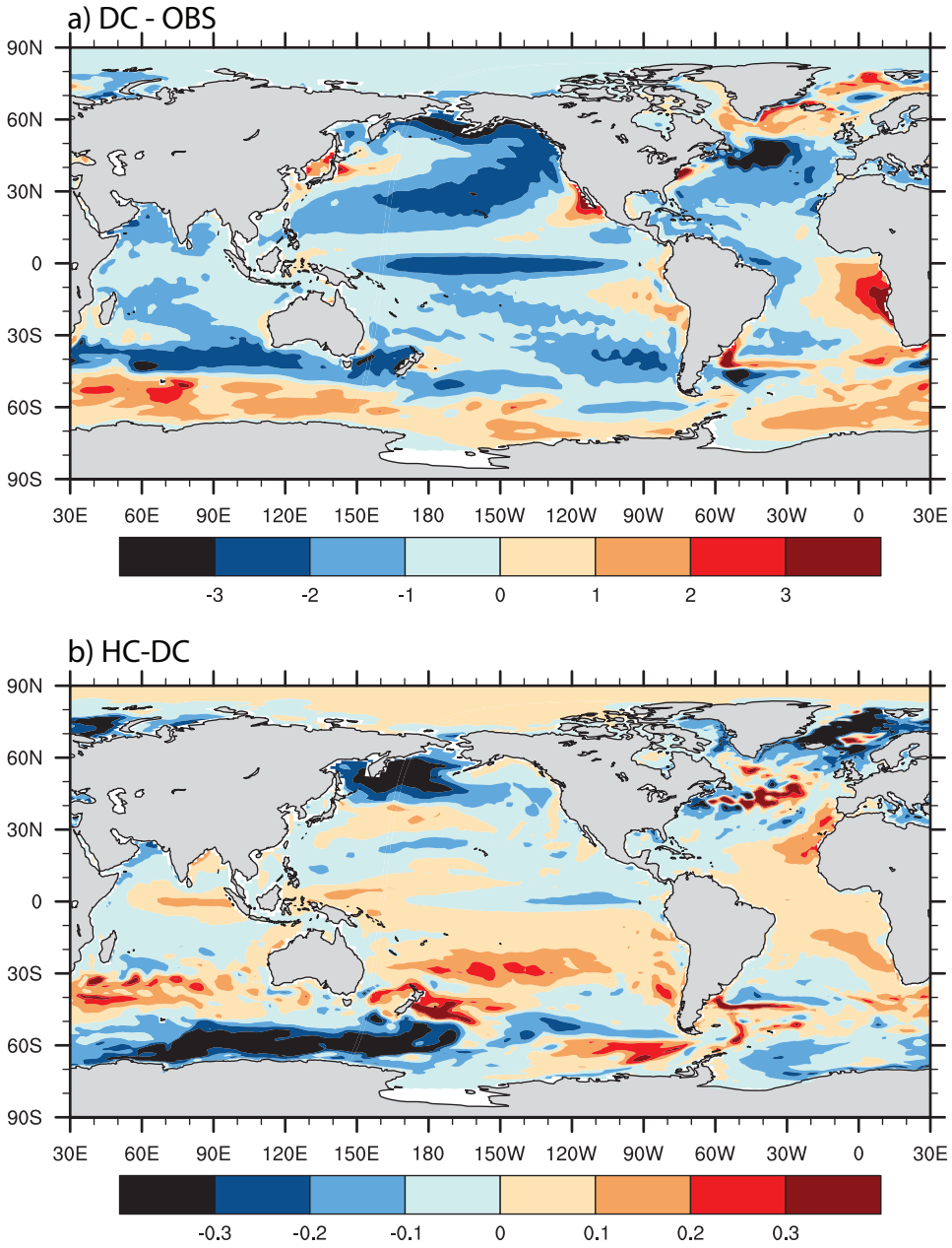

Fig. 2.5: (a) The bias of SST in experiment DC (DC - OBS) ($^{\circ}C$), (b) The difference of SST between experiment HC and DC (HC-DC) ($^{\circ}C$).

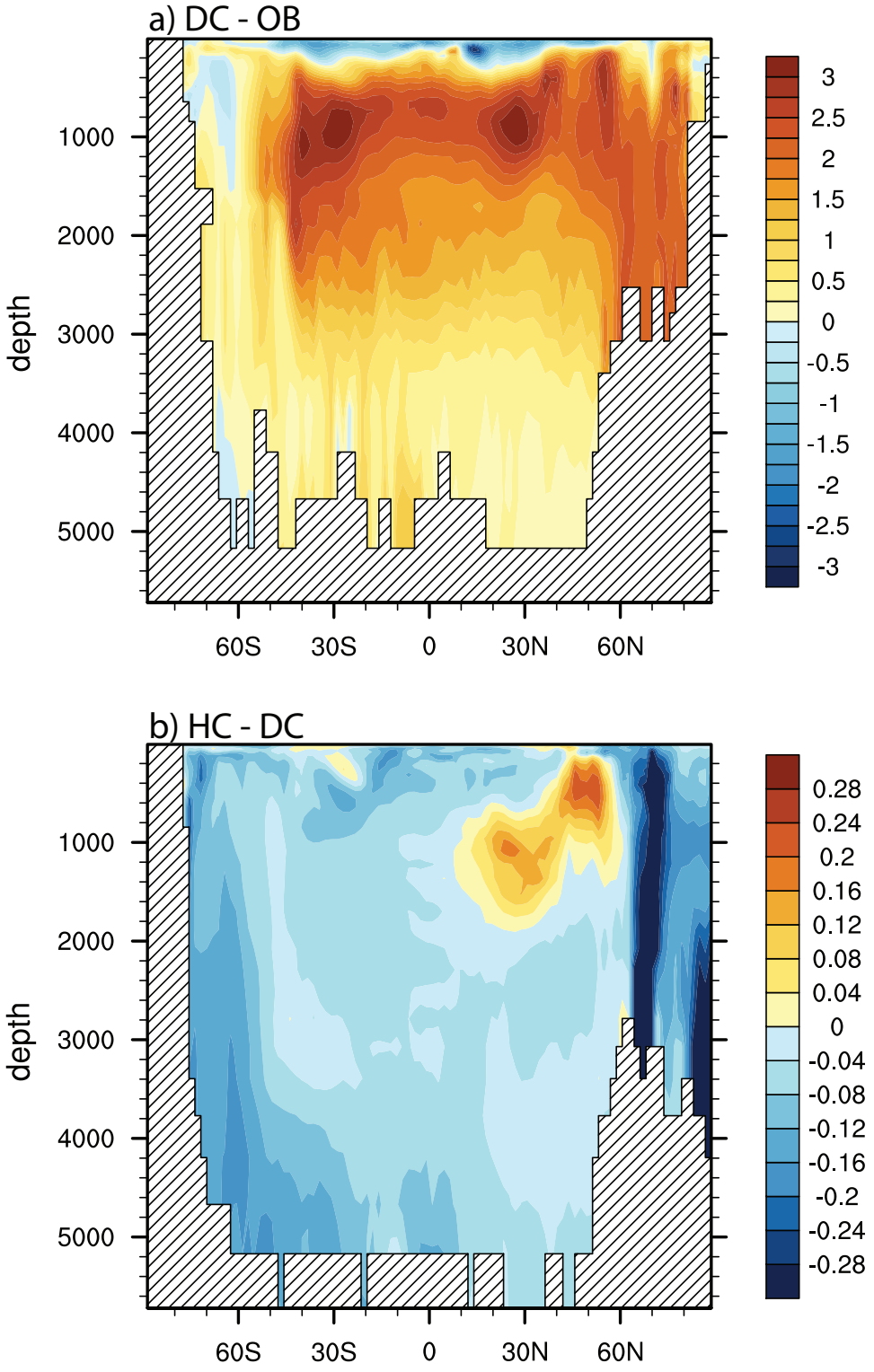

Fig. 2.6: (a) The bias of the zonal mean of the potential temperature (DC-OBS) ($^{\circ}C$), (b) The difference of the zonal mean of the potential temperature (HC-DC) ($^{\circ}C$).

Fig.2.6a compares the zonal mean of the simulated ocean potential temperature in experiment DC with the data from the Polar Science Centre Hydrographic Climatology (PHC3) (Levitus et al. 1998; Steele et al. 2001). The ocean of MPI-ESM is too warm at intermediate levels and in the deeper ocean . The maximum of the warm biases is located around 1000 m, north of $50°S$. At latitudes north of $50°N$, the warm biases are larger than $2°C$ throughout all depths.

As shown in Fig.2.6b, when increasing the coupling frequency from once per day to once per hour, the potential temperature is decreased everywhere except for a region with warming above 2000m at latitudes of $30°N - 60°N$. The warming might be related to the biases caused by the outflow through Gibraltar from the Mediterranean Sea. The maximum of the decrease is up to $0.25°C$ north of $60°N$. At latitudes south of $30°S$, the decrease is amplified with depth with the maximum around $0.15°C$. The cooling of the potential temperature at high latitude is consistent with the cooling of SST (Fig.2.5b) and the deepening of mixed layer depth, indicating more-intensive convection and more heat release to the atmosphere. Hence, the warm bias north of $50°N$ is decreased by up to 10%, the bias in the Southern Ocean is decreased by up to 20%.

The westerly wind belt in the troposphere is caused by a combination of the Earth's rotation and the meridional air temperature gradient with cold air in the polar region and warmer air towards the equator. In comparison with observations (Fig.2.7a), the westerly wind at $60°S$ is underestimated in experiment DC. The bias has a maximum value of 5 $m\ s^{-1}$ at 300 hPa. As increasing the coupling frequency increases the meridional gradient of SST in the Southern Ocean, the meridional gradient of the atmosphere temperature is increased there. Based on the thermal wind relation, the westerly wind in the troposphere is also increased. As shown in Fig.2.7b, the zonal mean westerly wind throughout the troposphere at $60°S$ is systematically enhanced with values up to $0.5m\ s^{-1}$. Hence, the bias is decreased by around 10% when increasing the coupling frequency to once per hour. The increased westerly wind can in turn influence the SST by increasing the momentum flux and mixing, enhancing the northward Ekman transport and causing the ocean to lose more latent and sensible heat flux to the atmosphere.

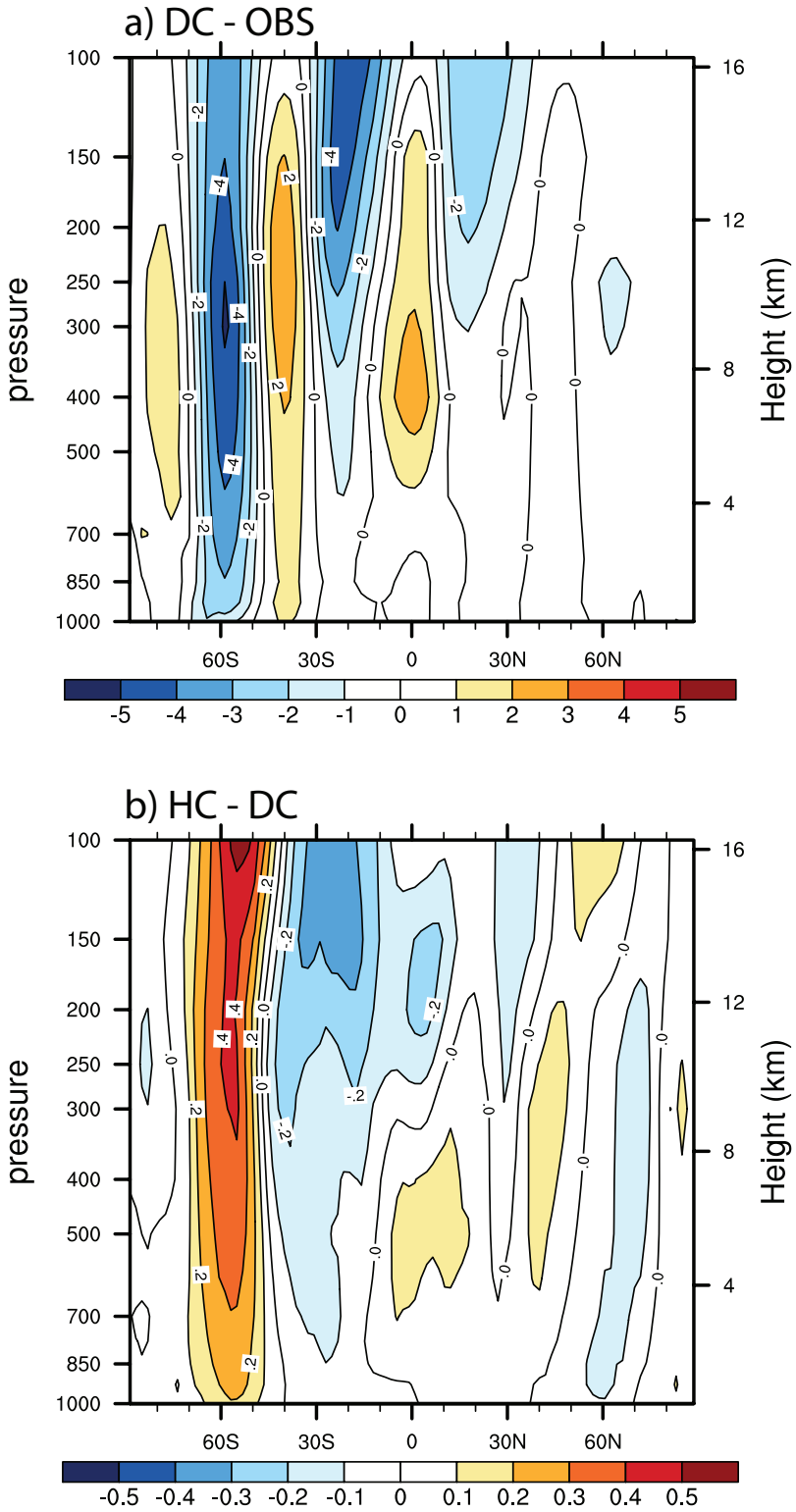

Fig. 2.7: (a) The bias of the zonal mean of troposphere zonal wind (DC-OBS) (ms^{-1}), (b) The difference of the zonal mean of troposphere zonal wind (HC-DC) (ms^{-1}).

2.5 Conclusion

This work shows that increasing the coupling frequency from daily to hourly, enables the model to simulate intra-daily air-sea feedbacks, and thus improves the simulation of many aspects of the general circulation in both atmosphere and ocean.

The parametrizations of the air-sea fluxes are appropriate in the hourly coupled MPI-ESM. The involved random intra-daily fluctuations increase the probability of momentum fluxes which are extremely weak or extremely strong as well as the probability of the fresh water fluxes with values around $-0.1\,mm\,day^{-1}$. The diurnal cycle of the net heat flux is well simulated when increasing the coupling frequency to hourly. Furthermore, the convective precipitation in most parts of the equatorial ocean is enhanced in the hourly coupled model. This indicates that the convection scheme used in daily coupled MPI-ESM can respond to intra-daily air-sea feedbacks.

In MPI-ESM, increasing the coupling frequency from once per day to once per hour overall leads to improvements of the model performance. In the daily coupled MPI-ESM, the simulated SST is too warm in the Southern Ocean and too cold in the central equatorial Pacific. The simulated oceanic potential temperature is too warm at intermediate levels and in the deeper ocean. The westerly wind at latitudes around $60°S$ is underestimated. When increasing the coupling frequency, the simulated SST is increased in the subtropical and tropical ocean and decreased in the high latitude ocean. The westerly wind increases around $60°S$ throughout the troposphere. The potential temperature of the ocean decreases globally, especially at high latitudes. Therefore, the cold biases of SST in the western equatorial Pacific and in subtropical oceans in the Southern Hemisphere are decreased. The warm biases in the Southern Ocean are decreased. The decreases of the SST biases amount to 10%. The biases of the westerly wind at $60°S$ are also decreased by up to 10%. The warm biases of the potential temperature in the ocean are decreased by up to 20% in the Southern Ocean.

It can be concluded that increasing the coupling frequency improves the performance of MPI-ESM. Processes such as intra-daily air-sea feedbacks, can be simulated in the hourly coupled experiment but cannot be resolved in the daily coupled experiment. Studying these processes is necessary to understand interactions in the climate system across different time scales. It may also be important for future model development. Since the coupling frequency directly influences air-sea fluxes, which in turn can alter the large-scale general circulation, in this

thesis, the processes through which intra-daily air-sea feedbacks at grid-point level influence the large scale modes of the air-sea fluxes are studied in Chapter 3. Further, the processes through which the air-sea feedbacks on intra-daily time scales impact a phenomenon on inter-annual time scales, ENSO, are investigated in Chapter 4.

Chapter 3

Effects of coupling frequency on the air-sea fluxes

This chapter analyses the changes in the air-sea fluxes of momentum, heat and fresh water caused by increasing the ocean-atmosphere coupling frequency from once per day to once per hour in the Max Planck Institute Earth System Model (MPI-ESM). We diagnose the relative influences of daily averaging and high-frequency feedbacks on the basic statistics of the air-sea fluxes at grid point level and quantify the feedback modes responsible for large scale changes in fluxes over the Southern Ocean and the equatorial Pacific.

Coupling once per hour instead of once per day reduces the mean of the momentum flux magnitude by up to 7% in the tropics and increases it by up to 10% in the Southern Ocean. These changes result solely from feedbacks between atmosphere and ocean occurring on time scales shorter than one day. The variance and extremes of all the fluxes are increased in most parts of the ocean. Exceptions are found for the momentum and fresh water fluxes in the tropics. These increases result mainly from the daily averaging, whereas the decreases in the tropics are caused by the high-frequency feedbacks. The increases in variance are substantial, reaching up to 50% for the momentum flux, 100% for the fresh water flux, and a factor of 15 for the net heat flux. These diurnal and intra-diurnal variations account for up to 50% to 90% of the total variances and exhibit distinct seasonality.

The high-frequency coupling can influence the large-scale feedback modes that lead to large-scale changes in the magnitude of wind stress over the Southern Ocean and equatorial Pacific. In the Southern Ocean, the dependence of the SST-wind-stress feedback on the mean state of SST, which is colder in experiment HC, leads to an increase of westerlies. In the equatorial Pacific, Bjerknes feedback in

experiment HC reveals a diurnal cycle during El Niño events, with the feedback being stronger in the nighttime than in the daytime, and no clear diurnal cycle during La Niña events. This asymmetry might lead to the decrease of wind stress in the equatorial Pacific in the hourly coupled experiment.

3.1 Introduction

The atmosphere and ocean are coupled by continuous exchanges of momentum, heat and fresh water. So far the diurnal cycle and the intra-diurnal fluctuations of these exchanges, which result mainly from atmospheric turbulence, are generally not resolved by state-of-the-art coupled climate models that usually use a coupling frequency of once per day. For example, more than half of the CMIP5 models that contributed to the fifth assessment report (AR5) of IPCC, including the Max Planck Institute Earth System Model (MPI-ESM), exchange fluxes between atmosphere and ocean once per day (see Table 2.1 in Chapter 2). Consequently, air-sea exchanges on time scales shorter than one day are excluded from most CMIP5 models. This chapter uses MPI-ESM, a CMIP5 model, to study the effects induced by increasing the coupling frequency from daily to hourly.

Previous studies show that increasing the coupling frequency can lead to significant changes in many aspects of the coupled system, such as those on the simulation of sea surface temperature (SST), Madden-Julian Oscillation (MJO), and El Niño- Southern Oscillation (ENSO). By increasing the coupling frequency from once per day to once per 1- or 3-hour, the mean equatorial SST is warmed by as much as $1°C$, which improves the agreement with observations (Danabasoglu et al. 2006). The meridional SST gradient in the North Atlantic is decreased (Guemas et al. 2013). The cold bias in the eastern tropical Pacific is reduced (Misra et al. 2008). For the variability on intra-seasonal and inter annual scales, including the diurnal cycle in the SST strongly influences the onset and intensity of MJO convection (Seo et al. 2014) and leads to a distinct improvement of the simulated intra-seasonal oscillation signal (Ham et al. 2014). The simulated MJO is stronger and more coherent (Bernie et al. 2008). The simulation of ENSO is also improved (Danabasoglu et al. 2006; Terray et al. 2012). Most of the changes considered in previous studies are the consequences of changed air-sea fluxes due to an increased coupling frequency. However, few studies have systematically addressed the direct impact of the coupling frequency on the air-sea fluxes. This study aims to fill this gap by addressing the influence of high-frequency coupling on both the basic statistics of air-sea fluxes at grid point level and the feedbacks leading to large scale air-sea flux changes.

The basic statistics of the air-sea fluxes are known to be important for the simulated climate. For example, Walin (1982) found that the mean heat flux at the sea surface directly determines the surface poleward branch of the meridional circulation. Tziperman (1986) revealed that time-mean density and velocity

fields are forced by the mean wind stress and heat fluxes at the upper surface of the ocean. Not only the long-term mean but also the fluctuation and associated variance of the air-sea fluxes play an important role in determining the general circulation of the climate system. Kuhlbrodt and Monahan (2003) found that the variability of surface fluxes leads to frequent deep convection and more deep water formation in the Labrador Sea. It was also found that the fluctuating fluxes change the intensity and the depth of vertical mixing, SST, Hadley circulation, and sea surface net upward water flux (Beena and von Storch 2009; Williams 2012). The extremes resulting from atmospheric turbulence or the diurnal cycle can also influence the simulated climate. Bernie et al. (2007) found that extremes related to the diurnal cycle of solar insolation affect the mixed layer depth and increase the sea surface temperature. These previous works, although not directly addressing changes in fluxes due to enhanced coupling frequency, clearly demonstrate the importance of the basic statistics of the air-sea fluxes for the climate system. Below, I first quantify the basic statistics of air-sea fluxes at each grid point. Then the modes of air-sea feedbacks that can lead to large-scale changes in the fluxes are studied.

The structure of this chapter is as follows: Section 3.2 quantifies the changes of mean, variance and extreme values of air-sea fluxes in the high-frequency coupling experiment, and discusses the causes of the changes, respectively. Section 3.3 identifies large-scale feedbacks between the fluxes and SST. Conclusions are given in Section 3.4.

3.2 Disentangling two different effects of coupling frequency at grid point level

3.2.1 The methods

We concentrate on three fluxes that are exchanged between ECHAM6 and MPIOM (for a detailed model description see chapter 2): the momentum flux, the net heat flux and the fresh water flux. For the momentum flux, we focus on the magnitude of wind stress $|\tau|$. The net heat flux is the sum of short- and long-wave radiation and latent and sensible heat flux. The fresh water flux is the sum of the total precipitation, evaporation and the river run-off. Downward net heat flux and fresh water flux have positive values.

The total effect induced by increasing the coupling frequency from once per

day to once per hour is quantified by the ratio of a statistical quantity S derived from hourly fluxes in experiment HC to the same statistic derived from daily fluxes in experiment DC, $S_{h,HC}/S_{d,DC}$. Here the subscript d and h indicates that S is derived form daily and hourly values respectively, and HC and DC denote experiments HC and DC, respectively. The statistical quantities (i.e. S) considered are the mean μ, the variance σ^2, and the extreme values in form of the $10th$ and $90th$ percentile q_{10} and q_{90}.

The effect described by $S_{h,HC}/S_{d,DC}$ can be decomposed into two factors. First, to quantify the effect induced by the daily averaging only, we consider the ratio of a statistic obtained from hourly fluxes in experiment HC, $S_{h,HC}$, to the same statistic derived from a daily averaging of the fluxes in the same experiment, $S_{d,HC}$, i.e. $S_{h,HC}/S_{d,HC}$. By considering hourly and daily fluxes within experiment HC, any possible changes arising from differences between experiment HC and DC (i.e. high-frequency feedbacks) are excluded from the analysis, allowing us to isolate the effect of daily averaging.

Second, changes in statistics can also arise from interactions between the atmosphere and the ocean on diurnal and intra-diurnal time scales. These interactions are accounted for in experiment HC, but are not resolved in experiment DC. For instance, consider an hourly wind stress time series containing a few strong wind bursts occurring within a time period of one day. These wind stresses can produce a stronger decrease in SSTs than the daily averaged wind stresses. Due to differences in SSTs, the hourly heat fluxes in experiment HC can behave differently from those in experiment DC. Hereafter, such interactions are referred to as high-frequency feedbacks. To quantify these feedbacks, we consider the ratio of the statistic S derived from daily averaged fluxes in experiment HC to the same statistic derived from the daily fluxes in experiment DC, $S_{d,HC}/S_{d,DC}$. Both daily fluxes have been subjected to the same averaging procedure, so that the effect of averaging is excluded. However, the daily fluxes from experiment HC contain, in an averaged sense, the effect of high-frequency feedbacks, which is absent in experiment DC. The comparison allows us to identify the daily averaged effect of high-frequency feedbacks. The total effect can be expressed as the product of the two effects:

$$\underbrace{S_{h,HC}/S_{d,DC}}_{total} = \underbrace{(S_{h,HC}/S_{d,HC})}_{averaging} \times \underbrace{(S_{d,HC}/S_{d,DC})}_{feedback} \tag{3.1}$$

In case S represents the mean, $\mu_{h,HC}$ equals $\mu_{d,HC}$. The total effect results from high-frequency feedbacks only. In case S represents variance σ^2 or percentiles q,

$S_{h,HC}$ is generally different from $S_{d,HC}$. Both the effects of averaging and that of high-frequency feedbacks may be present.

To quantify the strength and the seasonality of intra-diurnal and diurnal fluctuations, we decompose the flux F as $F = \bar{F} + F'$, where $\bar{F}$ is the daily mean and F' is the hourly anomaly. The total variance is decomposed into variances resulting from variations on intra-diurnal and diurnal scales F' and inter-diurnal time scales $\bar{F}$. Both variances can be obtained from experiment HC, whereas only the variance of $\bar{F}$ can be obtained from experiment DC. Generally, if the diurnal cycle dominates turbulent motions, the time series of F' reveals a deterministic oscillation with the period of 24 hours; otherwise the time series of F' reveals irregular intra-diurnal variations. Both types of variances can vary with the season. This seasonal dependence is quantified by considering the variances of F' in different seasons.

3.2.2 Regarding the mean

When decreasing the coupling frequency from once per hour in experiment HC to once per day in experiment DC, the long-term mean of the momentum-flux magnitude is systematically changed (Fig.3.1a). The momentum flux ratio between experiment HC and DC is larger than 1 in the Southern Ocean along the Antarctic Circumpolar Currents (ACC) and smaller than 1 over the tropical oceans, in particular over the western equatorial Pacific, and along about $40°S$. A dipole pattern exists over the Southern Ocean: the momentum-flux is increased in the ACC by up to about 10% and is decreased in the subtropical regions near $35°S - 40°S$ by about 5%. In the equatorial Pacific, the magnitude is decreased by up to 7%. The changes in the long-term mean of the net heat flux have small spatial scales and are mostly not significant (Fig.3.1b). Some significant changes in fresh water fluxes occur in the Southern Ocean, with a tendency for having reduced fluxes near $40°S - 50°S$ (Fig.3.1c). Other large changes are patchy, not well organized, and may not be of relevance.

As averaging cannot affect the mean of the fluxes, the above identified changes of the mean values have to result from intra-diurnal air-sea interactions that occur when using hourly coupling. We will come back to this issue later in section 3.3.

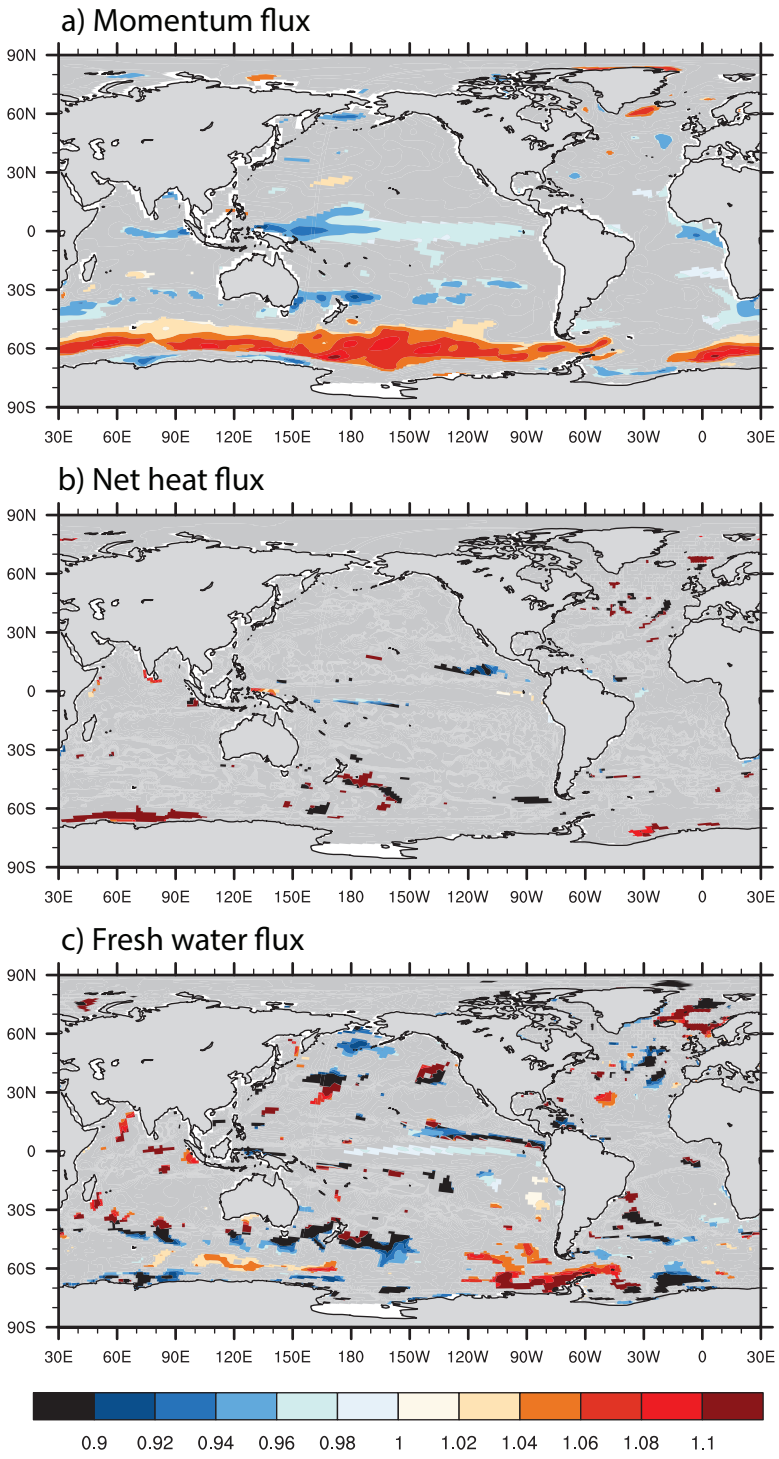

Fig. 3.1: Relative changes of time-mean air-sea fluxes $\mu_{d,HC}/\mu_{d,DC}$: a) magnitude of momentum flux, b) net heat flux, c) fresh water flux. The colours indicate no-zero differences at 5% significance level following a t-test.

3.2.3 Regarding the variance

Following Section 3.2.1, the total effect on the variance induced by increasing the coupling frequency from once per day to once per hour is quantified by the ratios of the variances of hourly fluxes in experiment HC to those of daily fluxes in experiment DC (Fig.3.2a-c). For the magnitude of the momentum flux (Fig.3.2a), hourly coupling enhances the variances up to 50% poleward of 30°. The pattern is characterized by variance ratios that reach maximum values of about 1.5 around $40°N - 50°N$ and $40°S - 60°S$. Hourly coupling decreases the total momentum variance in some parts of the tropics, in particular in the western tropical Pacific. There, the variance from experiment HC is about $20 - 30\%$ smaller than that in experiment DC.

For the net heat flux (Fig.3.2b), hourly coupling drastically increases the variance. The variance ratios are larger than 1 almost everywhere. They increase equatorward and in the tropics the heat flux variance is more than 15 times larger in experiment HC than in experiment DC.

For the fresh water flux (Fig.3.2c), the variance ratio is larger than 2 poleward of 30° with maximum values in the Southern Ocean and in the Northern Pacific and Atlantic. Over the Indian Ocean-Western Pacific warm pool and the tropical Atlantic the ratios are also larger than 1. However, in the equatorial Pacific, the variances in experiment HC are mostly smaller $(30 - 70\%)$ than those in experiment DC.

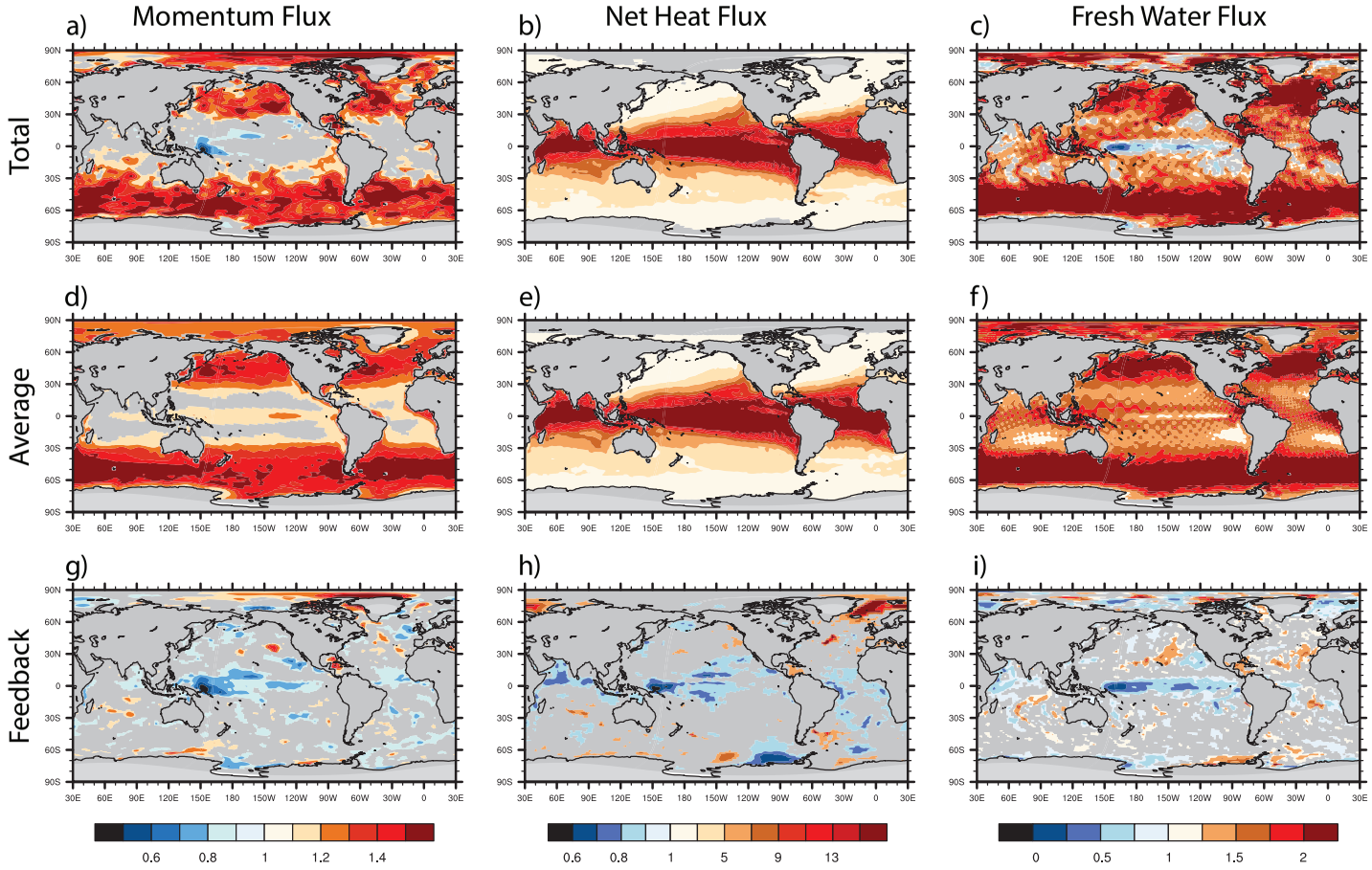

Fig. 3.2: Relative changes of the variance (expressed as variance ratios HC/DC) with respect to the total changes in a - c, to changes caused by averaging in d - f, and to changes caused by high-frequency feedbacks in g - i, for the magnitude of momentum flux (left column), the net heat flux (middle column) and the fresh water flux (right column). Colours show non-unit ratios at 5% significant level following a F-test.

The total effect induced by increasing the coupling frequency (top row in Fig.3.2) can be decomposed into the effect due to daily averaging (middle row in Fig.3.2) and the effect due to high-frequency feedbacks (bottom row in Fig.3.2). Generally, the daily averaging used in experiment DC affects all three fluxes by reducing the variances at almost all grid points (Fig.3.2 d-f), indicated by substantially higher variances in experiment HC. The spatial structures are comparable to those of the total changes (Fig.3.2 a-c). Nevertheless, important differences exist in the tropics and subtropics. There the total effect on the variance is reduced by high-frequency feedbacks, which cause the variance of the surface fluxes to reduce in experiment HC compared to experiment DC (Fig.3.2 g-i). This is particularly pronounced in the western tropical Pacific. Generally, the effect of daily averaging is clearly stronger than that of high-frequency feedbacks for momentum and fresh water fluxes in the mid- and high-latitudes and for heat flux all over the oceans. However, it is comparable to or even weaker than the effect of high-frequency feedbacks for momentum and fresh water fluxes over the tropical Pacific.

The daily averaging removes intra-diurnal fluctuations. To illustrate the significance of this reduction, the ratios of the variances of diurnal and intra-diurnal fluctuations to the total variances are examined (Fig.3.3). The variances of diurnal and intra-diurnal fluctuations are defined in section 3.2.1.

For the momentum flux, Fig.3.3a shows that intra-diurnal fluctuations amount to at least 10% of the total variance in most of the regions, and reaching about 40% over the Southern Ocean. For the net heat flux (Fig.3.3b), the intra-diurnal fluctuations become increasingly strong equatorward and reach 90% of the total variance in the tropics. At latitudes north of $60°N$ and south of $60°S$, the ratio is smaller than 60%, but still accounts for more than half of the total variance. For the fresh water flux, the ratio has the maximum in the Southern Ocean, which is larger than 60%. In the area of the Intertropical Convergence Zone (ITCZ) and in the North Pacific and North Atlantic, the ratio is around 30% or more (Fig.3.3c).

To understand how these changes come about, I consider a few time series of fluxes at grid points where large ratios are found (Fig.3.4). Compared to the momentum and fresh water fluxes, the variance of the net heat flux is particularly large because of the strong diurnal cycle of solar radiation in the tropics (Fig.3.4b). During nighttime, the hourly net heat flux is dominated by the sum of long wave radiation and sensible and latent heat flux, which are always negative

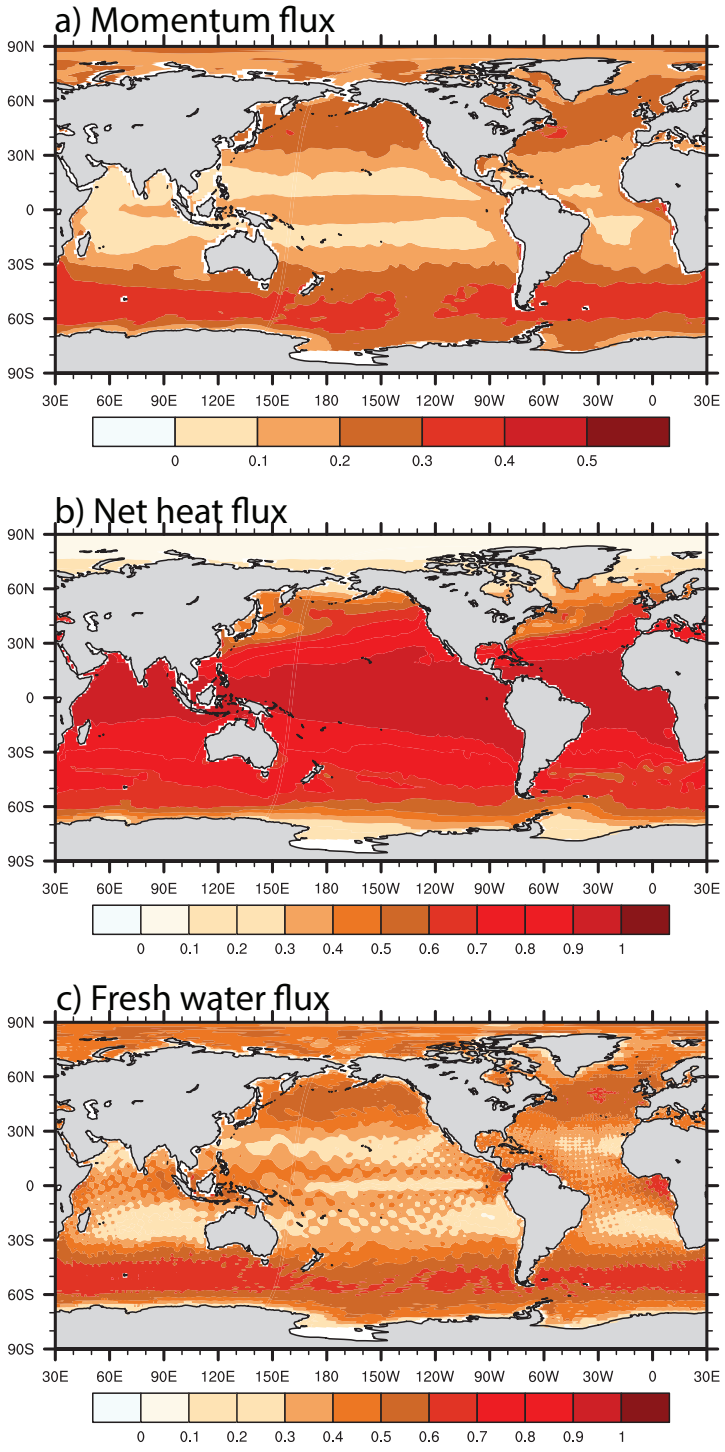

Fig. 3.3: Ratios of variance of diurnal and intra-diurnal fluctuation to the total variance of hourly fluxes of a) momentum, b) net heat, c) fresh water. Hourly fluxes of experiment HC are used. The diurnal and intra-diurnal fluctuations are obtained by subtracting daily mean from the respective hourly fluxes.

(upward). During the daytime, the net heat flux is dominated by the downward solar radiation, which can reach very large (positive) values especially in the tropics at noon. The intra-diurnal fluctuations of momentum and fresh water flux over the Southern Ocean are mainly due to high frequency turbulent motions that do not reveal regular diurnal cycles and are characterized by irregularly occurring events (Fig.3.4 a and c).

The strength of intra-diurnal fluctuations and the diurnal cycle, as described by the variance of F', varies with seasons. For the momentum flux (left column of Fig.3.5), the fluctuations are most pronounced in the winter hemisphere owing to the enhanced synoptic activities during the winter months.

For the net heat flux, the diurnal cycle dominates intra-diurnal fluctuations. As the diurnal cycle migrates with the sun, the variances of F' in the extra-tropics are much larger in the spring and summer seasons than in the fall and winter seasons (middle column in Fig.3.5). Along the equator, the diurnal and intra-diurnal fluctuations have the minimum in JJA and the maximum in SON.

For the fresh water flux, the seasonality is dominated by precipitation, whose variance is nearly 20 times larger than that of evaporation (not shown). In the tropics, large fluctuations are found within ITCZ and South Pacific convergence zone (SPCZ). At mid- and high-latitudes, precipitation varies strongly within the storm tracks during winter and fall, leading to maximal variance in these seasons.

3.2.4 Regarding the extremes

Since the daily averaging alone cannot induce changes in the mean, the changes in the time-mean fluxes have to result from high-frequency feedbacks. We expect these feedbacks to be most intense during extreme events. Following section 3.2.1, the total effect of hourly coupling on extreme values is examined by comparing the 90^{th} and 10^{th} percentile (hereafter q_{90} and q_{10}) of hourly fluxes in experiment HC with those of daily fluxes in experiment DC ($q_{10h,HC}/q_{10d,DC}$, $q_{90h,HC}/q_{90d,DC}$). For the magnitude of momentum flux, q_{10} and q_{90} indicate the extremely weak and strong fluxes, respectively. For the net heat flux and fresh water flux, q_{10} indicates the extreme large negative (upward) fluxes and q_{90} indicates the extreme large positive (downward) fluxes.

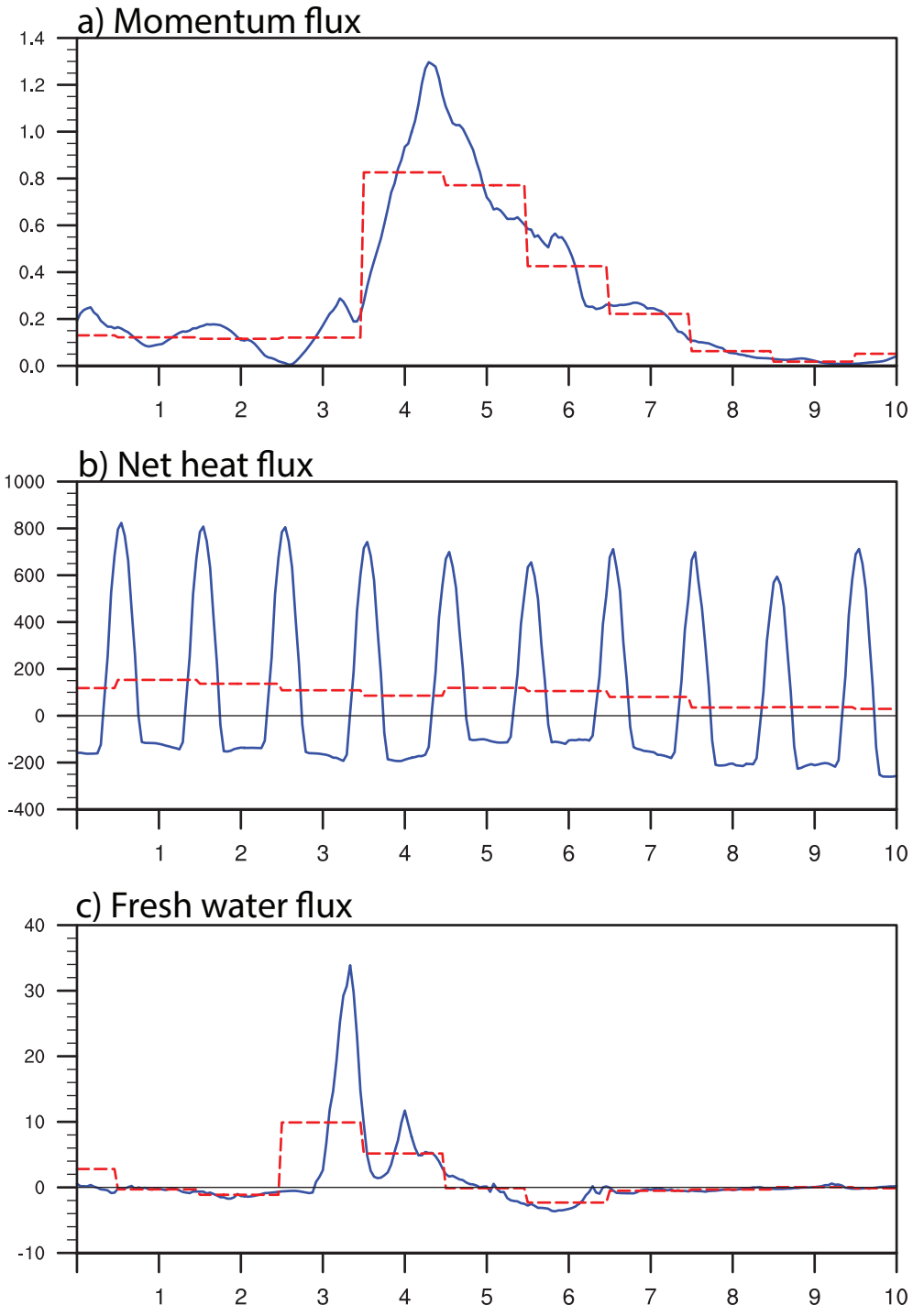

Fig. 3.4: Time series over 10 days for a) the magnitude of momentum flux at grid point $60°S$ $180°$ (Pa) , b) net heat flux at grid point $0°$ $180°$ $(W\ m^{-2})$, c) fresh water flux at grid point $60°S$ $180°$ $(mm\ d^{-1})$ in experiment HC. Dashed lines are daily series, solid lines are hourly series.

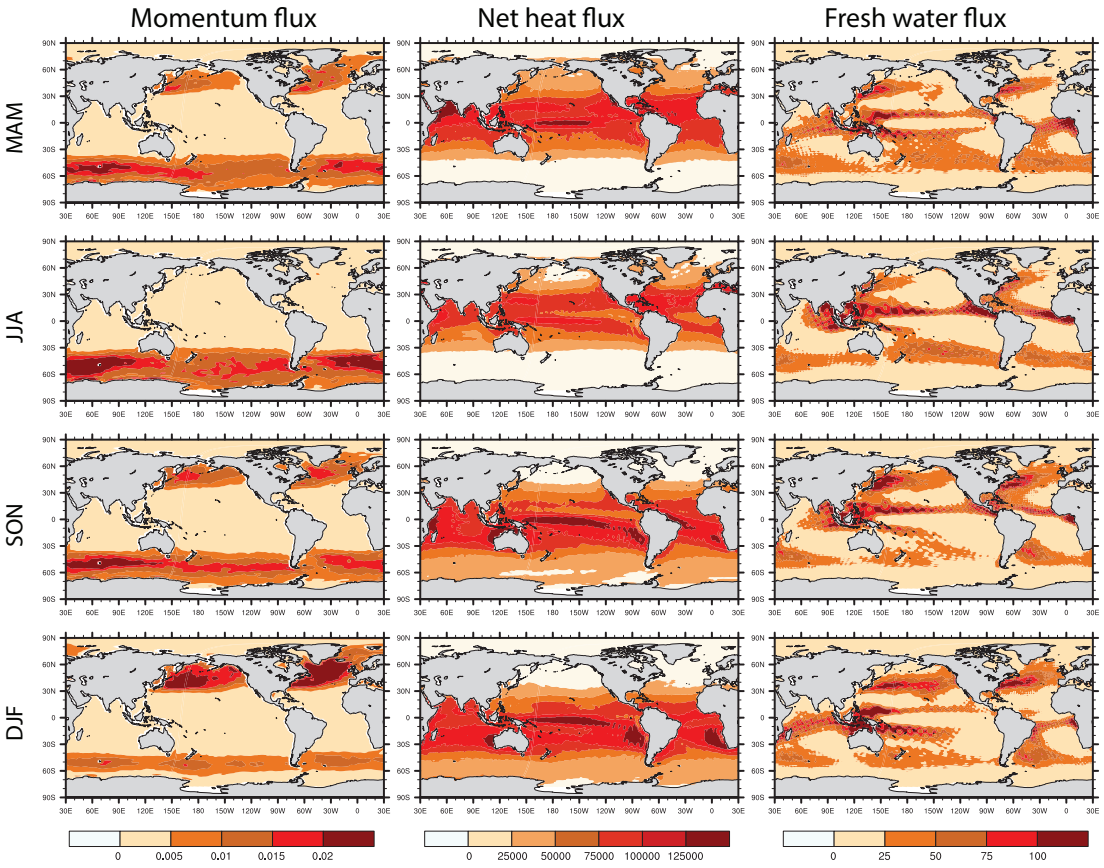

Fig. 3.5: The seasonal means of the variances of diurnal and intra-diurnal fluctuations for the magnitude of momentum flux (left column, Pa^2), the net heat flux (middle column $(Wm^{-2})^2$) and the fresh water flux (right column $(mm/day)^2$) in MAM, JJA, SON and DJF. Hourly fluxes in experiment HC are used.

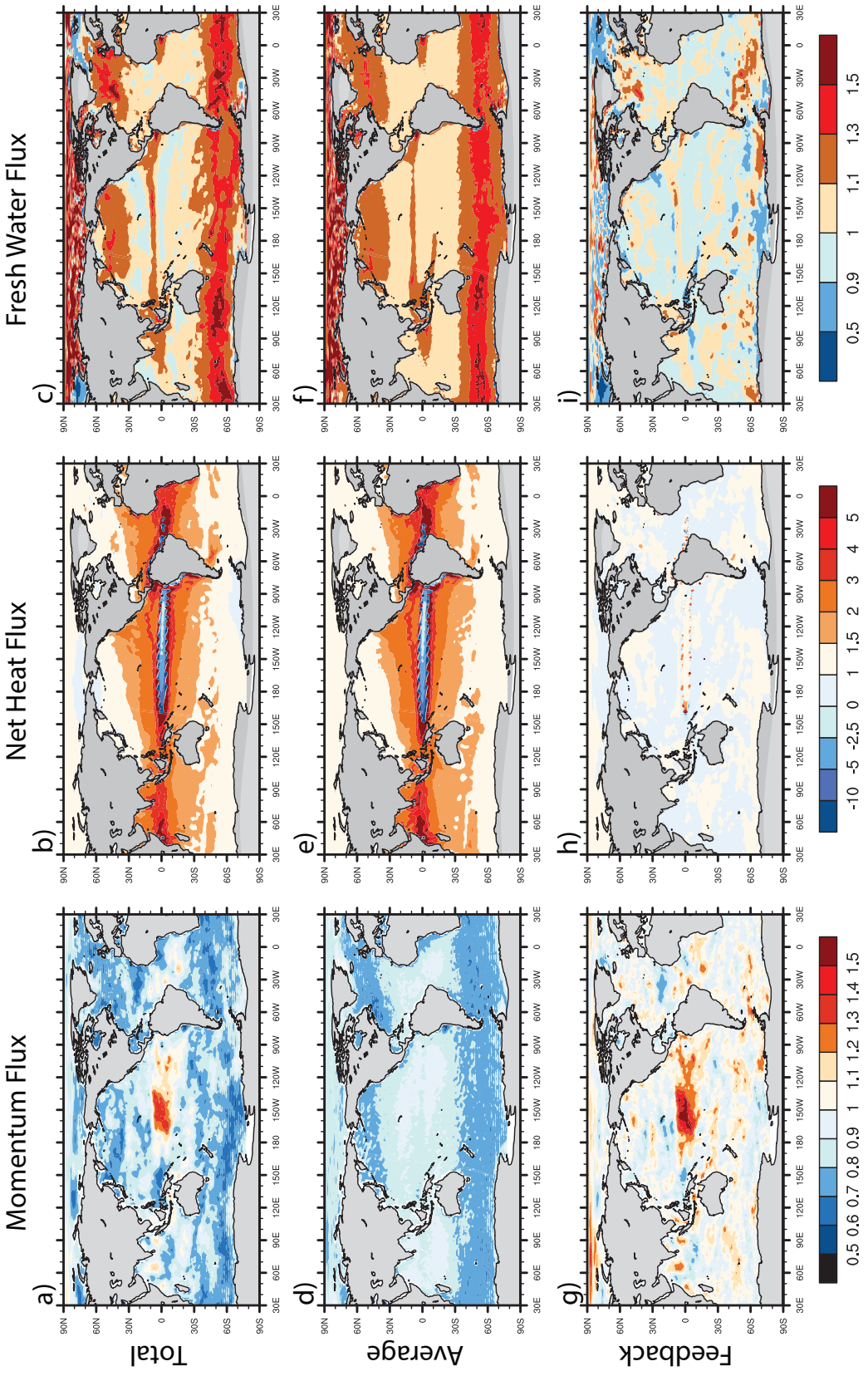

Fig. 3.6: Relative changes of the 10^{th} percentiles with respect to the total changes in a - c, changes caused by averaging in d - f and the changes caused by feedbacks in g - i. The changes are expressed as the ratio $q_{10\,HC}/q_{10\,DC}$

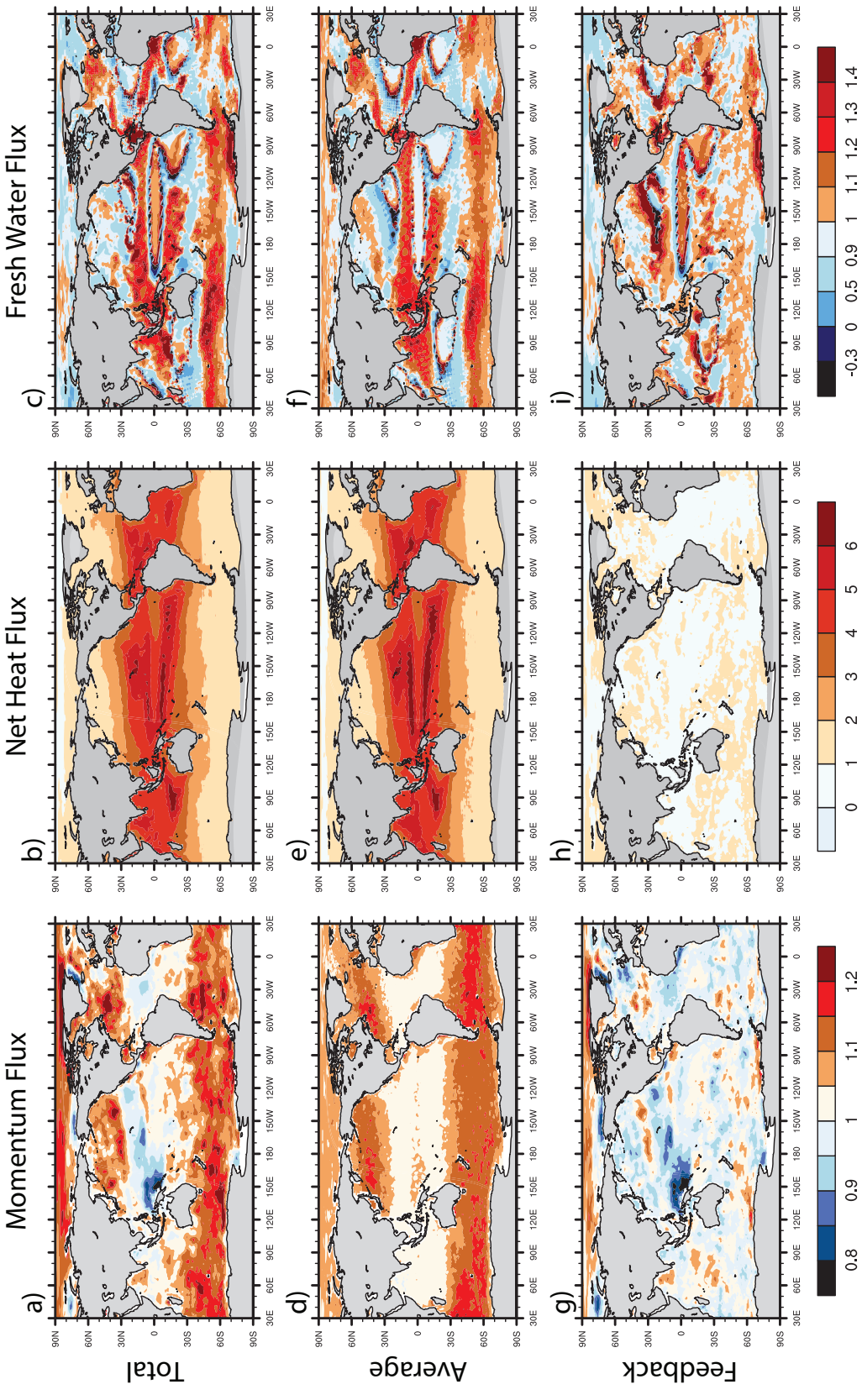

Fig. 3.7: Relative changes of the 90^{th} percentiles with respect to the total changes in a - c, changes caused by averaging in d - f and the changes caused by feedbacks in g - i. The changes are expressed as the ratio $q_{90\,HC}/q_{90\,DC}$

In most regions outside the tropics, extremely weak momentum fluxes (q_{10}) become up to 30% weaker in experiment HC than in experiment DC (Fig.3.6a), and the extremely strong momentum fluxes (90^{th} percentiles) become about 15% stronger in experiment HC than in experiment DC (Fig.3.7a). These changes suggest that increasing the coupling frequency makes the extremes occur more frequent. In the tropics, the opposite is found. Increasing the coupling frequency makes the extremes less frequent. The extremely weak momentum fluxes become less weak in the central equatorial Pacific, with the 10^{th} percentiles being up to 30% larger in experiment HC than in experiment DC (Fig.3.6a). The magnitudes of extremely strong momentum fluxes in the western tropical Pacific become less strong, with the magnitudes up to 15% smaller in experiment HC than those in experiment DC (Fig.3.7a).

For the net heat flux (Fig.3.6b,3.7b), the diurnal cycle dominates the intra-diurnal fluctuations. Including the diurnal cycle increases the extreme downward (as characterized by q_{90}) and extreme upward (as characterized by q_{10}) net heat flux cases remarkably. The ratios for both q_{90} and q_{10} are larger than one almost everywhere, reaching a factor of 5 for extreme downward fluxes in some tropical areas. In the equatorial Pacific, q_{10} is negative (indicating upward flux) in experiment HC. However, in experiment DC, averaging out the diurnal cycle strongly reduces the probability of having upward fluxes so that q_{10} is positive (indicating downward flux) (not shown). As a result, the ratio for q_{10} is negative there (Fig.3.6b).

Fresh water flux results mainly from intermittent precipitation events and continuous evaporation. Increasing the coupling frequency leads to increases in q_{10} in the Southern Ocean and in the North Pacific and North Atlantic as well as partly in the equatorial Pacific (Fig.3.6c). This indicates increases in the extremes of negative (upward) fluxes related to strong evaporation there, with maximum increase reaching about 50%. The increase in evaporation results likely from larger wind stress magnitudes in experiment HC than in experiment DC. Increasing the coupling frequency increases also q_{90} in the storm track regions over the Southern Ocean and in the ITCZ and SPCZ, indicating stronger precipitation in these regions (Fig.3.7c). The maximum increase in precipitation reaches about 40%. In the North Pacific and North Atlantic, increasing the coupling frequency enhances mostly precipitation in the southern flanks of the storm tracks. In the central equatorial Pacific, where evaporation dominates precipitation, q_{90} of fresh water flux is negative (not shown), corresponding to weak precipitation

there. Increasing the coupling frequency increases evaporation, enhancing the ratio $q_{90,h,HC}/q_{90,d,DC}$ (Fig.3.7c). A notable decrease in precipitation is found around $30°S$ and $30°N$, where precipitation is generally weak.

The effects from daily averaging and high-frequency feedbacks are compared (Fig.3.6d-f versus Fig.3.6g-i, Fig.3.7d-f versus Fig.3.7g-i). The total effect of increasing the coupling frequency results mainly from the daily averaging (Fig.3.6d-f and Fig.3.7d-f) as their spatial structures and magnitudes are comparable to those related to the total changes (Fig.3.6a-c and Fig.3.7a-c). Exceptions are found for the wind stress magnitude in the tropics where high-frequency feedbacks act to reduce the extremes (Fig.3.6g and Fig.3.7g). High-frequency feedbacks have also an impact on extremes of daily precipitation events (Fig.3.7i). In particular,the area of the dry regions in the subtropical North Pacific and subtropical North Atlantic are reduced when increasing the coupling frequency. Near the northern boundaries of these dry regions, q_{90}, which is mostly negative, has larger magnitudes in experiment HC than in DC. Consequently, $q_{90,d,HC}/q_{90,d,DC}$ are larger than one. In the central equatorial Pacific, where q_{90} is negative, high-frequency feedbacks enhance evaporation. As shown in Fig.3.6h and Fig.3.7h, high-frequency feedbacks have little effect on the net heat flux, which is dominated by a strong diurnal cycle.

3.2.5 A comparison with observation

The above analysis shows that for the heat flux, daily averaging reduces variances by a factor of 15 and extremes (in form of q_{10} and q_{90}) by a factor of 5. To confirm that the strong variations and the large extremes of the net heat flux in experiment HC exist in the real world, we consider the hourly net heat flux at 11 moorings available from the TAO project (Tropical Atmosphere Ocean project). For the comparison, hourly heat flux located at 11 grid points close to the moorings are selected from experiments HC.

The comparison of the hourly time series of net heat flux in experiment HC and observation shows that the hourly coupled MPI-ESM simulates the diurnal cycle very well, with maximum values close to $800 Wm^{-2}$ at noon and minimum around $-150 Wm^{-2}$ in the nighttime (not shown). Because of a realistic simulation of the diurnal cycle of the net heat flux in experiment HC, the biases of the considered statistics are strongly decreased when increasing the coupling frequency from once per day to once per hour.

To evaluate the bias of the considered statistics, I define the relative bias in ex-

periment HC and DC as ($|S_{h,HC}-S_{h,OBS}|/|S_{h,OBS}|$) and ($|S_{d,DC}-S_{h,OBS}|/|S_{h,OBS}|$), respectively. $S_{h,HC}$, $S_{d,DC}$ and S_{OBS} indicate the statistical quantities on each grid point in experiment HC, DC, and the observations. The mean of the relative biases at the considered 11 grid points are taken as the mean relative bias. In experiment HC, the mean relative bias of the variance, skewness, q_{10} and q_{90} are very small, with values of 0.110, 0.093, 0.194 and 0.069, respectively. In experiment DC, however, the mean relative bias are substantially larger, with values up to 0.963, 1.533, 1.084 and 0.764, respectively.

3.3 Large scale feedbacks related to changes in surface fluxes

The analysis in Section 3.2 focuses on changes in air-sea fluxes at each grid point. One important feature is the change in the mean magnitude of the wind stress (shown in Fig.3.1), which is characterized by a decrease of wind stress magnitude over the equatorial Pacific and a dipole pattern of wind stress over the Southern Ocean. These large scale changes may result from interactions between large-scale feedback modes between SST and wind stresses, which will be analysed below.

3.3.1 The methods

To understand large scale feedbacks in the Southern Ocean and equatorial Pacific, we consider anomalies of zonal mean SST and zonal mean zonal wind stress in the Southern Ocean ($20°S - 80°S$) in the equatorial Pacific ($10°S - 10°N$, $120°W - 90°W$). The dominant SST-modes are identified as the leading EOF obtained by performing an EOF analysis on SST anomalies of experiment HC. The anomalies are obtained by subtracting the monthly climatological values from the respective hourly time series.

To identify modes of wind stress, which emerge when dominant SST-modes are strong, I project SST anomalies in experiment HC and those in experiment DC onto the same dominant SST-mode obtained by performing EOF analysis on SST anomalies in experiment HC to produce the amplitude time series. Using the resulting time series, we then calculate the composites of wind stress anomalies in the respective experiments. The wind stress composites related to the positive phase of SST-modes are obtained when the time series of SST-modes are larger than one standard deviation; the wind stress composites related to the negative

phase of the SST-modes are obtained when the time series of the SST-modes are smaller than minus one standard deviation. The analysis is done for both the region in the Southern Ocean and the region in the equatorial Pacific

3.3.2 Southern Ocean

The dominant SST mode in the Southern Ocean, as expressed in form of the first EOF of zonal mean SST in experiment HC (Fig.3.8) shows a dipole with colder SST at the latitudes between $50°S - 70°S$ and warmer SST between $50°S - 35°S$. The composites of zonal wind stress related to the positive and negative phase of the SST mode are shown by black solid and dashed lines in Fig.3.9a, respectively. The structure of the composites suggests that warmer SSTs are related to weaker wind stress and colder SSTs are related to stronger wind stress. The relation is consistent with the idea that stronger winds lead to larger sensible and latent heat fluxes and stronger mixing which tend to generate colder SST, a known feature characteristic for large-scale air-sea interactions. The SST mode in turn, in particular the SST anomalies over $50°S - 60°S$ further strengthen the existing climatological mean temperature gradient there, leading to a further strengthening of wind stress at these latitudes. This interaction will be referred to as the SST-wind-stress feedback hereafter.

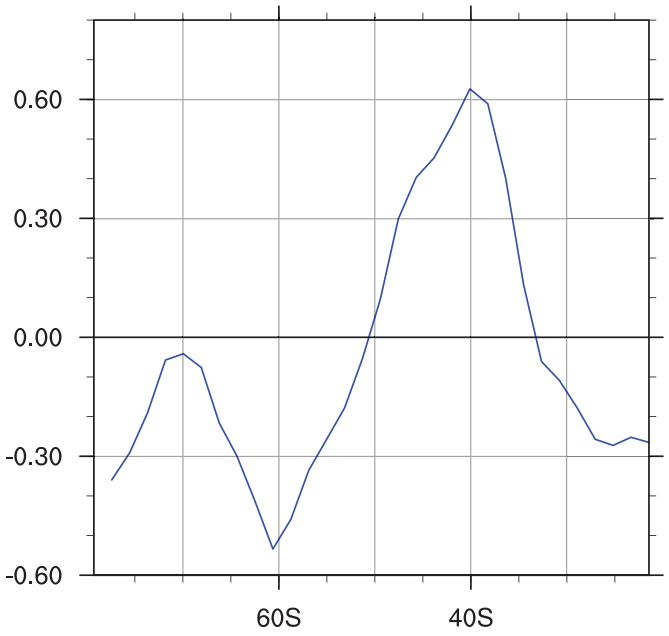

Fig. 3.8: EOF1 of zonal mean of SST anomalies (K) in latitudes of $20°S - 80°S$.

To quantify to which extent this feedback exists in experiment DC, composites of wind stress anomalies in experiment DC that are related to the SST-mode in Fig.3.8 are derived. The black solid (dashed) line in Fig.3.9b shows the positive (negative) phase of the composite. The general result that warmer SSTs are related to weaker wind stresses and colder SSTs are related to stronger wind stresses is also found in experiment DC.

The main difference between experiment HC and experiment DC lies in the net effect described by the sum of the positive and negative composites (green lines in Fig.3.9a,b). The net effects in experiments DC and HC are, by and large, out of phase. The difference of the two green lines (Fig.3.9c), which shows the effect of the coupling frequency on the wind stress related to the SST mode, suggests that it is the change of the wind stress associated with the SST mode that produces the dipole structure in the momentum flux in Fig.3.1.

To understand why in the Southern Ocean the wind stress in relation to the SST mode behaves differently in experiment DC than in experiment HC, we decompose the composites of zonal wind stress into different seasons. We find that Figs.3.9a and b result mainly from the composites in MAM and DJF. In SON and JJA, the wind stress anomalies related to the SST-mode are negligible (not shown). In experiment HC, the composites related to the positive and negative phase of the SST-mode are in-phase in MAM (red lines Fig.3.9d). This in-phase relation leads to a re-enhancement of the net effect. In DJF, the composites related to the positive and negative phase of the SST-mode are out-of-phase, leading to a cancellation of the net effect. Because of the re-enhancement in MAM, the net wind stress related to the SST mode, as characterized by the sum of the positive and negative composites, reveals a strengthening of wind stress at latitude $50°S - 70°S$ and a weakening at latitude north of $50°S$. In experiment DC, because the positive and negative composite patterns are out-of-phase in both DJF and MAM, the net wind stress related to the SST-mode does not favour a strengthening of wind stress south of $50°S$ and a weakening north of $50°S$.

The described difference between experiment DC and experiment HC can be related to the seasonality in SST. The maximal magnitude of the dominant SST-mode (Fig.3.8) is about $0.6°C$. In a cold season when high-latitude SSTs are close to the freezing point, the dominant SST-mode could be much less efficient in supporting any SST-wind-stress feedback. The SST in the Southern Ocean is colder in experiment HC than in experiment DC. In the warmest seasons, namely

the DJF in both experiments DC and HC and the MAM in experiment DC, the wind stress related to the SST mode displays a dipole structure with stronger wind stress being associated with colder SST and weaker wind stress being associated with warmer SST. The relation is not found for colder seasons. In MAM in experiment HC, which is colder than MAM in experiment DC, the stronger wind stress is associated with warmer SST and the weaker wind stress is associated with colder SST. In the coldest seasons, namely the SON and the JJA in both experiments HC and DC, no significant wind stress anomalies related to the SST-mode are found. This dependence on the seasonality of SST might be responsible for the differences in the SST-wind-stress feedback between experiment HC and *DC*, and thus for the increase in the wind stress in the Southern Ocean when the coupling frequency is increased (Fig.3.9c and Fig.3.1a).

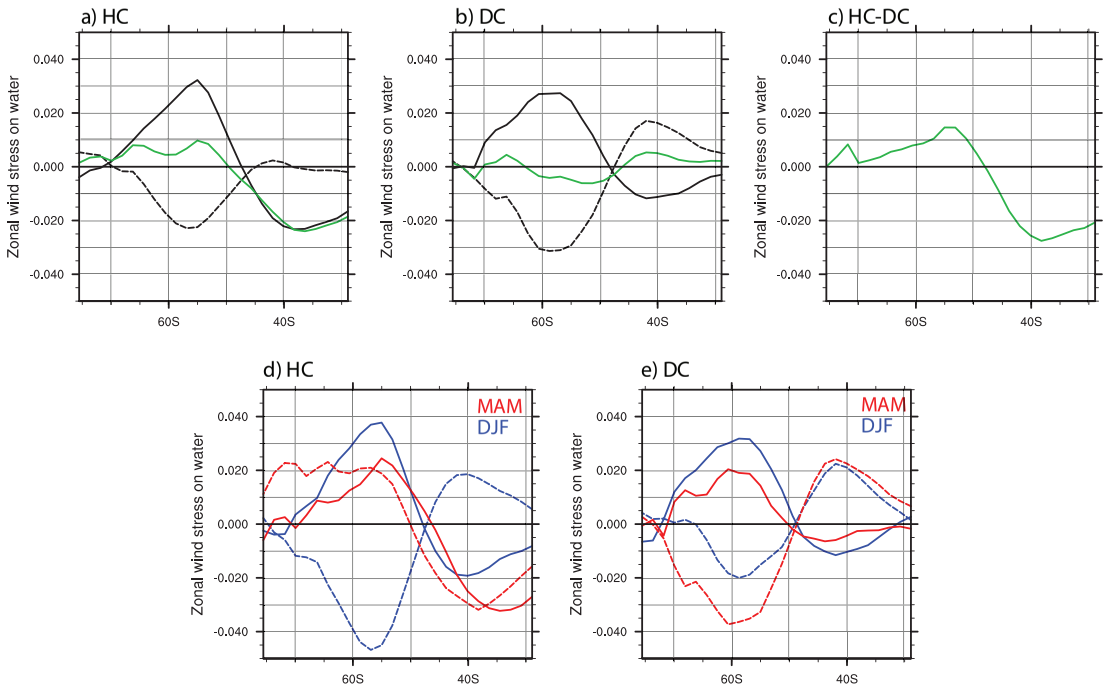

Fig. 3.9: Composites of zonal-mean zonal wind stress (Pa) a) based on time series obtained by projecting hourly SST anomalies in experiment HC on EOF1 in Fig.3.8, b) based on time series obtained by projecting daily SST anomalies in experiment DC on EOF1 in Fig.3.8.d) based on time series obtained by projecting hourly SST anomalies in MAM (red) and DJF (blue) in experiment HC on EOF1 in Fig.3.8. e) based on the time series obtained by projecting daily SST anomalies in MAM (red) and DJF (blue) in experiment DC on EOF1 in Fig.3.8. Solid (dashed) lines are the composite related to the positive (negative) SSTa pattern in Fig.3.8, green lines are the net effect. c) shows the difference of the net effect in experiment HC and DC.

3.3.3 Equatorial Pacific

The systematic decrease in wind stress magnitude along the equatorial Pacific (Fig.3.1a), which is mainly caused by the change of the zonal wind stress, might be related to ENSO. To understand such a feedback, we diagnose the dominant mode of tropical SSTs and quantify the large-scale structures in zonal wind stress that occur when the dominant SST-mode is strong in both experiments as outlined in section 3.2.1. For this purpose, we perform an EOF analysis on the SST anomaly in the tropical Pacific ($10°S - 10°N$, $120°W - 90°W$) in experiment HC. The dominant SST-mode shows an ENSO event (not shown), characterized by the warmer SSTs in the central and eastern Pacific and the colder SSTs in the western tropical Pacific.

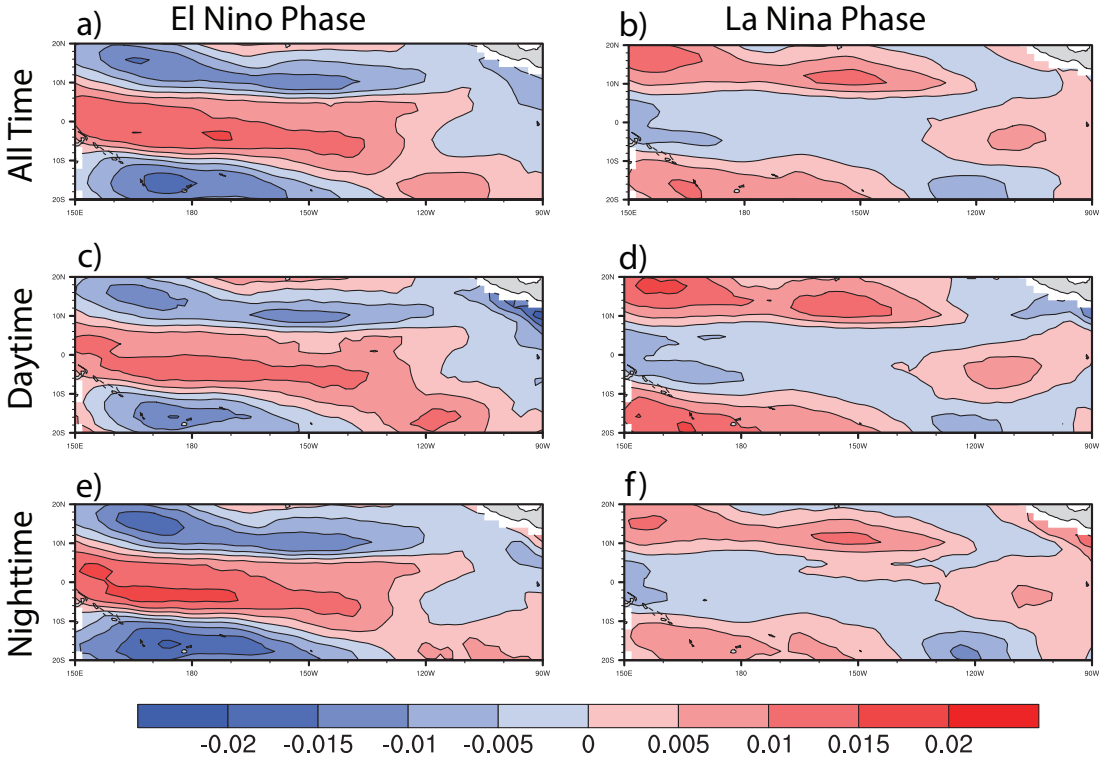

Fig. 3.10: Composites of zonal wind stress anomalies (Pa) in experiment HC for the El Niño phase (a) and La Niña phase (b). Both phases are further decomposed by composing wind stress anomalies at day (c and d) and night (e and f) time.

The wind stress anomaly related to the El Niño phase is described by the composite (Fig.3.10a) obtained when the magnitude time series, i.e. PC1, is larger than one standard deviation, and that related to the La Niña phase is described by the composite (Fig.3.10b) obtained when PC1 is smaller than minus

one standard deviation. The composites suggest that a strong El Niño phase is connected to a stronger westerly anomaly along the equator. This is consistent with the Bjerknes feedback (Bjerknes 1969) that warmer SST anomalies in the central and eastern Pacific that lead to a decreased zonal SST gradient, resulting in weaker easterly wind stresses, which in turn further amplify the warming in the central and eastern Pacific.

Fig.3.10a-b show that the zonal wind stress anomalies during the El Niño phase are much larger than those during a La Niña phase. As a result, the net effect (El Niño phase + La Niña phase) shows a stronger westerly anomaly, i.e. a decrease in the easterly wind stress along the equatorial Pacific (Fig.3.11a). To understand why the wind stress does not have the same magnitude during El Niño and La Niña events in experiment HC, we decompose the composites in Fig.3.10a and b into daytime and nighttime. Daytime (nighttime) is defined as the time at which solar radiation is larger (smaller) than $50W/m^2$. We find that zonal wind stress anomalies appear to be stronger in the nighttime (Fig.3.10e) than in the daytime (Fig.3.10c) during an El Niño phase, whereas they present comparable amplitudes in both daytime and nighttime during a La Niña phase (Fig.3.10d,f). Therefore, the Bjerknes feedback reveals a diurnal cycle during El Niño events, with the feedback being stronger in the nighttime than in the daytime, and no clear diurnal cycle during La Niña events. This diurnal cycle of Bjerknes feedbacks during El Niño events leads to the net effect in experiment HC shown in Fig.3.11a.

In experiment DC, the diurnal cycle of the Bjerknes feedback cannot be reproduced since fluxes are exchanged on a daily basis, so the composites during El Niño and La Niña have comparable magnitudes (not shown) making the net effect in experiment DC weaker than that in experiment HC (Fig.3.11b). The difference of the net wind stress in the two experiments (Fig.3.11c) shows stronger westerly anomalies of the zonal wind stress along the equator in experiment HC than in experiment DC. As the climate state of the zonal wind stress along the equator is easterly, the westerly anomaly of zonal wind stress indicates a decrease of the easterly wind stress. Hence, it is the diurnal cycle of the Bjerknes feedback during El Niño events that decreases the magnitude of wind stress in the equatorial Pacific in Fig.3.1a.

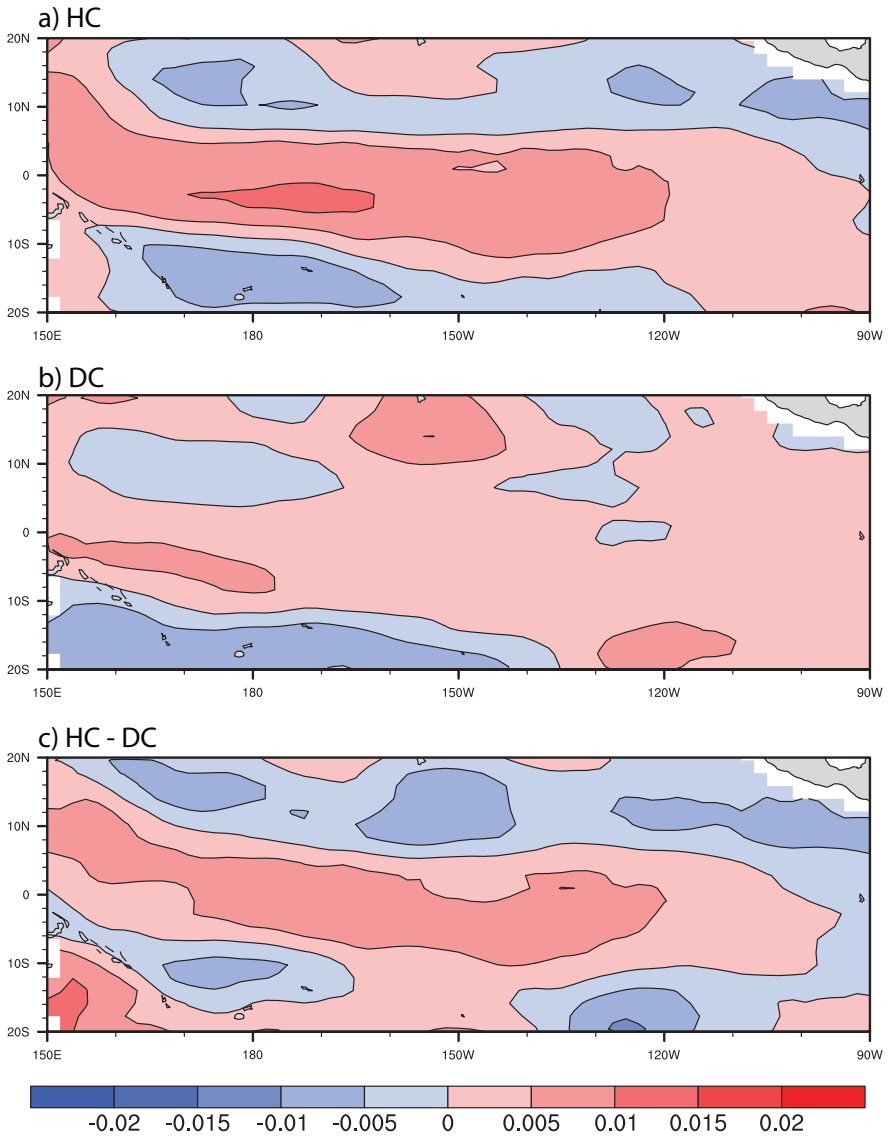

Fig. 3.11: The sum of zonal wind stress (Pa) composites related to the El Niño and La Niña phase for a) HC, b) DC. c) shows the difference HC-DC.

3.4 Conclusions

Using hourly coupling instead of daily coupling in MPI-ESM leads to changes in the statistics of air-sea fluxes. The changes can be separated into two different effects: one results from the daily averaging and the other from the high frequency feedbacks. With respect to the mean, significant changes are found for the magnitude of momentum flux, with an increase of up to 10% over the Southern Ocean and a decrease of up to 7% in the equatorial Pacific. These changes have to be attributed to feedbacks.

Hourly coupling increases the variances by up to 50% for the magnitude of momentum flux, up to 100% for the fresh water flux and up to 15 times for the net heat flux. These increases are mainly due to the daily averaging which removes a considerable amount of the variance that is related to high-frequency turbulent fluctuations in the momentum flux and the fresh water flux in the mid- and high-latitude regions and to the diurnal cycle of the net heat flux. Exceptions are found in the tropics, where feedbacks reduce the variances, most significantly those of the momentum and fresh water flux. The diurnal and intra-diurnal variations resolved in experiment HC vary in their strengths with seasons and amount up to 50% to 90% of the respective total variances.

Extremes are generally reduced by daily coupling, as the daily averaging smooths out the extremes. The reduction in the 10^{th} and 90^{th} percentiles reaches between 10 and 20% for momentum fluxes, about 40% for fresh water fluxes, and about a factor of 5 for the net heat flux. Exceptions are found in the tropics, in particular over the equatorial Pacific, where the weak momentum fluxes over the central equatorial Pacific are strengthened, the strong momentum fluxes over the western equatorial Pacific are weakened, and the weak evaporations over central equatorial Pacific are enhanced. These extremes seem to be related to positive feedbacks between high-frequency extremes and SST.

By separating the total changes between experiment HC and experiment DC into those induced only by the daily averaging and those induced by feedbacks, I find that the daily averaging has a strong effect on variations and extremes, in particular for the net heat flux globally and for the momentum and fresh water fluxes in the mid- and high-latitudes. High frequency feedbacks are important for the mean momentum fluxes both over the equatorial Pacific and over the Southern Ocean and for the variances and extremes of momentum and fresh water fluxes in the tropical Pacific.

In the Southern Ocean, the SST-wind-stress feedback, characterized by weak-

er/stronger wind stress anomalies over warmer/colder SST and the re-enforcement of anomalies related to changes in temperature gradients, is different in experiment HC and experiment DC. The difference seems to arise from the background SST, with the SST-wind-stress feedback being only found when the background SST is sufficiently warm. Because SST is colder in experiment HC, the SST-wind-stress feedback is modified. This modification results in the increase of the magnitude of wind stress over the Southern Ocean.

In the equatorial Pacific, the decrease of the magnitude of the wind stress is related to the diurnal cycle of Bjerknes feedback which cannot be simulated by experiment DC. In experiment HC, the Bjerknes feedback has a diurnal cycle during El Niño events with enhanced westerly anomalies in the nighttime but weaker ones at daytime. In La Niña events, there is no clear diurnal cycle. This leads to westerly anomalies on average along the equator in experiment HC. As the climate mean wind stress in the equatorial Pacific is easterly, the magnitude of the wind stress is weaker in experiment HC than in experiment DC.

Besides the influence on the magnitude of wind stress in the equatorial Pacific, the diurnal cycle of Bjerknes feedback in the equatorial Pacific might also be related to the simulation of ENSO in experiment HC, and the change of the mean SST in the tropical Pacific. To understand why the Bjerknes feedback exhibits a diurnal cycle and how this diurnal cycle affects the mean SST requires additional work.

Chapter 4

Impact of intra-daily air-sea interactions on ENSO asymmetry

The dominant mode of inter-annual variability in the tropical Pacific is El Niño-Southern Oscillation (ENSO). ENSO is not symmetric in the sense that El Niño is stronger than La Niña. However, many CMIP5 models, including MPI-ESM, produce an almost symmetric ENSO. This chapter shows that, if resolving the intra-daily air-sea interactions by coupling the atmospheric and oceanic model components once per hour, the ENSO asymmetry can be reproduced by MPI-ESM.

It is found that the diurnal cycle of SST in hourly coupled MPI-ESM enhances the atmospheric convection in the central tropical Pacific during El Niño years but does not affect it in La Nina years, since the background SST in the central tropical Pacific are only warm enough to support convection in the nighttime during El Niño events. As a result, the anomalies of Walker circulation, which are directly related to the convection are stronger during El Niño years than that during La Niña years, making El Niño to be stronger than La Niña. The results are obtained with the CMIP5 version of MPI-ESM at a low resolution and are further confirmed by the latest version of MPI-ESM at higher spatial resolutions, implying that the role of the intra-daily air-sea interactions in the ENSO asymmetry is independent of model resolutions.

4.1 Introduction

The amplitude of SST anomalies is generally stronger during El Niño than during La Niña. This difference is referred to as ENSO asymmetry (Hoerling et al. 1997; Burgers and Stephenson 1999). Besides the difference of the SST anomalies, the asymmetry also has a vertical structure in the ocean. In the western Pacific, the negative anomalies of the upper ocean heat content during a strong El Niño are much stronger than the corresponding positive anomalies during a strong La Niña (Tang and Hsieh 2003).

Since CGCMs are usually unable to simulate the ENSO asymmetry (Zhang et al. 2009), the causes of the ENSO asymmetry have been studied by many previous works. For example, some studies suggest that stronger El Niño events are related to a stronger warming tendency due to nonlinear dynamic thermal advections, which ultimately generates the ENSO asymmetry (Timmermann et al. 2003; An and Jin 2004; An et al. 2005). Other suggest that the ENSO asymmetry results from the fact that effects of the tropical instability waves are different during El Niño and La Niña years. It is shown that the tropical instability waves tend to reduce the cold-tongue intensity. This effects are stronger during La Niña than during El Niño (Yu and Liu 2003; Vialard et al. 2001; An et al. 2008).

Though these previous studies show that processes in the ocean are important for the ENSO asymmetry, it is difficult to separate the effects of atmosphere and ocean in a coupled air-sea system. Especially in the tropics, air-sea interactions are of significance because they play an important role for ENSO and ENSO asymmetry (Guilyardi et al. 2004; Watanabe et al. 2011; Kang and Kug 2002; Zhang et al. 2009; Hoerling et al. 1997; Zhang and Sun 2014). Kang and Kug (2002) show that the ENSO asymmetry is related to the westward shift of wind stress anomalies. The shift of wind stress is a consequence of the deep convection (Zhang et al. 2009): During El Niño, the convection anomalies are located over the central and eastern tropical Pacific, whereas, during La Niña, the convection anomalies are confined to the western central Pacific. This shift of convection anomalies is attributed to the dependence of convection on the background SST (Hoerling et al. 1997). This role of SST-dependent convection in ENSO asymmetry is further confirmed in a more recent study by Zhang and Sun (2014) using wind-forced GCM experiments.

Even though the effects of air-sea interactions on ENSO asymmetry have been considered, but not on an intra-daily time scales. Previous works are generally based on monthly mean variables of observations or model output, with the role

of diurnal cycle of SST and the related intra-daily air-sea interactions being not addressed.

Recently, the diurnal cycle of SST has been extensively studied using both observations (Gille 2012; Clayson and Bogdanoff 2013; Weller et al. 2014; Yang et al. 2015) and models (Danabasoglu et al. 2006; Bernie et al. 2008; Terray et al. 2012; Masson et al. 2012; Li et al. 2013; Thushara and Vinayachandran 2014). It is found that, in the tropics, the annual mean of diurnal range of SST can be as large as $0.5°C$ (Kennedy et al. 2007), with maximum values up to $3°C$ (Clayson and Bogdanoff 2013). Meehl et al. (2001) suggest that processes on shorter time and smaller space scales may influence processes with longer and larger scales in continuous scale interactions. The intra-daily air-sea interactions are important high-frequency processes in the coupled air-sea system, which might affect processes with time scales longer than one day, such as ENSO. For example, when the intra-daily variability of SST is included, the model's El Niño has a more realistic evolution in its developing and decaying phases, a stronger amplitude and a shift towards lower frequencies (Terray et al. 2012). The ENSO asymmetry is also influenced by air-sea interactions with time scales shorter than one day.

As shown in Masson et al. (2012), the simulation of ENSO asymmetry is improved if increasing the air-sea coupling frequency from daily to hourly. However, in their study, 1m-depth surface layer for the ocean model is necessary to simulate the ENSO asymmetry. Moreover, the processes by which the intra-daily air-sea interactions affect the ENSO asymmetry were not studied. Therefore, this chapter aims to reveal the responsible mechanisms by which the intra-daily air-sea interactions affect the simulation of ENSO asymmetry with the low resolution version of the Max Planck Institute Earth System Model (MPI-ESM). Since it is not known whether the influence of high coupling frequency on the ENSO asymmetry depends on the applied model or model resolution, the analyses are further extended to simulations performed with the latest version of the model at higher resolutions.

This chapter is organized as follows. In section 4.2, the methods and observations used in the analysis are introduced. The model performance in reproducing the intra-daily air-sea interactions is evaluated. Section 4.3 describes the ENSO asymmetry in observations, and in a daily- and a hourly- coupled experiment. A mechanism of how the intra-daily air-sea feedback influences the ENSO asymmetry is proposed. Conclusions are given in section 4.4.

4.2 Data, methods and simulated diurnal cycles

4.2.1 Data and methods

To quantify the asymmetry of ENSO, this work composes the SST anomaly in the tropical Pacific ($30°S - 30°N$, $100°E - 60°W$) based on 50-years monthly Niño-3 index derived from the Hadley Centre Sea Ice and SST (HadISST) dataset (Rayner et al. 2003) and from experiment HC and DC (Fig.4.1).

The composite related to the El Niño phase is obtained when the Niño-3 index is larger than $0.5°C$ (dashed lines above zero); the composite related to the La Niña phase is obtained when the Niño3 index is smaller than $-0.5°C$ (dashed lines below zero). The sum of the composites of El Niño and La Niña phases is used to measure the ENSO asymmetry. To understand the air-sea feedback processes that affect the ENSO asymmetry, this work also composes anomalies of mixed-layer depth, upper ocean potential temperature, zonal wind stress and outgoing longwave radiation (OLR) in the same way as for the SST anomalies. The OLR considered is the full sky OLR minus the clear sky OLR, hence represents only the effect of convection. Anomalies of mixed-layer depth, upper ocean potential temperature, zonal wind stress and OLR are obtained by subtracting the monthly climatological values from the respective Niño3 index in experiment HC and DC.

To study the diurnal cycle of air-sea feedback, 50-years hourly OLR and SST in experiment HC are used. The composites of OLR and SST anomalies in El Niño and La Niña phases are decomposed into daytime and nighttime. Here the daytime is defined as the time when solar radiation is positive and the remaining time is defined as nighttime.

The simulated climatological SST is compared with that obtained from Hadley Centre Sea Ice and SST (HadISST) dataset (Rayner et al. 2003). 7 years (2007-2014) hourly SSTs of TAO/TRITON data of a mooring close to (0°, 140°W) (http://www.pmel .noaa.gov/tao/) are used to validate the diurnal cycle of the simulated SST.

4.2.2 Diurnal cycles in hourly coupled MPI-ESM

In reality, the atmosphere is directly influenced by the skin temperature of the ocean. However, in the ocean component of MPI-ESM, i.e. MPIOM, the SST, which is the model skin temperature, is the temperature of the first model layer. As this layer is 12 meters deep in MPIOM and can store much more heat than a

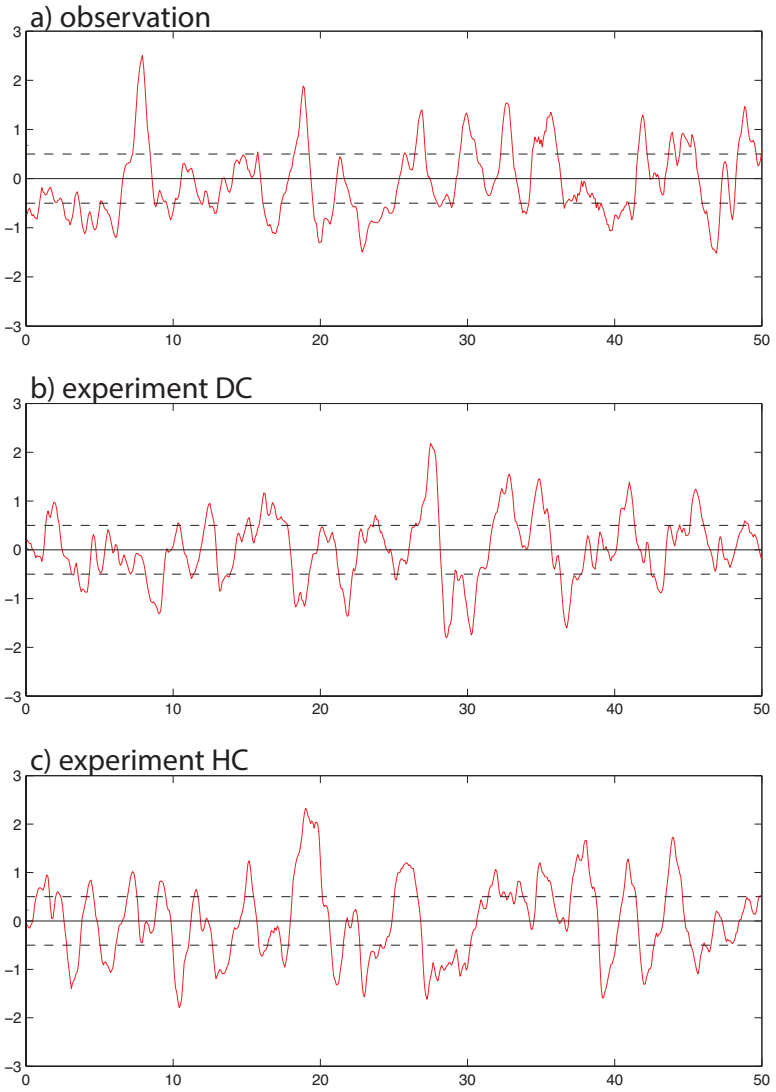

Fig. 4.1: Red lines are the monthly time series of Niño-3 index in (a) observation, (b) experiment DC and (c) experiment HC. Black dashed lines denote $0.5°C$ and $-0.5°C$.

thinner surface layer, the diurnal cycle of SST in the model is generally weaker than that in observation. Nevertheless, as shown in Fig.4.2b, MPI-ESM produce strong diurnal cycles of SST with the mean diurnal range being larger than $0.15°C - 0.2°C$ along the equator. Strong diurnal cycle are also found in net heat flux with the mean diurnal range being larger than 840 $W\ m^{-2}$ in the equatorial Pacific, the north Indian Ocean and the tropical Atlantic (Fig.4.2a).

The interactions between the diurnal cycle of the atmospheric and the oceanic variables are the intra-daily air-sea interactions. To have an idea about the ability of MPI-ESM in reproducing the intra-daily air-sea interactions, I compare the simulated diurnal cycle of net heat flux, SST, and mixed-layer depth at a grid point near (0°N, 140°W) with those of observation collected close to the selected grid point. The observation of a mooring near (0°N, 140°W) (Fig.4.3a) shows that the net heat flux (black) is positive during the daytime (around 7:00 - 18:00) and is negative in the nighttime (around 18:00 to 7:00), indicating that the ocean gains the heat at daytime and loses heat in the nighttime. The diurnal cycle of the observed SST (red) is highly correlated to the net heat flux. The SST starts to increase after the net heat flux becomes positive, and starts to decrease when the net heat flux becomes negative.

In the hourly coupled MPI-ESM, the basic features of the diurnal cycle of the net heat flux and SST near (0°N, 140°W) are reproduced (black and red lines in Fig.4.3b). The major defects are an underestimation of the diurnal range of SST by about 40%. The mixed-layer-depth (blue) has also a clear diurnal cycle, with the evolution of mixed-layer depth being out of phase with that of SST (red). This relation is consistent with the idea that the mixed-layer depth is related to the stability of the surface ocean. When SST is getting warmer, the surface ocean is more stable, leading to a thinner mixed layer. On the other hand, when SST is getting colder, the surface ocean tends to be more unstable, leading to a deeper mixed layer. The diurnal cycle of the mixed-layer depth indicates that the vertical structure of the ocean responds to the diurnal cycle of SST.

In order to describe the diurnal cycle of convection, the OLR anomalies in hourly coupled MPI-ESM are decomposed into daytime and nighttime and averaged over all years. The daytime and nighttime are defined by the local solar radiation larger and smaller than zero W/m^2. As shown in Fig.4.4, the convection over the tropical Pacific has clear diurnal cycle, which is stronger in the nighttime and weaker in the daytime. The diurnal cycle of convection over the tropical Pacific may because that, in the nighttime, air loses heat rapidly by radiation while

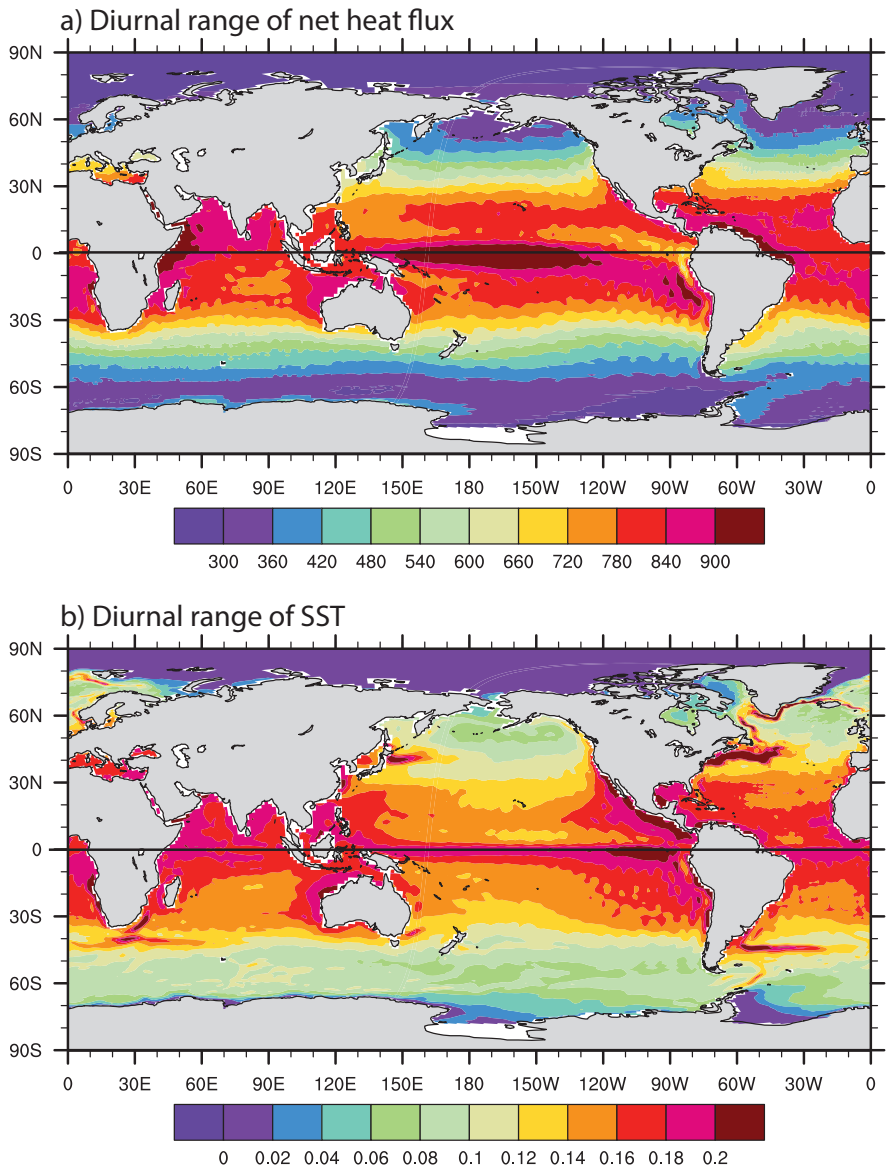

Fig. 4.2: The 50-year mean of the diurnal ranges of (a) the net heat flux (W/m^{-2}) and (b) the SST (K). The diurnal ranges are the differences between maximum value in one day and the minimum value in one day (daily maximum - daily minimum) obtained from 50-year hourly data in experiment HC.

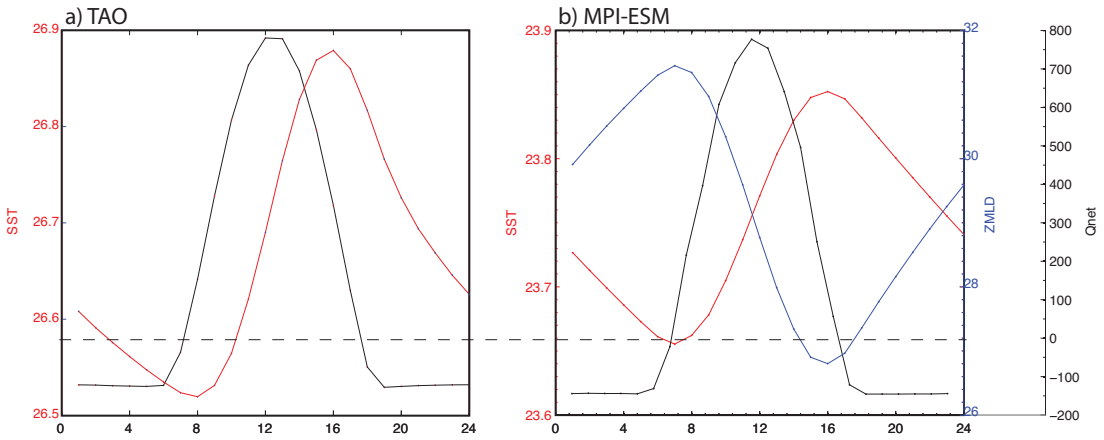

Fig. 4.3: (a) Diurnal cycle of the net heat flux (black solid) and SST (red) obtained from a mooring near (0°N, 140°W). (b) Diurnal cycle of the net heat flux (black), SST (red) and the mix-layer depth (blue) at grid point near (0°N, 140°W) by MPI-ESM. The black dashed line indicates zero of net heat flux.

the SST below decreases more slowly because of the large heat capacity of water. Therefore, the stability of the atmosphere decreases in the nighttime, leading to more convection. At daytime, the increases of the SST is slower than that of the air above, the stability of the atmosphere increases, leading to less convection. The diurnal cycle of precipitation in ECHAM6 has been compared with observation in (Hohenegger and Stevens 2013) and it is found that the diurnal cycle of precipitation over ocean can be produced by the model, though it peaks too early.

Since increasing the coupling frequency from daily to hourly allows MPI-ESM to produce the effects of diurnal cycle of net heat flux on the SST, mixed-layer depth and atmospheric convection, these intra-daily interactions between the atmosphere and the ocean may also be able to affect the simulated ENSO asymmetry in the hourly coupled MPI-ESM. The effects of intra-daily air-sea interactions on ENSO asymmetry can be described by the differences between experiment HC and experiment DC, because the interactions can be produced in the hourly coupled experiment but can not be resolved in the daily coupled experiment.

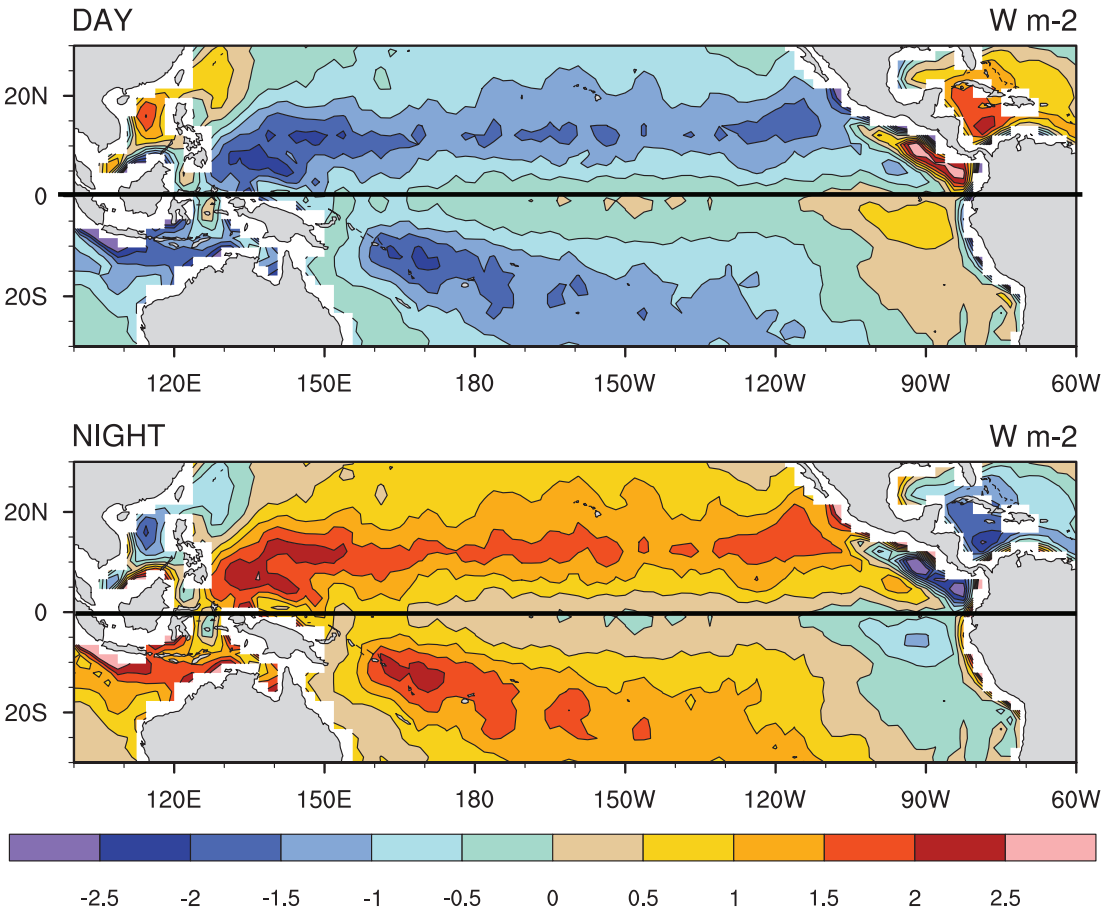

Fig. 4.4: (a) mean of OLR anomalies in the daytime. (b) mean of OLR anomalies in the nighttime. The anomalies are obtained by subtracting the monthly climatological values from the respective hourly time series of experiment HC. Daytime is defined as the time when solar radiation is positive and the remaining time is defined as nighttime.

4.3 Results

4.3.1 The ENSO asymmetry in observations and models

The composites of SST anomalies of El Niño and La Niña based on 50-year observational data (HadISST, Rayner et al. (2003)) show that the magnitude of El Niño (Fig.4.5b) is stronger than that of La Niña (Fig.4.5a). The sum of El Niño and La Niña (Fig.4.5c) is not zero, but exhibits warm anomalies up to $0.4°C$ in the eastern equatorial Pacific and cold anomalies up to $-0.1°C$ in the western equatorial Pacific.

As many other CMIP5 models, the daily coupled MPI-ESM can not reproduce the ENSO asymmetry. The simulated El Niño (Fig.4.6d) has the same magnitude as the simulated La Niña (Fig.4.6a), thus the sum of El Niño and La Niña is close to zero (Fig.4.6g). However, when increasing the coupling frequency from daily to hourly, the magnitude of El Niño (Fig.4.6e) becomes larger than that of La Niña (Fig.4.6b), and thus the sum of El Niño and La Niña reveals warm anomalies in the central and eastern Pacific, and cold anomalies in the western Pacific (Fig.4.6h). Therefore, the ENSO asymmetry can be captured by MPI-ESM when increasing the coupling frequency from daily to hourly. The differences of the composites between experiment HC and DC (HC-DC) (Fig.4.6c,f,i) show that the improvements of the simulation of ENSO asymmetry (Fig.4.6i) are mainly attributed to the factor that increasing the coupling frequency amplifies the amplitude of El Niño (Fig.4.6f) but does not change the amplitude of La Niña (Fig.4.6c).

This distribution is much closer to observations (Fig.4.5c). The ENSO asymmetry can also be indicated by the skewness of the Niño3-index, defined as $m_3/(m_2)^{3/2}$, where m_k is the kth moment, $m_k = \left(\sum_{i=1}^{N}(X_i - \overline{X})^k\right)/N$, where X_i is the ith sample of Niño3-index, $\overline{X}$ is the mean, and N is the number of sample. In the observation, the skewness of the recent 50 years Niño3-index is 1.02. Using 50 years of simulation, the skewness of Niño3-index is -0.02 in experiment DC and is 1.23 in experiment HC. When considering last 200 years of the two experiments and calculating skewness from overlapping 50-year windows, we find that skewness varies over time with values generally larger than zero in experiment HC and smaller than zero in experiment DC. Thus, ENSO asymmetry is a robust feature of experiment HC.

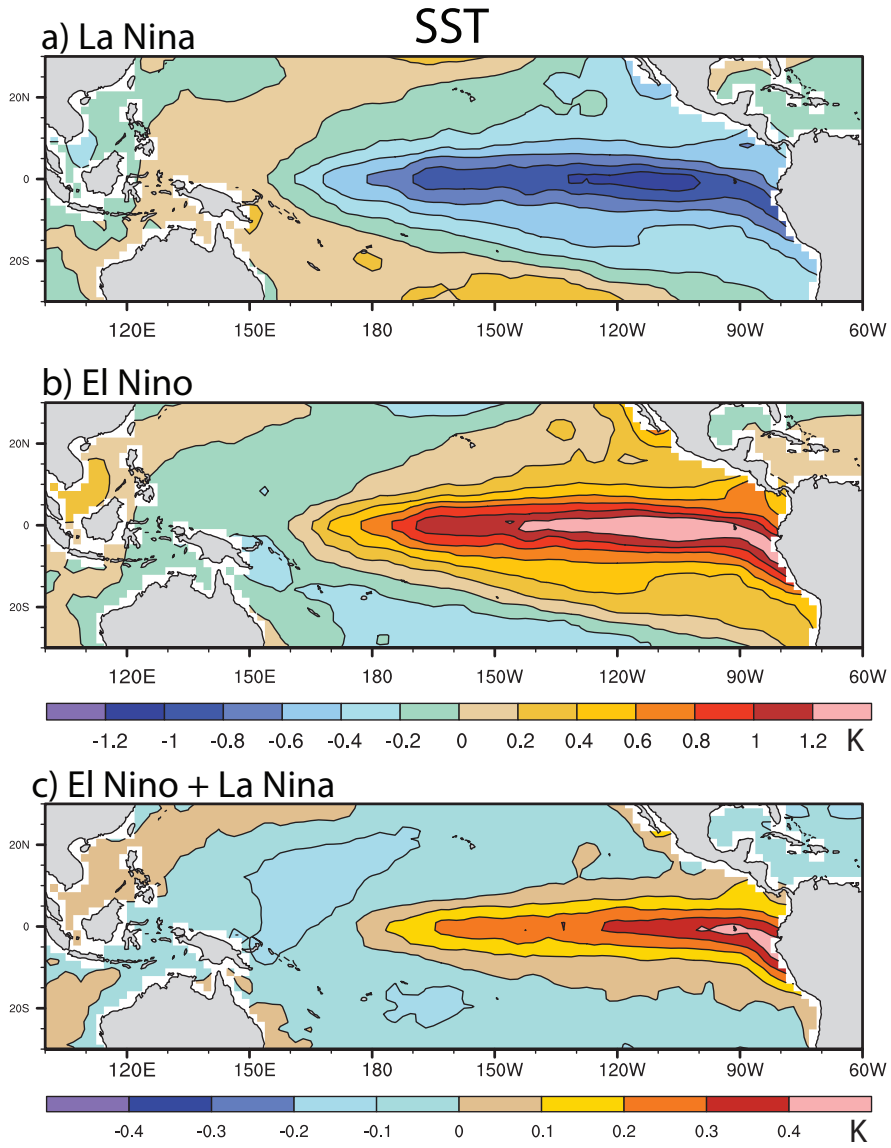

Fig. 4.5: Composites of SST anomalies in observation for La Niña (a) and El Niño (b) and the sum of the two phases (c), obtained from 50-year monthly data from HadISST. The anomalies are obtained by subtracting the monthly climatological values from the respective monthly time series. The composite of El Niño is obtained when the Niño-3 index is larger than $0.5°C$, the composite of La Niña is obtained when the Niño-3 index is smaller than $-0.5°C$.

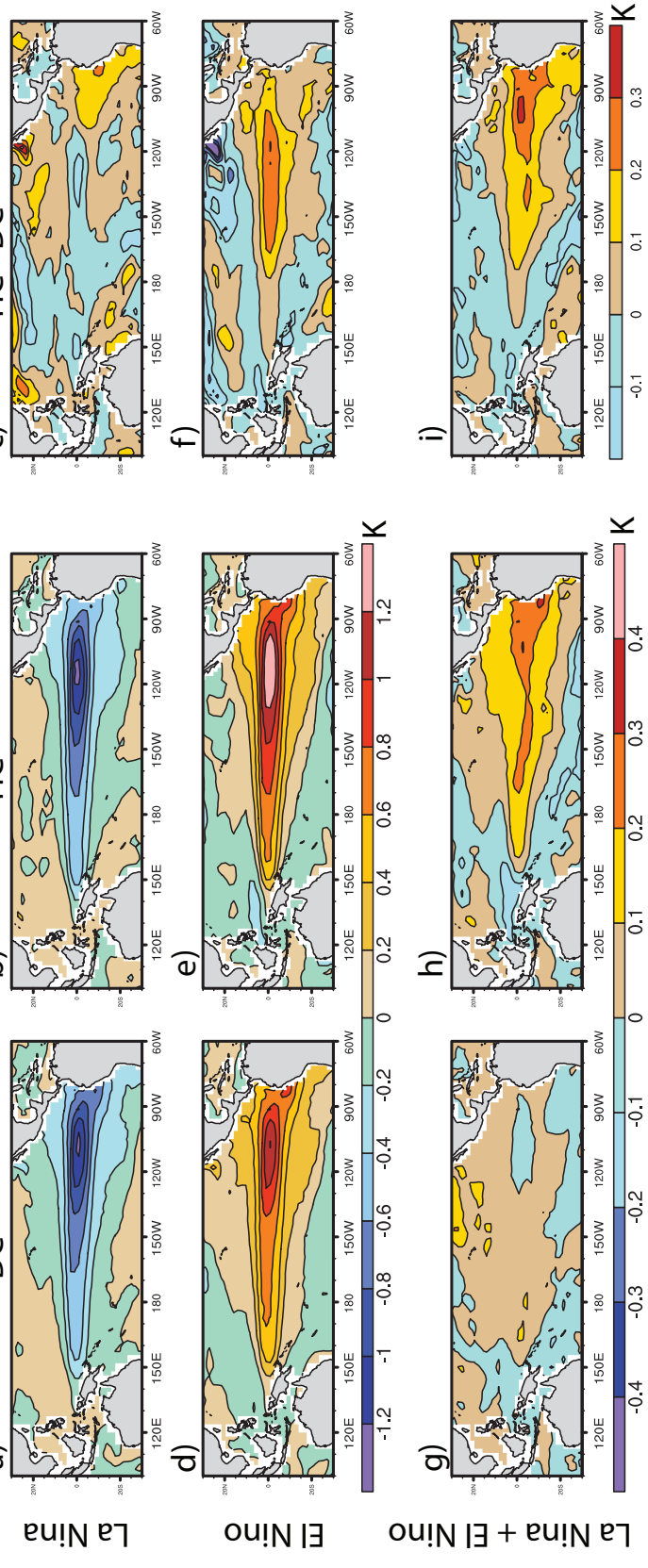

Fig. 4.6: Composites of monthly SST anomalies in experiment DC (a,d,g), experiment HC (b,e,h) and the differences (HC-DC) (c,f,i) for La Niño (a,b,c), El Niño (d,e,f) and the sum of La Niña and El Niño (g,h,i) obtained from 50-year monthly data from experiment HC and DC. The anomalies are obtained by subtracting the monthly climatological values from the respective monthly time series. The composites of El Niño are obtained when the Niño-3 index is larger than $0.5°C$, the composites of La Niña are obtained when the Niño-3 index is smaller than $-0.5°C$.

4.3.2 Asymmetry of Walker circulation

To understand why increasing the coupling frequency from daily to hourly amplifies El Niño but does not affect La Niña, the anomalies of the Walker circulation in ENSO years are investigated.

The Walker circulation is a conceptual model of the air flow in the tropical troposphere (Lau et al. 2002). As shown in Fig.4.7a, the time-mean Walker circulation is a closed circulation in zonal and vertical directions: low-level winds blow from east to west, accompanied by ascending motion over the western Pacific, returning flow from west to east in the upper troposphere, and descending motion over the cold water of the central and eastern Pacific. The ascending motion over the western Pacific with deep convection characterized by OLR greater than $-240W/m^2$ (upper panel in Fig.4.7a) and SST warmer than $28°C$ (Bottom panel in Fig.4.7a).

During El Niño phase, the Walker circulation is weaker than normal, characterized by an anomalous circulation (Fig.4.7b) which opposes the time-mean Walker circulation (Fig.4.7a). The descending branch of the time-mean Walker circulation is suppressed by positive convection anomalies in the central and eastern Pacific (indicated by the composite of equatorial OLR in the upper panel of Fig.4.7b), where the SST is warmer than normal (indicated by the composites of equatorial SST anomalies in the bottom panel of Fig.4.7b). The enhanced deep convection warms the upper troposphere by releasing latent heat in deep convective clouds. The warming of the upper troposphere leads to a decrease of the local sea level pressure and a weakening of the zonal gradient of sea level pressure and a weakening of the easterlies in the eastern Pacific. On the contrary, during La Niña phase, Walker circulation is stronger than normal, characterized by an anomalous circulation which reinforces the time-mean Walker-circulation (Fig.4.7c). The Walker circulation is amplified by the anomalies of convection shown by the OLR composites in the upper panel of Fig.4.7c. Because the convection is enhanced in the western Pacific and suppressed in the central and eastern Pacific, the ascending and descending branches of Walker circulation are both enhanced.

Apart from the known features of Walker circulation including its modification due to ENSO, Fig4.7 also suggests a less-known feature, namely the asymmetry of ENSO-related modifications of Walker circulation. As quantified by the composites of equatorial SST and OLR anomalies, the modification due to El Niño is stronger than that due to La Niña events. Since the modifications of Walker

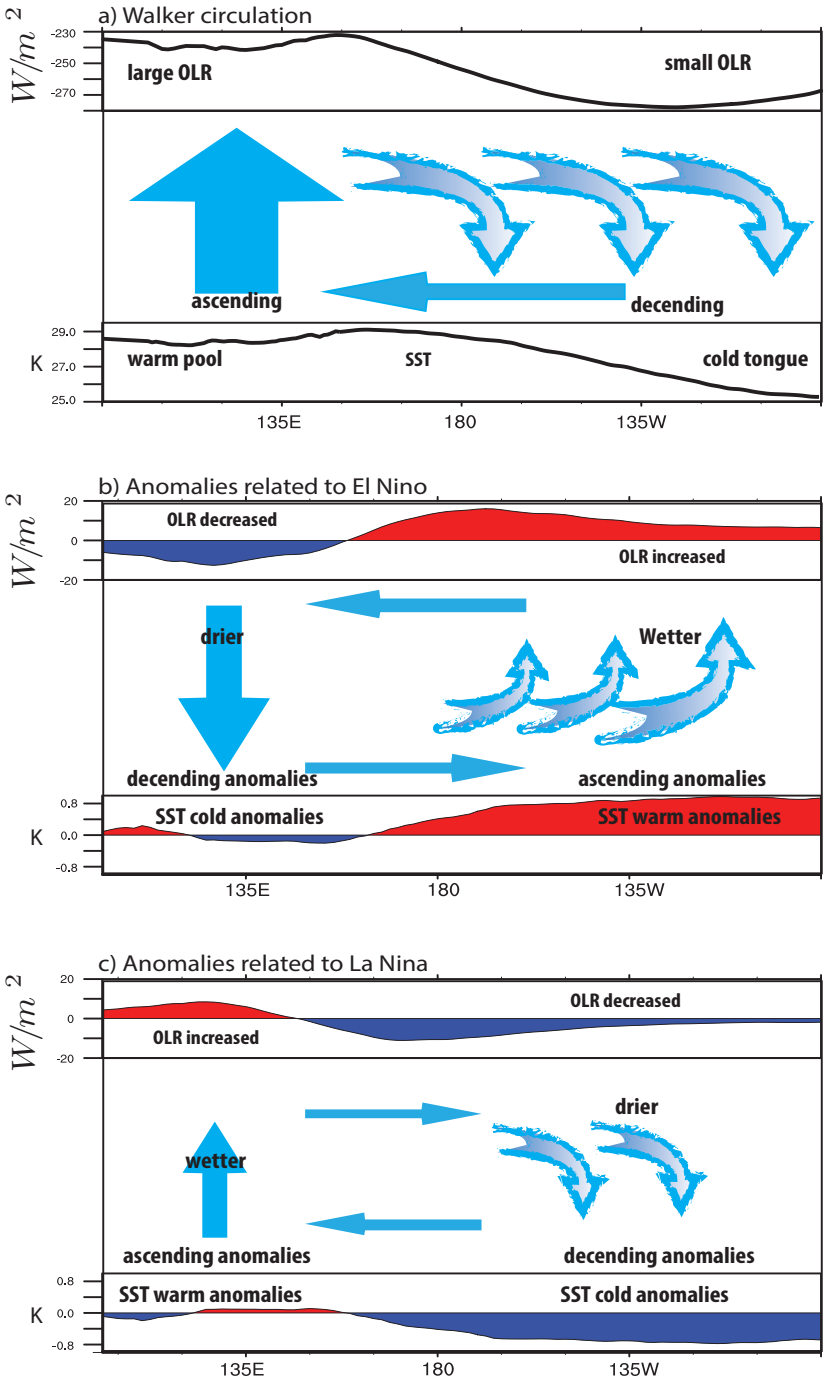

Fig. 4.7: Schematic diagrams of (a) the time-mean Walker circulation, (b) anomalous Walker circulation during El Niño Phase, (c) anomalous Walker circulation during La Niña Phase. Added to the schematic diagrams are time-mean and composites of the anomalies of equatorial (averaged over latitudes of $5°N - 5°S$) OLR (above the respective schematic diagram) and SST (below the respective schematic diagram). SST are taken from 50-year HadISST data and OLR from ERA-Interim data.

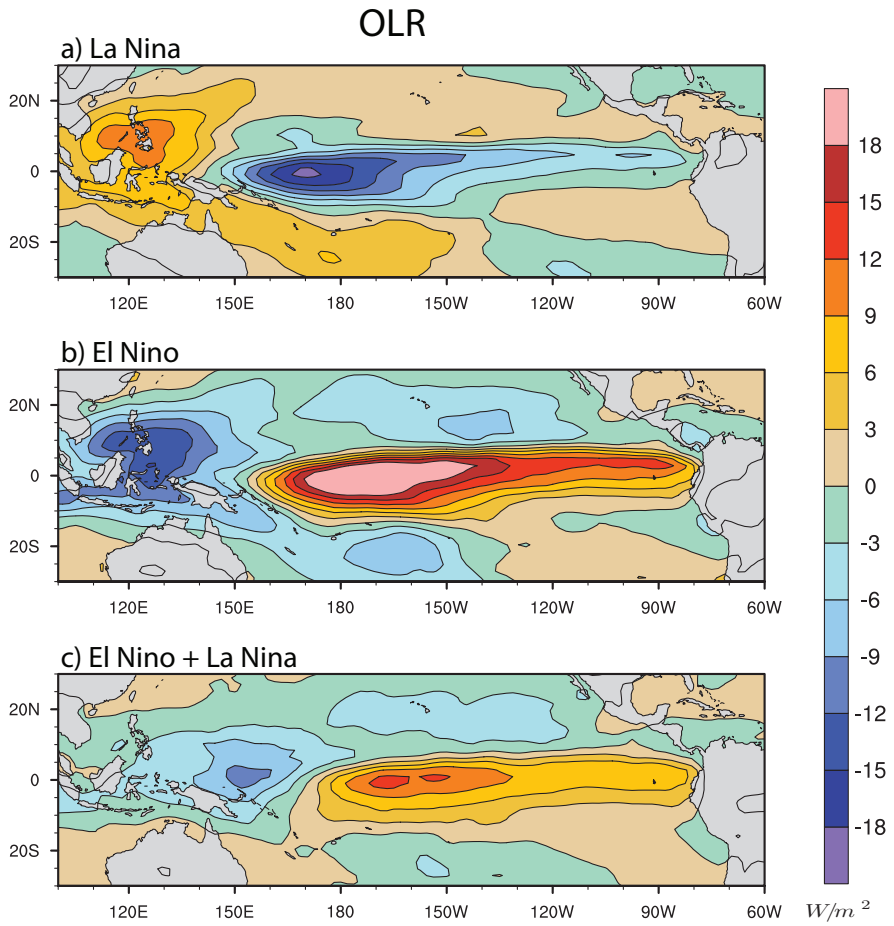

Fig. 4.8: Composites of OLR anomalies for La Niña (a) and El Niño (b) and the sum of El Niño and La Niña (c) from ERA-Interim data. The anomalies are obtained by subtracting the monthly climatological values from the respective monthly time series. The composites of El Niño are obtained when the Niño-3 index in HadISST is larger than $0.5°C$, the composites of La Niña are obtained when the Niño-3 index in HadISST is smaller than $-0.5°C$.

circulation are strongly related to convection, we further quantify this asymmetry by considering the composites of the observed 2-dimensional OLR anomalies obtained according to HadISST Niño3-index (Fig.4.8). In La Niña years (Fig.4.8a), the positive anomalies of OLR in the western Pacific indicate an enhancement of the ascending branch of Walker circulation, and the negative anomalies in the central and eastern tropical Pacific indicate an enhancement of the descending branch of Walker circulation. In El Niño Years (Fig.4.8b), OLR anomalies are negative in the western Pacific and positive in the central and eastern Pacific, indicating the suppression of the ascending and descending branches of Walker circulation.

The sum of OLR anomalies of El Niño and La Niña years (Fig.4.8c) is not zero. It shows positive anomalies in central and eastern Pacific and negative anomalies in the western Pacific, which resembles the OLR anomalies in El Niño years (Fig.4.8b). This suggests that the amplitude of the anomalies of Walker circulation in El Niño years is larger than the anomalies in La Niña years. The asymmetry of the anomalies of the Walker circulation is not confined to the equator, but has a meridional extent over $10 - 20$ degrees.

As investigated in Section 4.3.1, increasing coupling frequency from daily to hourly enhances the strength of El Niño but has minor effects on the strength of La Niña. This result is obtained by considering SST-composites. Do we get the same result for OLR and Walker circulation in the sense that increasing coupling frequency leads to stronger modification during El Niño than during La Nina, whereby enhancing the asymmetry of Walker circulation in experiment HC? To answer this question, the anomalies related to Walker circulation in experiment HC are compared with those in experiment DC. The anomalies of Walker circulation are detected from the composites of the anomalies of SST, OLR, surface zonal wind stress and oceanic potential temperature obtained according to model Niño3-index.

In La Niña phase, the SST in the central and eastern tropical Pacific is colder than normal. Corresponding to the SST anomalies (Fig.4.6b), the negative anomalies of OLR in Fig.4.9a,c indicate that the descending branch of the Walker circulation east of 120° E is enhanced. Since the Walker circulation is enhanced, the easterly wind stress along the equator are stronger than normal (Fig.4.10a and c). In the ocean, the enhanced easterlies transport the warm surface water westward. The upper-layer potential temperature is colder in the eastern Pacific and warmer in the western Pacific (Fig.4.11a,c). Comparing the variables related

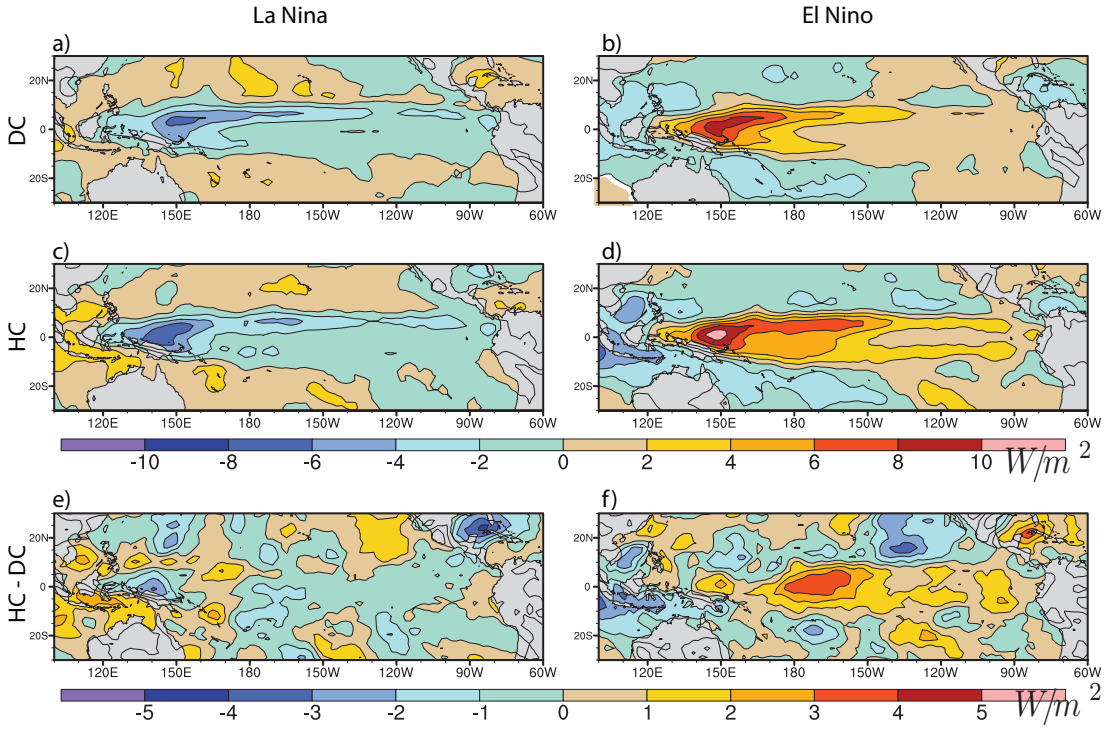

Fig. 4.9: Composites of OLR anomalies (full sky-clear sky) obtained from 50-year daily data in experiment DC (a,b), 50-year houly data in experiment HC (c,d) and the difference between HC and DC (HC-DC) (e,f) for the La Niña (a,c,e) and El Niño (b,d,f). The anomalies are obtained by subtracting the monthly climatological values from the respective time series in experiment HC and DC. The composites of El Niño are obtained when the respective Niño-3 index in each experiment is larger than $0.5°C$, the composites of La Niña are obtained when the Niño-3 index is smaller than $-0.5°C$.

to Walker circulation in experiment HC and DC, it is found that the anomalies of OLR (Fig.4.9e), easterly wind stress (Fig.4.10e) and oceanic potential temperature (Fig.4.11e) are comparable in experiment HC and DC. This indicates that during the La Niña phase, the effects of the intra-daily air-sea interactions on the Walker circulation in experiment HC are negligible.

In El Niño years, the anomalies of OLR (Fig.4.9b,d) are enhanced east of 120° E. The descending branch of Walker circulation is suppressed. As shown in Fig.4.10b,d, the easterly wind stress anomalies are weaker than normal along the equator. The upper-layer potential temperature in the ocean is warmer than normal in the eastern Pacific (Fig.4.11b,d). Comparing these anomalies in experiment HC and DC shows that the amplitudes of positive OLR anomalies in the central tropical Pacific and the negative OLR anomalies in the western tropical

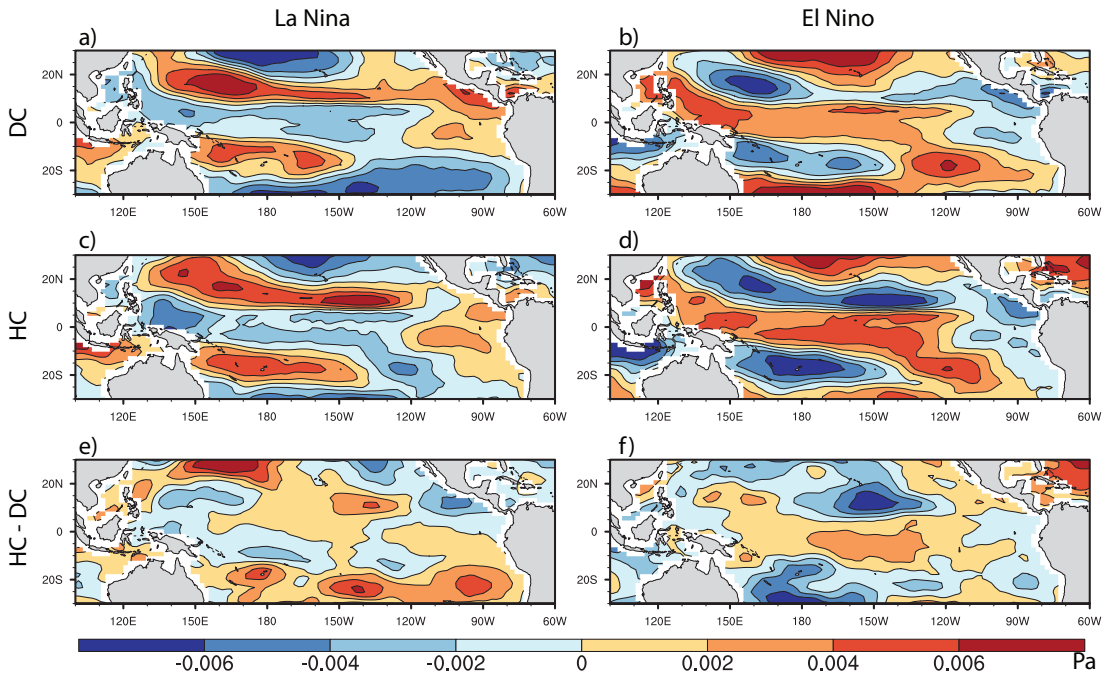

Fig. 4.10: Composites of anomalies of zonal wind stress in 50-year daily data in experiment DC (a,b), 50-year hourly data in experiment HC (c,d) and the difference between HC and DC (HC-DC) (e,f) for the La Niña (a,c,e) and El Niño (b,d,f). The anomalies are obtained by subtracting the monthly climatological values from the respective time series in experiment HC and DC. The composites of El Niño are obtained when the respective Niño-3 index in each experiment is larger than $0.5°C$, the composites of La Niña are obtained when the respective Niño-3 index is smaller than $-0.5°C$.

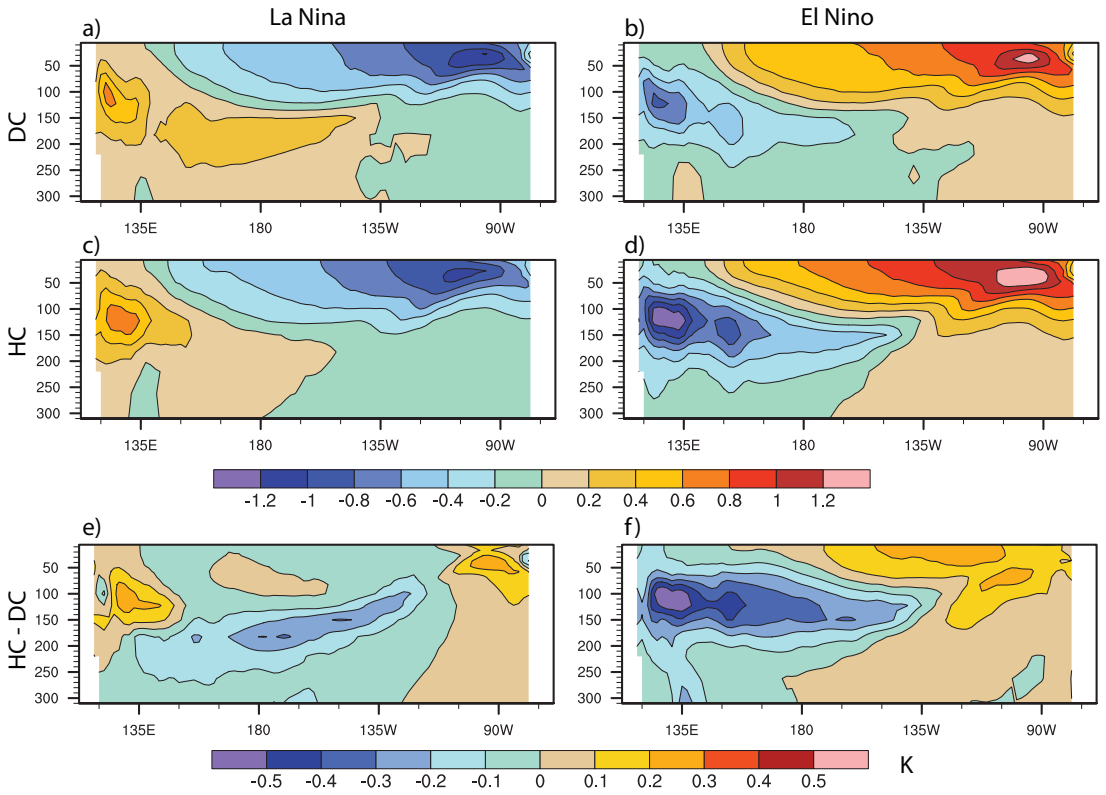

Fig. 4.11: Composites of meridional mean of oceanic potential temperature anomalies at latitudes of $5°N - 5°S$ as a function of depth in experiment DC (a,b), experiment HC (c,d) and the difference between HC and DC (HC-DC) (e,f) for La Niña (a,c,e) and El Niño (b,d,f). The anomalies are obtained by subtracting the monthly climatological values from the respective time series in experiment HC and experiment DC. The composites of El Niño are obtained when the respective Niño-3 index in each experiment is larger than $0.5°C$, the composites of La Niña are obtained when the respective Niño-3 index is smaller than $-0.5°C$.

Pacific are larger in experiment HC than in DC (Fig.4.9f). The amplitudes of the anomalies of wind stress along the equator (Fig.4.10f) and the oceanic potential temperature (Fig.4.11f) are also larger in experiment HC than in DC. This indicates that the intra-daily air-sea interactions included in experiment HC produce larger changes in Walker circulation in El Niño years than in La Niña years.

In summary, the modifications of Walker circulation due to El Niño and La Niña events are not the same in the observation. This asymmetry of Walker circulation is better simulated in experiment HC than in experiment DC. Increasing coupling frequency has weaker effects on Walker circulation in La Niña years than in El Niño years. As a result, the amplitudes related to La Niña events are comparable in the two experiments, whereas those related to El Niño events are stronger in experiment HC than in experiment DC.

4.3.3 Role of diurnal cycle of convection for the asymmetry

The modification of Walker circulation due to ENSO involves the Bjerknes feedback discussed in Section 3.3.3. Since Bjerknes feedback has a diurnal cycle, it is possible that the different modification of Walker circulation due to El Niño and La Niña are induced by changes in diurnal cycles. This possibility is investigated in this subchapter with focus on convection.

On intra-daily timescales, convection can be affected by the diurnal cycle of SST as discussed in section 4.2.2. The diurnal cycle of SST in experiment HC, as shown in Fig.4.2b, has the mean maximum along the equator with the values about $0.15°C$, amounts to 20% of the SST anomalies caused by ENSO. It is assumed that the diurnal cycle of SST affects convection differently during El Niño and La Niña phases. The difference of the effects may be attributed to the background SST in the central tropical Pacific. During La Niña phase, the background SST is colder than normal. Convection is suppressed there. The diurnal cycle of SST has minor influence on the convection. During the El Niño phase, however, the background SST is warmer than normal. The additional SST warming caused by the diurnal cycle could trigger more convection in El Niño phase.

To investigate this assumption, time series of hourly OLR anomalies obtained from experiment HC are decomposed into daytime and nighttime and averaged over all years, over El Niño years and over La Niña years, respectively. The daytime and nighttime are defined by the local solar radiation larger and smaller than zero W/m^2, respectively. For the long-term mean, the results are shown in

Fig.4.12a,b. The convection over the tropical Pacific is stronger in the nighttime and weaker at the daytime. The diurnal range of the convection, defined as the difference between night and day (night-day) (Fig.4.12c) is zonally distributed with the maximum along $10°N$ and $10°S$ and the minimum along the equator.

During the El Niño phase, the convection also has a diurnal cycle. Decomposing the OLR anomalies into daytime and nighttime (Fig.4.12d,e) shows that the enhanced convection equatorward of 10° is stronger in the nighttime than in the daytime. The diurnal range of the convection in El Niño years is different to that of the long-term mean. As shown in Fig.4.12f, the diurnal range over the western equatorial Pacific is increased in comparison with that of the long-term mean (Fig.4.12c). The increase of diurnal range of the convection is mainly caused by an enhancement of convection in the central tropical pacific in the nighttime. In the nighttime, the cooling of the SST, which is warmed at daytime, is slower than the cooling of the air above, leading to an unstable atmosphere. In addition to the warm anomalies of the background SST in El Niño years, more convection are triggered in the nighttime.

For the La Niña phase (Fig.4.12g,h), the convection anomalies in the tropical Pacific are negative in the region of $10°S - 10°N$ in both daytime and nighttime but the negative anomalies along the equator are stronger in the daytime than in the nighttime. Though the distribution of day and night convection in La Niña years are different to that of the long-term mean, the diurnal range of the convection (Fig.4.12i) has the similar distribution as that of the long-term mean (Fig.4.12c), with the maximum zonal distributed along $10°N$ and $10°S$ and the minimum along the equator. This similarity indicates that the intra-daily air-sea feedback has minor effects on the anomalies of convection in La Niña years.

In summary, the convection in the central tropical Pacific is more strongly affected by the diurnal cycle of SST in El Niño years than in La Niña years. In particular, the nighttime convection is much more enhanced during El Niño years over the anomaly warmer central equatorial Pacific when the background SST is increased and the atmosphere becomes more unstable. As shown in Fig.4.12j, this enhancement of convection, which outweigh the reduction of nighttime convection during La Niña years, leads to a stronger El Niño and stronger El Niño-related modification of Walker circulation.

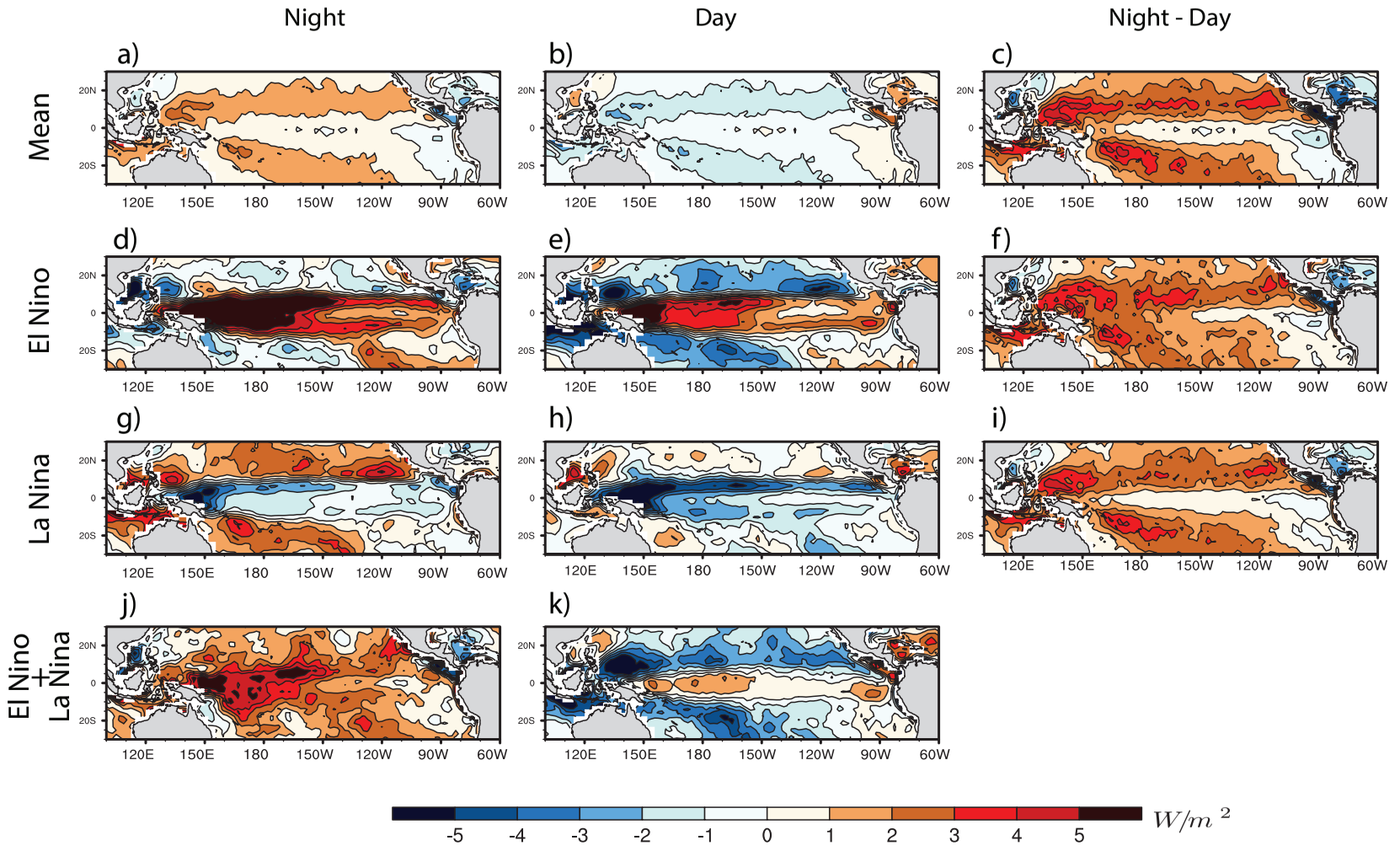

Fig. 4.12: Composites of OLR anomalies (full sky-clear sky) in the nighttime (left column), daytime (middle column) and the difference (night-day) (right column) for long-term mean (a-c), El Niño (d-f), La Niña (g-i) and the sum of El Niño and La Niña (j-k), obtained from 50-year hourly data in experiment HC. Daytime is defined as the time when solar radiation is positive and the remaining time is defined as nighttime. The composites of El Niño are obtained when the Niño-3 index in experiment HC is larger than $0.5°C$, the composites of La Niña are obtained when the respective Niño-3 index is smaller than $-0.5°C$.

4.4 Conclusions

4.4.1 Summary

ENSO is not symmetric: El Niño is stronger than La Niña. However, the simulated ENSO in many CMIP5 models, including MPI-ESM, is almost symmetric. This work finds that ENSO asymmetry can be simulated by MPI-ESM when increasing the air-sea coupling frequency from daily to hourly. These changes are caused by the intra-daily air-sea interactions included in the hourly coupled model.

Comparing the anomalies of Walker circulation in hourly and daily coupled experiments during El Niño and La Niña years suggests that the anomalies of Walker circulation in La Niña years are comparable in the two experiments, indicating that the intra-daily air-sea interactions do not notably influence the strength of La Niña. In El Niño years, the intra-daily air-sea interactions enhance the anomalies of the Walker circulation, thus, El Niño is stronger in hourly coupled experiment than in daily coupled experiment. The fact that the intra-daily air-sea interactions do not change the strength of La Niña but enhance El Niño results in a better simulation of ENSO asymmetry in experiment HC.

To understand why the effects of intra-daily air-sea interactions on the anomalies of Walker circulation are different between La Niña and El Niño years, this work decomposes the OLR anomalies into daytime and nighttime and finds that, in La Niña years, the intra-daily air-sea interactions have minor effect on the diurnal cycle of the convection. In El Niño years, however, the diurnal cycle of SST amplifies the convection in the nighttime in the central equatorial Pacific. The enhanced convection in the equatorial Pacific amplifies the anomalies of the Walker circulation through Bjerknes feedback, and amplifies the El Niño events. Consequently, the simulated El Niño is stronger than La Niña in the hourly coupled experiment.

4.4.2 Discussion

In addition to the CMIP5-version of MPI-ESM-LR (ECHAM6 T63) that was used in the above analysis, the daily and hourly coupled MPI-ESM-HR (ECHAM6 T127) and MPI-ESM-XR (ECHAM6 T255) based on the latest version of MPI-ESM are used to test the importance of intra-daily air-sea interactions on the ENSO asymmetry. As shown in Fig.4.13, in daily coupled MPI-ESM-HR (Fig.4.13d),

the ENSO asymmetry is not adequately simulated. However, the ENSO asymmetry can be simulated when using a coupling frequency of once per hour (Fig.4.13e). This results are similar to MPI-ESM-LR (Fig.4.13b and c), even though the spatial structure with large positive anomalies in the eastern tropical Pacific (Fig.4.13a) is not completely reproduced. With the extremely high resolution model (MPI-ESM-XR), only a simulation with a coupling frequency of once per hour is available. The ENSO asymmetry can also be produced here. At this resolution, the observed spatial structure is also not completely reproduced. Nevertheless, ENSO asymmetry, as characterised by the non-zero sum of El-Niño- and La Niña-composites, is only obtained when using coupling frequency of once per hour and this result seems to be independent of model spatial resolution. To what extent the less satisfactory simulation of the pattern of the asymmetry is due to the changes in the new version of MPI-ESM requires further investigation.

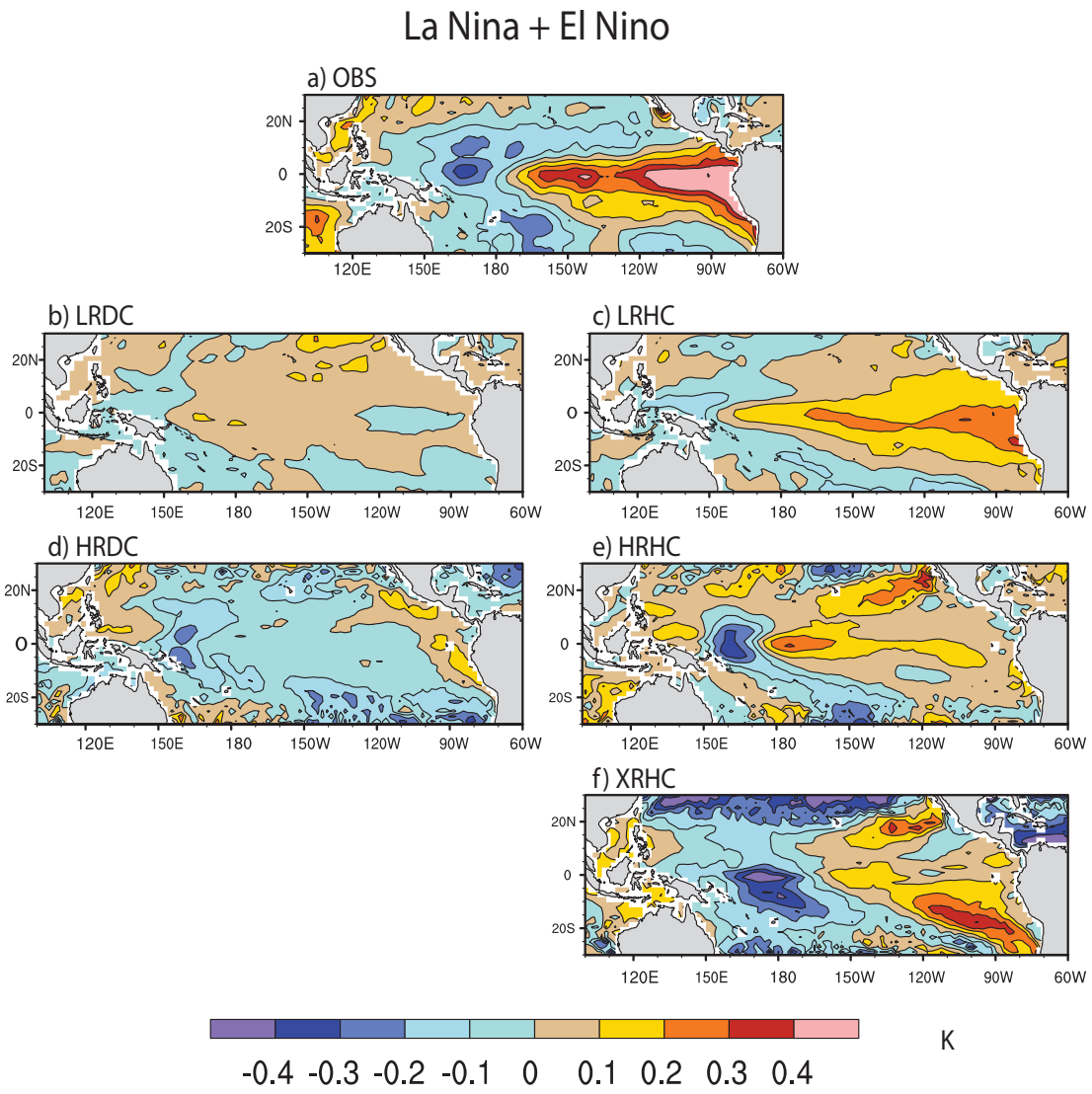

Fig. 4.13: The sum of the composites of El Niño and La Niña in (a) Observation, (b) and (c) MPI-ESM-LR with daily and hourly coupling, (d) and (e) MPI-ESM-MR with daily and hourly coupling and (f) MPI-ESM-XR with hourly coupling only.

Chapter 5

Conclusions and Outlook

5.1 Summary

This thesis aims to better understand the effects of intra-daily air-sea interactions on the large scale climate system. In order to produce the intra-daily air-sea interactions, the coupling frequency between the atmospheric and oceanic components of MPI-ESM is increased from its standard value of once per day to once per hour. The intra-daily air-sea interactions are analysed by comparing results from the hourly coupled MPI-ESM with that from the daily coupled MPI-ESM, as the daily coupled model cannot reproduce air-sea interactions with time scales shorter than one day, with focus on both the diurnal cycle and the intra-daily fluctuations.

The analyses are done in three steps. In the first step, whether and to what extent coupling frequency from once per day to once per hour is capable of reducing some long-standing biases are examined (Chapter 2). The second step quantifies the statistics of the diurnal cycle and random intra-daily fluctuations of the air-sea fluxes at grid point level and studies the air-sea interactions that lead to large-scale changes (Chapter 3). For this purpose, an effective method is developed to distinguish effects arising from daily/hourly averaging from those directly arising from air-sea interactions occurring on diurnal and intra-diurnal time scales. In the third step, this work investigates whether air-sea interactions on intra-daily time scales can influence the longer time scale phenomenon, ENSO, through non-linear interactions. Specifically, it quantifies the role of diurnal cycle of convection and its dependence on background SST on the ENSO asymmetry (Chapter 4).

Below, I give conclusions in form of answers to the questions raised in the introduction of this thesis (Chapter 1).

5.2 Answers to the research questions

Can parametrizations directly respond to changes in coupling frequency?

The parametrizations of surface fluxes in form of bulk formulas can directly respond to an increase in coupling frequency. Because of the non-linear nature of these formulas, random intra-daily fluctuations arising from hourly coupling increase the probability of extremely weak or extremely strong momentum fluxes. The fluctuations also increase the probability of having fresh water fluxes with negative values around $-0.1\,mm\,day^{-1}$. The diurnal cycle dominates the intra-daily variability of the net heat flux. The convective precipitation in most parts of the equatorial ocean is enhanced in the hourly coupled model. Generally, the bulk formulas and the convection scheme used in MPI-ESM do respond to increasing coupling frequency from once per day to once per hour.

What are the biases in the standard daily coupled MPI-ESM? Are they improved in the hourly coupled model?

To evaluate the performance of the hourly coupled MPI-ESM, I focus on the known biases of SST, oceanic potential temperature and troposphere westerlies. In the daily coupled MPI-ESM, the simulated SST is too warm in the Southern Ocean and too cold in the central equatorial Pacific. The simulated oceanic potential temperature is too warm at intermediate levels and in the deeper ocean. The westerly wind around $60°S$ is underestimated.

In MPI-ESM, increasing coupling frequency from once per day to once per hour decreases many of these model biases. When increasing the coupling frequency, the simulated SST is increased in most part of the subtropical and tropical ocean and decreased in the high latitude ocean. Hence, the cold biases of SST in the western equatorial Pacific and subtropical ocean in the southern Hemisphere are decreased. The warm SST biases in the Southern Ocean are also decreased. The decrease of the SST biases amounts by up to 10%. The westerly wind increases around $60°S$ throughout the troposphere, with the bias decreased by up to 10%. The potential temperature of the ocean decreases at high latitudes when increasing the coupling frequency. The bias reduction in the Southern Ocean amounts up to 20%.

What are the effects of increasing coupling frequency on the basic statistics of air-sea surface fluxes at grid point level?

For the basic statistics, this work considers the time means, the variances and

the extremes.

1. Regarding the time means: Significant changes of the means are found for the magnitude of momentum flux, with an increase of up to 10% over the Southern Ocean and a decrease of up to 7% in the equatorial Pacific.

2. Regarding the variances: Increasing the coupling frequency from daily to hourly increases the variances by up to 50% for the magnitude of momentum flux, up to 100% for the fresh water flux and up to 15 times for the net heat flux. Exceptions are found in the tropics, where high-frequency feedbacks reduce the variances, most significantly those of the momentum and fresh water flux. The diurnal and intra-diurnal variations resolved in hourly coupled experiment vary in their strengths with seasons and amount up to 50% to 90% of the respective total variances.

3. Regarding the extremes: The extremes are generally reduced by daily coupling, as the daily averaging smooths out the extremes. The reduction in the 10^{th} and 90^{th} percentiles reaches between 10 and 20% for momentum fluxes, about 40% for fresh water fluxes, and about a factor of 5 for the net heat flux. Exceptions are found in the tropics, in particular over the equatorial Pacific, where the weak momentum fluxes over the central equatorial Pacific are strengthened, the strong momentum fluxes over the western equatorial Pacific are weakened, and the weak evaporation over the central equatorial Pacific is enhanced.

Which processes are responsible for the changes in basic statistics of air-sea fluxes?

The intra-daily variabilities in hourly coupled MPI-ESM are partly caused by the different averaging intervals used before exchanging information between atmosphere and ocean, and partly caused by the intra-daily air-sea feedbacks which can only be resolved by hourly coupled MPI-ESM. This work separates the effect of daily averaging from that of air-sea feedbacks occurring within a day. I find that the increases in variances and extremes are mainly due to the daily averaging which removes a considerable amount of the variance and extremes that is related to high-frequency turbulent fluctuations in the momentum flux and the fresh water flux in mid- and high-latitudes and to the diurnal cycle of the net heat flux almost everywhere over the ocean. The intra-diurnal air-sea feedbacks are responsible for changes of the mean momentum fluxes in the tropical Pacific and Southern Ocean and decreases of variance and extremes over the tropical oceans.

How does the intra-daily air-sea feedback affect large-scale patterns of air-sea fluxes?

In the Southern Ocean, the SST-wind-stress feedback is characterized by weaker/stronger wind stress anomalies over warmer/colder SST and the re-enforcement of wind stress anomalies due to changes in temperature gradients. This feedback is different in daily and hourly coupled experiments. The difference of the SST-wind-stress feedback seems to arise from the dependence of the feedback on the background SST, with the SST-wind-stress feedback being only found when the background SST is sufficiently warm. This SST-dependence can be responsible for the different SST-wind-stress feedbacks, found in daily and hourly coupling experiment. Because the SST is colder in hourly coupled experiment, the SST-wind-stress feedback is modified. This modification causes the increase of the magnitude of wind stress over the Southern Ocean.

In the Equatorial Pacific, the decrease of the magnitude of wind stress is related to the diurnal cycle of Bjerknes feedback which cannot be simulated in the daily coupled experiment. In the hourly coupled experiment, the Bjerknes feedback has a diurnal cycle during the El Niño events with enhanced westerly anomalies in the nighttime but weaker ones in the daytime. During La Niña events, there is no clear diurnal cycle of westerly winds. This results in westerly anomalies on average along the equator in hourly coupled experiment. As the climate mean wind stress in the equatorial Pacific is easterly, the magnitude of the wind stress is weaker in hourly coupled experiment than in daily coupled experiment.

Can hourly coupling improve the model's ability in simulating the ENSO asymmetry, and if yes, why?

El Niño is stronger than La Niña. However, the simulated ENSO in daily coupled MPI-ESM is almost symmetric. This error is corrected when simulating intra-daily air-sea interactions by increasing coupling frequency from daily to hourly. The intra-daily air-sea interactions do not notably influence the strength of La Niña, but they strengthen El Niño. This is because that the intra-daily air-sea interactions has minor effect on the diurnal cycle of convection in La Niña years. In El Niño years, on the contrary, the diurnal cycle of SST amplifies the convection in the central equatorial Pacific where the background SST is anomalously warm, especially in the nighttime when the atmosphere over the anomalously warm central Pacific is less stable. The enhanced convection in the equatorial Pacific amplifies the Bjerknes feedback, and thus amplifies the El Niño. Consequently, the simulated El Niño is stronger than La Niña in the hourly

coupled experiment.

5.3 Outlook

The results of this work are based on CMIP5-version of MPI-ESM-LR (ECHAM6 T63). Intra-daily air-sea interactions will also occur in coupled model at higher resolutions. Some improvements caused by high spatial resolution could be modified or amplified by the simulated intra-daily air-sea interactions. For example, the negative anomalies of ENSO asymmetry at longitude $160°E$ in Fig.4.13a can not be produced in hourly coupled MPI-ESM at low resolution LR (Fig.4.13c), but are partly reproduced by hourly coupled MPI-ESM at higher resolutions (Fig.4.13e and f). Similarly, the distribution of positive anomalies of ENSO asymmetry, which extends too much westward into the western equatorial Pacific in MPI-ESM-LR (Fig.4.13.c), is better simulated by MPI-ESM-HR and MPI-ESM-XR (Fig4.13 e and f). Even though the ENSO asymmetry can be robustly simulated by MPI-ESM at high resolutions, the detailed structure of the asymmetry differs among the different simulations. More work is needed to clarify whether the differences, including some improvement in higher resolution experiments, result from the enhanced spatial resolution or from the improved model physics implemented in the latest version of MPI-ESM.

On intra-daily time scales, physics in the surface layer of the ocean are important (Bernie et al. 2008; Klingaman et al. 2011). There might be rectification in the ocean's response to high frequency fluxes. However, the first model layer of the oceanic component of MPI-ESM, MPIOM, is 12 meters in depth, which is too coarse to resolve details of processes occurring in the surface layer (Fig.4.3). Further studies based on models with higher vertical resolution are required to understand the ocean processes related to the intra-daily air-sea interactions.

Bibliography

An, S.-I., Y.-G. Ham, J.-S. Kug, J. Fei-Fei, and I.-S. Kang, 2005: El niño-la niña asymmetry in the coupled model intercomparison project simulations*. *Journal of Climate*, **18 (14)**, 2617.

An, S.-I. and F.-F. Jin, 2004: Nonlinearity and asymmetry of enso*. *Journal of Climate*, **17 (12)**, 2399–2412.

An, S.-I., J.-S. Kug, Y.-G. Ham, and I.-S. Kang, 2008: Successive modulation of enso to the future greenhouse warming. *Journal of Climate*, **21 (1)**, 3–21.

Beena, B. S. and J.-S. von Storch, 2009: Effects of fluctuating daily surface fluxes on the time-mean oceanic circulation. *Climate dynamics*, **33 (1)**, 1–18.

Bernie, D., E. Guilyardi, G. Madec, J. Slingo, and S. Woolnough, 2007: Impact of resolving the diurnal cycle in an ocean–atmosphere gcm. part 1: a diurnally forced ogcm. *Climate Dynamics*, **29 (6)**, 575–590.

Bernie, D., E. Guilyardi, G. Madec, J. Slingo, S. Woolnough, and J. Cole, 2008: Impact of resolving the diurnal cycle in an ocean–atmosphere gcm. part 2: A diurnally coupled cgcm. *Climate dynamics*, **31 (7-8)**, 909–925.

Bernie, D., S. Woolnough, J. Slingo, and E. Guilyardi, 2005: Modeling diurnal and intraseasonal variability of the ocean mixed layer. *Journal of climate*, **18 (8)**, 1190–1202.

Bjerknes, J., 1969: Atmospheric teleconnections from the equatorial pacific 1. *Monthly Weather Review*, **97 (3)**, 163–172.

Bradley, E. F., 1968: A shearing stress meter for micrometeorological studies. *Quarterly Journal of the Royal Meteorological Society*, **94 (401)**, 380–387.

Buck, A. L., 1981: New equations for computing vapor pressure and enhancement factor. *Journal of applied meteorology*, **20 (12)**, 1527–1532.

Burgers, G. and D. B. Stephenson, 1999: The "normality" of el niño. *Geophysical Research Letters*, **26 (8)**, 1027–1030, doi:10.1029/1999GL900161, URL http://dx.doi.org/10.1029/1999GL900161.

Clayson, C. A. and A. S. Bogdanoff, 2013: The effect of diurnal sea surface temperature warming on climatological air–sea fluxes. *Journal of Climate*, **26 (8)**, 2546–2556.

Danabasoglu, G., W. G. Large, J. J. Tribbia, P. R. Gent, B. P. Briegleb, and J. C. McWilliams, 2006: Diurnal coupling in the tropical oceans of ccsm3. *Journal of climate*, **19 (11)**, 2347–2365.

Gentemann, C. L., P. J. Minnett, P. Le Borgne, and C. J. Merchant, 2008: Multi-satellite measurements of large diurnal warming events. *Geophysical Research Letters*, **35 (22)**.

Gille, S., 2012: Diurnal variability of upper ocean temperatures from microwave satellite measurements and argo profiles. *Journal of Geophysical Research: Oceans (1978–2012)*, **117 (C11)**.

Guemas, V., D. Salas-Mélia, M. Kageyama, H. Giordani, and A. Voldoire, 2013: Impact of the ocean diurnal cycle on the north atlantic mean sea surface temperatures in a regionally coupled model. *Dynamics of Atmospheres and Oceans*, **60**, 28–45.

Guilyardi, E., et al., 2004: Representing el niño in coupled ocean-atmosphere gcms: the dominant role of the atmospheric component. *Journal of Climate*, **17 (24)**, 4623–4629.

Ham, S., S.-Y. Hong, and S. Park, 2014: A study on air–sea interaction on the simulated seasonal climate in an ocean–atmosphere coupled model. *Climate Dynamics*, **42 (5-6)**, 1175–1187.

Ham, Y.-G., J.-S. Kug, I.-S. Kang, F.-F. Jin, and A. Timmermann, 2010: Impact of diurnal atmosphere–ocean coupling on tropical climate simulations using a coupled gcm. *Climate dynamics*, **34 (6)**, 905–917.

Hoerling, M. P., A. Kumar, and M. Zhong, 1997: El niño, la niña, and the nonlinearity of their teleconnections. *Journal of Climate*, **10 (8)**, 1769–1786.

Hohenegger, C. and B. Stevens, 2013: Controls on and impacts of the diurnal cycle of deep convective precipitation. *Journal of Advances in Modeling Earth Systems*, **5 (4)**, 801–815.

Jungclaus, J., et al., 2006: Ocean circulation and tropical variability in the coupled model echam5/mpi-om. *Journal of climate*, **19 (16)**, 3952–3972.

Jungclaus, J., et al., 2010: Climate and carbon-cycle variability over the last millennium. *Climate of the Past Discussions*, **6 (3)**, 1009–1044.

Kang, I.-S. and J.-S. Kug, 2002: El niño and la niña sea surface temperature anomalies: Asymmetry characteristics associated with their wind stress anomalies. *Journal of Geophysical Research: Atmospheres (1984–2012)*, **107 (D19)**, ACL–1.

Kawai, Y. and A. Wada, 2007: Diurnal sea surface temperature variation and its impact on the atmosphere and ocean: A review. *Journal of oceanography*, **63 (5)**, 721–744.

Kennedy, J., P. Brohan, and S. Tett, 2007: A global climatology of the diurnal variations in sea-surface temperature and implications for msu temperature trends. *Geophysical research letters*, **34 (5)**.

Klingaman, N. P., S. J. Woolnough, H. Weller, and J. M. Slingo, 2011: The impact of finer-resolution air-sea coupling on the intraseasonal oscillation of the indian monsoon. *Journal of Climate*, **24 (10)**, 2451–2468.

Kuhlbrodt, T. and A. H. Monahan, 2003: Stochastic stability of open-ocean deep convection. *Journal of physical oceanography*, **33 (12)**, 2764–2780.

Large, W. and S. Pond, 1982: Sensible and latent heat flux measurements over the ocean. *Journal of Physical Oceanography*, **12 (5)**, 464–482.

Lau, K., , and S. Yang, 2002: Walker circulation.

Levitus, S., T. Boyer, M. Conkright, D. Johnson, T. J. Antonov, C. Stephens, and R. Gelfeld, 1998: World ocean database 1998, volume 2: Temporal distribution of mechanical bathythermograph profiles. *NOAA Atlas NESDIS*, **19**.

Li, Y., W. Han, T. Shinoda, C. Wang, R.-C. Lien, J. N. Moum, and J.-W. Wang, 2013: Effects of the diurnal cycle in solar radiation on the tropical indian ocean

mixed layer variability during wintertime madden-julian oscillations. *Journal of Geophysical Research: Oceans*, **118 (10)**, 4945–4964.

Masson, S., P. Terray, G. Madec, J.-J. Luo, T. Yamagata, and K. Takahashi, 2012: Impact of intra-daily sst variability on enso characteristics in a coupled model. *Climate dynamics*, **39 (3-4)**, 681–707.

Meehl, G., R. Lukas, G. Kiladis, K. Weickmann, A. Matthews, and M. Wheeler, 2001: A conceptual framework for time and space scale interactions in the climate system. *Climate Dynamics*, **17 (10)**, 753–775.

Misra, V., L. Marx, M. Brunke, and X. Zeng, 2008: The equatorial pacific cold tongue bias in a coupled climate model. *Journal of Climate*, **21 (22)**, 5852–5869.

Nordeng, T. E., 1994: *Extended versions of the convective parametrization scheme at ECMWF and their impact on the mean and transient activity of the model in the tropics*. European Centre for Medium-Range Weather Forecasts.

Oberhuber, J. M., 1993: Simulation of the atlantic circulation with a coupled sea ice-mixed layer-isopycnal general circulation model. part i: Model description. *Journal of Physical Oceanography*, **23 (5)**, 808–829.

Pacanowski, R., 1987: Effect of equatorial currents on surface stress. *Journal of physical oceanography*, **17 (6)**, 833–838.

Palmer, T. N., 2001: A nonlinear dynamical perspective on model error: A proposal for non-local stochastic-dynamic parametrization in weather and climate prediction models. *Quarterly Journal of the Royal Meteorological Society*, **127 (572)**, 279–304.

Rädel, G., T. Mauritsen, B. Stevens, D. Dommenget, D. Matei, K. Bellomo, and A. Clement, 2016: Amplification of el nino by cloud longwave coupling to atmospheric circulation. *Nature Geoscience*.

Rayner, N., D. E. Parker, E. Horton, C. Folland, L. Alexander, D. Rowell, E. Kent, and A. Kaplan, 2003: Global analyses of sea surface temperature, sea ice, and night marine air temperature since the late nineteenth century. *Journal of Geophysical Research: Atmospheres*, **108 (D14)**.

Seo, H., A. C. Subramanian, A. J. Miller, and N. R. Cavanaugh, 2014: Coupled impacts of the diurnal cycle of sea surface temperature on the madden–julian oscillation. *Journal of Climate*, **27 (22)**, 8422–8443.

Steele, M., R. Morley, and W. Ermold, 2001: Phc: A global ocean hydrography with a high-quality arctic ocean. *Journal of Climate*, **14 (9)**, 2079–2087.

Stevens, B., et al., 2013: Atmospheric component of the mpi-m earth system model: Echam6. *Journal of Advances in Modeling Earth Systems*, **5 (2)**, 146–172.

Tang, Y. and W. W. Hsieh, 2003: Nonlinear modes of decadal and interannual variability of the subsurface thermal structure in the pacific ocean. *Journal of Geophysical Research: Oceans (1978–2012)*, **108 (C3)**.

Terray, P., K. Kamala, S. Masson, G. Madec, A. Sahai, J.-J. Luo, and T. Yamagata, 2012: The role of the intra-daily sst variability in the indian monsoon variability and monsoon-enso–iod relationships in a global coupled model. *Climate dynamics*, **39 (3-4)**, 729–754.

Thushara, V. and P. Vinayachandran, 2014: Impact of diurnal forcing on intraseasonal sea surface temperature oscillations in the bay of bengal. *Journal of Geophysical Research: Oceans*, **119 (12)**, 8221–8241.

Tiedtke, M., 1989: A comprehensive mass flux scheme for cumulus parameterization in large-scale models. *Monthly Weather Review*, **117 (8)**, 1779–1800.

Timmermann, A., F.-F. Jin, and J. Abshagen, 2003: A nonlinear theory for el niño bursting. *Journal of the atmospheric sciences*, **60 (1)**, 152–165.

Tziperman, E., 1986: On the role of interior mixing and air-sea fluxes in determining the stratification and circulation of the oceans. *Journal of Physical Oceanography*, **16 (4)**, 680–693.

Valcke, S., A. Caubel, D. Declat, and L. Terray, 2003: OASIS ocean atmosphere sea ice soil user's guide. Tech. rep., Cent. Eur. Formation Avancee Calcul Sci., 85 pp., Toulouse, France.

Vialard, J., C. Menkes, J.-P. Boulanger, P. Delecluse, E. Guilyardi, M. J. McPhaden, and G. Madec, 2001: A model study of oceanic mechanisms affecting equatorial pacific sea surface temperature during the 1997-98 el niño. *Journal of Physical Oceanography*, **31 (7)**, 1649–1675.

Walin, G., 1982: On the relation between sea-surface heat flow and thermal circulation in the ocean. *Tellus*, **34 (2)**, 187–195.

Watanabe, M., M. Chikira, Y. Imada, and M. Kimoto, 2011: Convective control of enso simulated in miroc. *Journal of Climate*, **24 (2)**, 543–562.

Weller, R. A., S. Majumder, and A. Tandon, 2014: Diurnal restratification events in the southeast pacific trade wind regime. *Journal of Physical Oceanography*, **44 (9)**, 2569–2587.

Williams, P. D., 2012: Climatic impacts of stochastic fluctuations in air–sea fluxes. *Geophysical Research Letters*, **39 (10)**.

Wittenberg, A. T., A. Rosati, N.-C. Lau, and J. J. Ploshay, 2006: Gfdl's cm2 global coupled climate models. part iii: Tropical pacific climate and enso. *Journal of Climate*, **19 (5)**, 698–722.

Wu, G., Y. Guan, Y. Liu, J. Yan, and J. Mao, 2012: Air–sea interaction and formation of the asian summer monsoon onset vortex over the bay of bengal. *Climate dynamics*, **38 (1-2)**, 261–279.

Yang, Y., T. Li, K. Li, and W. Yu, 2015: What controls seasonal variations of the diurnal cycle of sea surface temperature in the eastern tropical indian ocean?*. *Journal of Climate*, **28 (21)**, 8466–8485.

Yu, J.-Y. and W. T. Liu, 2003: A linear relationship between enso intensity and tropical instability wave activity in the eastern pacific ocean. *Geophysical research letters*, **30 (14)**.

Zhang, T. and D.-Z. Sun, 2014: Enso asymmetry in cmip5 models. *Journal of Climate*, **27 (11)**, 4070–4093.

Zhang, T., D.-Z. Sun, R. Neale, and P. J. Rasch, 2009: An evaluation of enso asymmetry in the community climate system models: A view from the subsurface. *Journal of Climate*, **22 (22)**, 5933–5961.

Acknowledgements

Foremost, my sincere gratitude goes to my advisor Prof. Jin-Song von Storch for her continuous support during my PhD study. I can not express enough thanks for her passion, patience and wise in almost weekly discussions, which have substantially helped me in the research and writing on this thesis. Much appreciation goes to my co-advisor Dr. Eileen Hertwig, who is always willing to discuss whenever I knock on her door and gives me plenty of help on English writing and time management. I am deeply indebted to Prof. Jochem Marotzke for chairing my panel and offering thoughtful and encouraging guidance during my panel meetings. I am very grateful to Prof. Martin Claussen for being the reviewer and chair of my PhD committee.

I am grateful to Dr. Stephan Bakan for carefully reading the manuscript of chapter 3 during the internal review process and for lots of helpful comments. I would like to thank Dr. Chao Li, Dr. Hongmei Li and Dr. Jian Su for many good ideas coming up in the talks. And thanks to Dr. Dian Putrasahan for many helpful discussions and suggestions, especially in using MPI-ESM. I would like to thank Irina Fast and Dr. Helmuth Haak for their supports and interests in my work.

I would like to thank IMPRS-ESM and the ocean group at MPI-M. It has been my great pleasure to meet so many brilliant students and colleagues. Especially, we spend lots of happy time together during the retreat of IMPRS-ESM. Special thanks to Dr. Antje Weitz, Cornelia Kampmann and Wiebke Böhm for their organisational and mental support.

Thanks to Christina Rieckers, for her excellent help when I for the first time came to Hamburg. Thanks to Mrs. Elke Klose for sharing with me her beautiful apartment and comfortable time, encouraging me to write, and staying with me in prayer. My grateful thanks goes to my friends, Zhuhua, Xueyuan, Feifei, Ruidan, Xin, Guokun for all the fun we had here in Hamburg and making me feel home in Hamburg.

Last but not the least, I would also like to thank my parents for giving me

freedom in pursuing my PhD abroad. I also would like to thank my husband Suguang for cooking me a big breakfast every morning to keep me full of energy the whole day and encouraging me early to bed, early to rise during the past few years.

Eidesstattliche Erklärung

Hiermit erkläre ich an Eides statt, dass ich die vorliegende Dissertationsschrift selbst verfasst und keine anderen als die angegebenen Quellen und Hilfsmittel benutzt habe.
I hereby declare, on oath, that I have written the present dissertation by myself and have not used other than the acknowledged resources and aids.

Hamburg, 25 April 2016
Fangxing Tian

Hinweis / Reference

Die gesamten Veröffentlichungen in der Publikationsreihe des MPI-M
„Berichte zur Erdsystemforschung / Reports on Earth System Science“,
ISSN 1614-1199

sind über die Internetseiten des Max-Planck-Instituts für Meteorologie erhältlich:
http://www.mpimet.mpg.de/wissenschaft/publikationen.html

All the publications in the series of the MPI -M
„Berichte zur Erdsystemforschung / Reports on Earth System Science“,
ISSN 1614-1199

are available on the website of the Max Planck Institute for Meteorology:
http://www.mpimet.mpg.de/wissenschaft/publikationen.html